Attosecond spectroscopy for the investigation of ultrafast dynamics in atomic, molecular and solid-state physics

Rocío Borrego Varillas[1], **Matteo Lucchini**[1,2] **& Mauro Nisoli**[1,2]

[1]Institute for Photonics and Nanotechnologies (IFN) – Consiglio Nazionale delle Ricerche (CNR), Piazza Leonardo da Vinci 32, 20133 Milano, Italy

[2]Department of Physics, Politecnico di Milano, Piazza Leonardo da Vinci 32, 20133 Milano, Italy

E-mail: mauro.nisoli@polimi.it

Abstract. Since the first demonstration of the generation of attosecond pulses (1 as $= 10^{-18}$ s) in the extreme-ultraviolet (XUV) spectral region, several measurement techniques have been introduced, at the beginning for the temporal characterization of the pulses, and immediately after for the investigation of electronic and nuclear ultrafast dynamics in atoms, molecules and solids with unprecedented temporal resolution. The attosecond spectroscopic tools established in the last two decades, together with the development of sophisticated theoretical methods for the interpretation of the experimental outcomes, allowed to unravel and investigate physical processes never observed before, such as the delay in photoemission from atoms and solids, the motion of electrons in molecules after prompt ionization which precede any notable nuclear motion, the temporal evolution of the tunneling process in dielectrics, and many others. This review focused on applications of attosecond techniques to the investigation of ultrafast processes in atoms, molecules and solids. Thanks to the introduction and ongoing developments of new spectroscopic techniques, the attosecond science is rapidly moving towards the investigation, understanding and control of coupled electron-nuclear dynamics in increasingly complex systems, with ever more accurate and complete investigation techniques. Here we will review the most common techniques presenting the latest results in atoms, molecules and solids.

1. Introduction

The discovery of high-order harmonic generation (HHG) in gases, a highly nonlinear process in which XUV radiation is emitted during the interaction of an intense laser pulse with a gaseous medium, set the basis for the generation of attosecond pulses [1–4]. In 2001, the first observation of a train of pulses with a temporal duration of 250 as was reported [5]. In the same year Hentschel and co-workers isolated for the first time a single attosecond pulse with a duration of 650 as from the train [6]. These achievements marked the birth of a new branch of ultrafast science, able to resolve the electron motion on its natural time scale: attosecond science [7–12]. Its advent has paved the

way for the direct observation and control of electron motion in molecules opening up the possibility for the ultimate real-time control of chemical reactions, one of the central problems in modern chemistry [11]. Recent important advances in the application of attosecond techniques to solid samples promise to shed light onto fundamental solid-state dynamical phenomena and light-carrier manipulation, allowing us, for example, to explore the ultimate speed limits of electronics [13]. We mention that ultrashort XUV pulses have been generated in the last two decades by using different nonlinear media, such as solids [14, 15] and plasma induced by ultrashort laser pulses on solid surfaces [16–18] and by using X-ray free-electron lasers (FELs) [19]: these techniques will not be discussed in this work.

In brief, to generate high-order harmonics in gas, ultrashort laser pulses [20, 21], with duration ranging from a few femtoseconds to a few tens of femtoseconds, are focused onto the gas medium (typically, a noble gas) at intensities in the range between 10^{12} to $10^{15}\,\mathrm{W/cm^2}$ [8, 9, 18, 22]. At such intensities, the Coulomb potential experienced by the outer shell electrons of the gas is strongly deformed and a potential barrier is generated, through which the outer-shell electrons can tunnel. Tunnel ionization is most probable in short temporal windows around each crest of the driving electric field. After tunnel ionization, the electron moves in the electric field of the excitation pulse (named driving pulse, hereafter) thus acquiring a high kinetic energy. In the case of linearly polarized driving pulses, the electron may return to the parent ion, with a quite small probability, and radiatively recombine. In this process, the kinetic energy of the recolliding electron is released in the form of a very short light burst [23–27]. The maximum kinetic energy of the recolliding electrons is proportional to the product of peak intensity, I_0, of the driving pulses and of the square of their central wavelength, λ_0, $\mathcal{E}_{k,max} \propto I_0\lambda_0^2$. Therefore, the spectrum of the emitted radiation may extends up to the soft-x-ray energy region. Indeed, the maximum photon energy is given by the so-called *cutoff law*: $\hbar\omega_{max} = I_p + 3.17U_p$, where I_p is the ionization potential of the gas used for HHG and $U_p \propto I_0\lambda_0^2$ is the ponderomotive energy (i.e., the average kinetic energy of an electron in an oscillating electric field). Since this processes is periodically repeated every half optical cycle of the driving laser field (typically, $\sim 1\,\mathrm{fs}$), a train of attosecond pulses is generated. In a different configuration, a two-colour driving field (fundamental plus second harmonic) is employed. In this case, due to symmetry breaking of the driving field, a train of attosecond pulses separated by a complete optical cycle of the fundamental radiation is generated.

For a number of important applications, single attosecond pulses, instead of trains of attosecond pulses, are required. For this reason, from the very beginning of the attosecond technology, several techniques have been developed to confine the harmonic generation process to a single event, thus leading to the production of isolated attosecond pulses [10, 28, 29]. All these experimental techniques can be understood in terms of *gating* of the harmonic radiation or of the harmonic generation process. The most used experimental approaches are based on spectral selection of the cutoff harmonics (i.e., the high-energy portion of the harmonic spectrum) or on temporal gating techniques.

A particular temporal gating technique is based on the use of driving pulses with a modulated polarization state, such that only during a short temporal window close to the peak of the pulse, the polarization is close to linear: harmonic generation is therefore confined within this portion of the driving field [30–33]. Typical energies of isolated attosecond pulses are from tens of picojoules up to the microjoule level (see an overview of gas-phase isolated attosecond light pulses in [10, 34]). In order to induce nonlinear processes, intensities above 10^{11} W/cm^2 are required, currently generated in the 15-35 eV photon energy range in the form of trains and isolated attosecond pulses with duration < 700 as [35, 36]. Since the XUV photon flux scales with $\lambda^{-5.5}$ [37], while the maximum photon energy scales with λ^2, the generation of high-intensity attosecond pulses with hundreds of eV photon energy is particularly challenging. A record value of 10^9 photons/s in 1% bandwidth in a x-ray supercontinuum in the water window spectral region (284-543 eV) was reported by using high-energy mid-infrared driving laser source, focused in waveguides filled by high-pressure helium gas [38, 39]. Free electron lasers (FELs) offer the possibility to significantly increase the attosecond pulse energy at high photon energy, up to the keV region, as recently demonstrated by Duris *et al.* [19], with the generation of isolated attosecond pulses with tens of microjoules of pulse energy in the soft-x-ray range (> 280 eV), thus reaching intensities sufficient for attosecond-pump/attosecond-probe experiments. The median pulse energy was 10 μJ at 905 eV and 25 μJ at 570 eV. In this work, we will only review advances in attosecond science based on the use of table-top technology.

A variety of experimental techniques have been introduced for the characterization and application of attosecond pulses [22, 40, 41]. The typical experimental approach is based on the use of attosecond pulses, in the form of trains of pulses or of isolated pulses, in combination with few-femtosecond infrared (IR) pulses, with or without controlled electric field (i.e., with or without stable carrier-envelope phase, CEP). This is due to the low photon flux of typical attosecond beamlines, which has limited, until recently, the development of experimental setups for attosecond-pump/attosecond-probe measurements. The high photon energy of attosecond pulses leads, in general, to the ionization of the sample, with the subsequent release of one (or more) photoelectron. The sample is thus left in a nonstationary state, which will evolve in time. By using a second delayed pulse, one can detect the photo-induced dynamics and obtain time-resolved spectroscopic information of the system upon measuring the evolution of the spectrum of the photoelectrons as a function of the pump-probe delay. This was the first experimental approach introduced in attosecond science, at the beginning for the temporal characterization of the pulses and immediately after for their application to the measurement of the characteristic time constants of the relaxation dynamics of core-excited krypton atoms [42]. More recently, attosecond photoelectron spectroscopy has been employed to study the ultrafast dynamics in the process of photo-ionization [43], with particular attention to photoemission from solid targets [44–50], or the ultrafast electron dynamics in dielectric nanoparticles, thus offering real-time access to electron scattering in dielectrics [51]. Besides electrons, the production yield of ionic fragments

generated by attosecond excitation can be measured as a function of pump-probe delay. This experimental approach has been used to investigate the light-induced electron tunneling in atoms [52], the electron localization process in diatomic molecules after excitation [53] or the charge migration process in amino acids [54, 55], to cite just a few examples.

In the last decade an all-optical spectroscopic technique, largely used in the femtosecond domain, has been implemented in the attosecond domain. The spectrum of the attosecond pulses transmitted or reflected by the sample is measured as a function of the delay between the attosecond pulse and, in general, a few-femtosecond pump pulse. Since its first implementation in the attosecond domain in 2010, with the investigation of ultrafast electron dynamics in krypton [56] and argon [57], attosecond transient absorption spectroscopy (ATAS) has established as a very powerful tool for the investigation of sub-femtosecond electron dynamics in atomic, molecular and solid state physics. More recently attosecond transient reflection spectroscopy (ATRS) has been employed for the investigation of ultrafast carrier dynamics in solids, which cannot be manufactured in thin membranes [58].

A different class of all-optical experiments is high-order harmonic generation spectroscopy. In this case, information about the electron and coupled electron-nuclear dynamics in molecules and solids is encoded in the harmonic spectrum generated in the sample by the driving pulse. This is related to the fact that the high-harmonic spectrum contains information on both the ionization and the recollision processes of the electronic wavepacket generated by tunnel ionization, which recombine with the parent ion. The evolution of the ionized system between electron ionization and recollision can be probed by the acquisition of a single high-harmonic spectrum, since it contains a broad range of energies corresponding to different time intervals spent by the electron in the continuum after tunnel ionization. This spectroscopic technique combines sub-angstrom spatial resolution, related to the de Broglie wavelength of the recolliding electron, with attosecond temporal resolution, thus offering the possibility to resolve the evolution of electronic wavefunctions. During the past two decades, high-order harmonic spectroscopy has been successfully applied to resolve fundamental strong-field phenomena such as field-induced tunneling in atoms, ultrafast nuclear dynamics, charge migration in molecules and field-induced currents in solids. This spectroscopic technique will not be discussed in this Review (for review of this topic, see for example [59–61]).

The objective of this work is to review some of the most widely used attosecond spectroscopic techniques, developed since the beginning of the attosecond era, for the investigation of electron and coupled nuclear dynamics. In particular, attosecond electron/ion pump-probe spectroscopy in atoms, molecules, nanoparticles and solids is the subject of Section 2 of this Review. Attosecond transient absorption spectroscopy in atomic, molecular and solid state physics and attosecond transient reflection spectroscopy in solids are discussed in Section 3. In the last section of the review, the current status of attochemistry is summarized and an outlook of future investigations in this field is given.

2. Attosecond electron/ion pump-probe spectroscopy

One of the most extended spectroscopic schemes in attosecond science is time-resolved photo-electron(ion) spectroscopy. These technique involves a first pulse (pump), which drives the system out of equilibrium, and a second pulse (probe), which follows the dynamics initiated by the pump. Typically attosecond spectroscopy experiments use an XUV attosecond pulse in combination with an intense few-cycle IR field; due to the high energy of the XUV photons, an inner valence or core photoelectron is emitted from the sample, which is used to extract the photo-induced dynamics.

There exists a large variety of techniques to obtain spectroscopic information from the electrons and ions released upon the XUV induced photoionization. One of the most widespread methods is the use of time of flight (TOF) spectrometers, which measure the time required by a charged particle to fly along a drift tube, allowing to obtain the kinetic energy distribution of the photoelectrons (electron TOF spectrometer [62]) or the mass-charge ratio of the photoions (ion mass TOF spectrometer [63]). TOF spectrometers are composed by a stack of plates (which accelerate the particles), a flying tube and a detector (typically a microchannel plate - MCP -coupled to a scintillator and a photomultiplier tube). An improvement in the collection efficiency can be achieved with magnetic bottle spectrometers [64], which effectively collects the electrons emitted in different directions. by means of electron trajectory parallelization mechanism induced by a strong inhomogeneous magnetic field.

In spite of their versatility, TOF and magnetic bottle spectrometers have some limitations in terms of angular resolution and ion-electron coincidence measurements. To this end, velocity map imaging (VMI) spectrometers and reaction microscopes (REMI) have been developed. VMI spectrometers allow for measuring angular-resolved kinetic energy distributions [65] by generating a static field with two electrodes (repeller and extractor) and projecting the charged particles onto a position sensitive detector, e.g a MCP multiplier and a phosphor screen. A fast charge-coupled device (CCD) camera is then used to record images of the phosphors. The time required to reach the detector and the final impingement position provide and indirect measurement of the three spatial components of the particle initial velocity, which can be retrieved by means of an inverse-Abel transform [66].

Kinematically complete experiments call for the simultaneous detection of multiple ions and electrons. This is possible thanks to REMI [67], which measures the 3D momentum distribution of all charged fragments generated from the target. Reaction microscopes have emerged from the cold-target recoil ion momentum spectroscopy (COLTRIMS) technique combined with electron imaging [68]. Such spectrometer requires a well-collimated beam of cold molecules or atoms, which is ionized by the laser beam. The produced ions and electrons are then extracted by applying a weak electrostatic field and a set of electrodes designed to accelerate ions and electrons in opposites sides of the spectrometer. In order to achieve a better spatial confinement of electrons, two (or sometimes three) large Helmholtz coils are used to create a

homogeneous magnetic field approximately parallel to the electric field.

2.1. Attosecond photoelectron/ion spectroscopy experimental techniques

Let us know review how the information about the ultrafast temporal evolution of the system can be extracted by employing these methods in combination with time-resolved spectroscopy schemes. There are three main attosecond investigation schemes, which employ photo-electrons/ions as an observable:

2.1.1. RABBITT (Reconstruction of Attosecond Beating By Interference of Two-photon Transitions) This technique is based on the measurement of the spectra of the photoelectrons emitted by a sample excited by train of attosecond pulses in the presence of an IR field as a function of the delay between the IR and XUV pulses [5, 69]. The principle of the RABBITT technique is presented in Fig. 1. A train of attosecond XUV pulses, which corresponds in the spectral domain to a comb of odd-order harmonics, ionizes the sample. In the absence of an IR field, the photoelectron spectra consist of a series of peaks, spaced by $2\hbar\omega_{IR}$ (with ω_{IR} the central frequency of the IR pulse), corresponding to the direct ionization by single-photon absorption of XUV harmonics. When the XUV pulses overlap spatially and temporally with a relatively weak IR field (peak intensity around $10^{11}\,\mathrm{W/cm^2}$), an IR photon can be either emitted or absorbed giving rise to additional peaks (sidebands) in the photoelectron spectra located at $\pm\hbar\omega$ with respect to the main peaks. Due to the interference between two indistinguishable quantum paths (one comprising the absorption of an XUV and IR photon, the other the absorption of the next harmonic and the emission of an IR photon) the amplitude of the sideband is periodically modulated with twice the periodicity of the IR field. In the framework of the second-order perturbation theory for the light–matter interaction, under the rotating-wave approximation, considering only the processes where the XUV fields are absorbed first, and assuming monochromatic fields, the signal of the $q-th$ sideband can be written as [70]:

$$S_q(\tau) = |A_{em}|^2 + |A_{abs}|^2 + 2\,|A_{em}|\,|A_{abs}|\cos(2\omega_{IR}\tau - \Delta\phi_q - \Delta\phi_{atom}) \qquad (1)$$

where τ is the time delay between the XUV and IR pulses, $\Delta\phi_q$ is the phase difference between two consecutive harmonics ($q-1$ and $q+1$) and $\Delta\phi_{atom}$ is the intrinsic phase difference of the target matrix elements corresponding to a photoionization from two consecutive harmonics. A_{abs} (A_{em}) denotes the photoemission probability for a two-color mechanism, which involves the absorption of an harmonic $q-1$ ($q+1$) and the absorption (emission) of an additional fundamental photon.

From Eq. (1) it is clear that the sideband oscillates at twice the frequency of the IR field. RABBITT has been first applied for XUV pulse temporal characterization [5, 71] and later to the measurement of photoemission time delays [43, 72]. In the first case, a known target is used, such that the atomic phase, $\Delta\phi_{atom}$, can be precisely calculated, rendering the phase difference between consecutive harmonics, $\Delta\phi_q$, directly

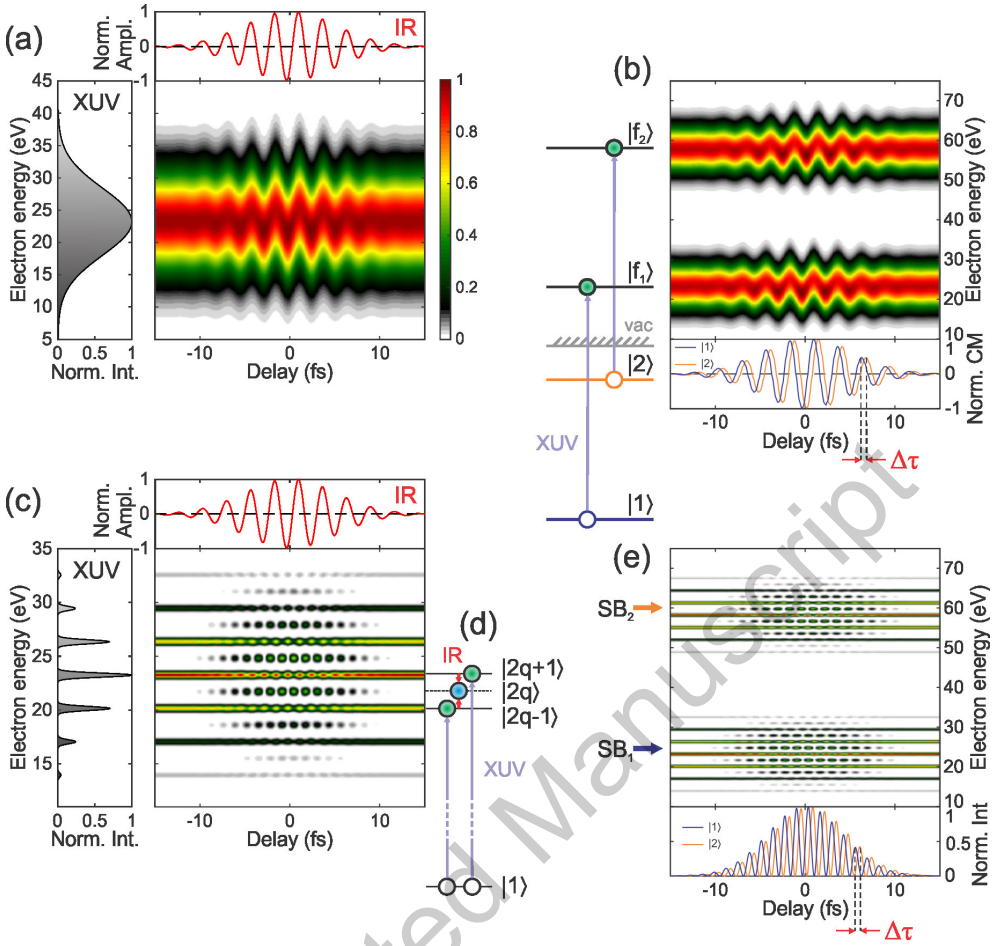

Figure 1. Principles of streaking and RABBITT techniques. (a) Streaking trace obtained from ionization of a single initial state. (b) Double streaking trace resulting from the ionization of two initial states (depicted in the excitation scheme on the left side). The two panels in (a) show the XUV spectrum (left) and the vector potential of the IR femtosecond pulse (top). The lower panel in (b) shows the center of mass (CM) extracted from the two streaking traces. The delay $\Delta\tau$ between the two oscillatory curves corresponds to an actual relative delay in the photoemission process between states $|1\rangle$ and $|2\rangle$. (c), (e) Analogous situation for the case of RABBITT. The XUV spectrum in the left panel of (c) is characterized by discrete odd harmonic peaks. In (d) is sketched the principle of the RABBITT technique leading to the formation of oscillating sidebands (order $2q$, with q an integer) between two harmonic peaks $(2q \pm 1)$. The lower panel in (e) shows the integrated electron yield for two sidebands corresponding to the same order and marked by the respective arrows.

accessible. In the second case, $\Delta\phi_{atom}$ can be determined if the relative phase between consecutive harmonics, $\Delta\phi_q$, is known. It is possible to show that the atomic phase is directly linked to the time delay a particle experiences when it is scattered by a potential [73], $\tau_{atom} = d\phi_{atom}/d\omega$, hence, from a RABBITT measurement one can extract the photoemission time delay [74].

2.1.2. Attosecond streaking As in the case of RABBITT, attosecond streaking is based on the measurement of the electrons photoionized by an XUV pulse in the presence of an IR field (streaking pulse) [75–77]. In contrast to RABBITT, it does not use a train of pulses, but a single attosecond pulse [78].

If the intensity of the IR pulse is weak enough to avoid the ionization of the medium, but sufficient to impart substantial momentum to the photoelectrons generated by the XUV (typically around $10^{12}\,\mathrm{W/cm^2}$), it will modulate the kinetic energy spectra of the photoelectrons as a function of the temporal delay. Under the assumption of a nearly constant dipole transition matrix element over the energy spectrum of the attosecond pulse, the electron wave packet can be considered as a replica of the XUV pulse. The streaking spectrogram measured upon scanning the time delay between the XUV and IR pulses is given by [79]

$$S(\mathbf{p},\tau) = \left| \int_{-\infty}^{+\infty} e^{i\phi(t)} \mathbf{d}_{\mathbf{p}+\mathbf{A(t)}} \cdot \mathbf{E}_{\mathbf{XUV}}(t-\tau) e^{i(p^2/2+I_p)t} dt \right|^2 \tag{2}$$

where $\mathbf{A}(t)$ is the vector potential of the streaking field, $\mathbf{v}$ is the final velocity of the electron, $\mathbf{p}$ is the final electron momentum in the continuum, $\mathbf{d}$ is the dipole matrix element, I_p is the ionization potential of the medium, $\mathbf{E}_{\mathbf{XUV}}$ is the XUV field and $\phi(t)$ is the quantum phase acquired by the electron due to its interaction with the laser field:

$$\phi(t) = -\int_{t}^{+\infty} [\mathbf{p}\cdot\mathbf{A}(t') + \frac{\mathbf{A}^2(t')}{2}] dt' \tag{3}$$

The spectrogram defined by Eq. (2) can be interpreted in the framework of the FROG (frequency resolved optical gating) technique [80], widely used in the field of femtosecond pule characterization. In this approach the two dimensional spectrogram (FROG trace) is given by the internal product of a temporal gate applied to a test pulse:

$$S(\omega,\tau) = \left| \int_{-\infty}^{+\infty} G(t) E(t-\tau) e^{i\omega t} dt \right|^2 \tag{4}$$

where $G(t)$ is the temporal gate, $E(t-\tau)$ is the electric field of the test pulse and ω the radiant frequency.

The extension of the FROG technique to the attosecond domain has been termed FROG-CRAB (FROG for complete reconstruction of attosecond bursts) and it was first proposed by Mairesse and Quéré [81]. Information about the spectral phase from the streaking trace can be retrieved by an iterative inversion algorithm, such as the principal component generalized projections algorithm (PCGPA) [82], the least squares GPA (LSGPA) [83], the extended ptychographic iterative engine (ePIE) algorithm [84] or more sophisticated algorithms [85, 86].

2.1.3. Attosecond time-resolved photoion spectroscopy RABBITT and streaking are both based on the measurement of the kinetic energy of the photoelectrons as a function of time. An alternative way to extract the information on the dynamics is to measure

the temporal evolution of the ion yields (or their velocity spectra) as a function of the pump-probe delay.

The high photon energy of the XUV pulses leads inevitably to the ionization of valence (and in some cases inner shell) orbitals, resulting in a wide range of fragment ions. Depending on the mechanism triggered by the XUV excitation, a time-delayed NIR field can, for example, redistribute the charge within the ion[53] or lead to a second photo-ionization which is more prone to occur depending on the location of the hole at that particular time delay [54]. In these two examples, the fingerprint in the observable is imprinted as an asymmetry in the angular distribution of the ejected fragment or as temporal oscillations in the ion yield. It is important to remark here that the interpretation of such experiments is not straightforward and requires the support of state-of-the-art numerical simulations.

2.2. Time-resolved photoelectron(ion) spectroscopy on atoms

The advent of attosecond pulses paved the way to resolve the electron motion on its natural time scale and to address fundamental questions in Physics such as: What are the characteristic time constants of the relaxation dynamics of core-excited atoms? [42] Is it possible to track in real time the subfemtosecond motion of valence electrons? [56] Is it possible to tell when a photoelectron has been freed from an atom? [87, 88] Can the creation of a photoelectron wavepacket be tracked and can this information be used to characterize atomic resonances? [89–92] How do electrons behave in presence of a strong electromagnetic field? [52, 93, 94].

The applications of attosecond methods to atomic spectroscopy has been extensively assessed in previous reviews [8, 9, 74, 95–98]. We will limit our discussion here to two seminal examples of attosecond photoelectron spectroscopy in atoms and a brief review of the works published in the last few years. A scheme of the basic processes that can occur in atoms after photoexcitation with an XUV pulse is shown in Fig. 2.

One of the first time-resolved experiments consisted on the measurement of the lifetime of M-shell vacancies of krypton (Kr) by means of attosecond photoelectron streaking [42]. Excitation of a core shell electron is followed by an ultrafast electronic rearrangement to fill the inner-shell vacancy. As depicted in Fig. 2, the hole generated after photoexcitation with an XUV pulse can be occupied with an electron from an outer shell, releasing the excess binding energy either in the form of a photon or transferred via electrostatic forces to second electron (Auger decay), which is subsequently ejected. The lifetime of core holes can be estimated from the spectral width of the the emitted photons or Auger electrons, but these measurements cannot provide a detailed mapping of the multi-electron dynamics.

In 2002 Drescher *et al.* proposed the use of attosecond streaking to measure the lifetime of the $3d$ core hole in Kr. In their experiment they used a 97-eV, sub-femtosecond soft-x-ray pulse for excitation and sub-7-fs few-cycle IR pulse centred at 16 eV for probing electron emission. The two pulses were then collinearly focused into

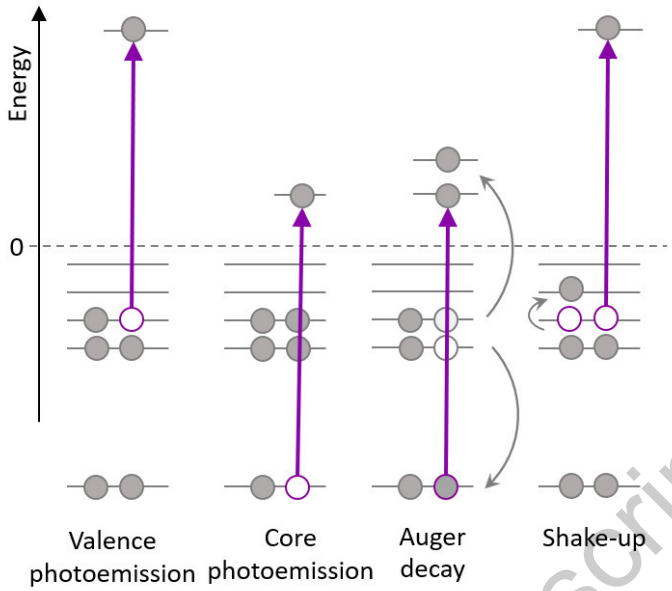

Figure 2. An XUV photon (purple arrow) interacts with an atom. A valence or core electron can be removed in a photoionization process. After excitation of a core level, a valence electron can occupy a core level with subsequent emission of another valence electron (Auger decay). Upon photoemission of a valence (or core) electron a second electron can be excited by electron correlation (shake up). Gray arrows represent internal processes, empty balls vacancies and circles with purple contour holes generated by the XUV excitation filled with another electron.

a Kr gas target and the kinetic energy distribution of the emitted photo and Auger electrons was measured with a TOF spectrometer. Excitation by the XUV pulse results on the creation of a $3d$ hole, which is accompanied by the emission of an electron from the $4p$ shell by Auger recombination. In the presence of a strong IR field the emitted electron changes its final momentum (reached after the light pulse left the interaction volume) by $\Delta p(t_r) = [eE_a(t_r)/\omega_L \sin(\omega_L t_r + \phi)]$ where t_r is the time at which the electron was ejected, E_a is the amplitude envelope, and ω_L and ϕ are the carrier frequency and carrier-envelope phase of the IR pulse. The final energy is thus given by:

$$E_f(t_r) = E_i + 2U_p(t_r)\sin^2(\omega_L t_r + \phi)\cos 2\theta + [8E_i U_p(t_r)]^{1/2}\sin(\omega_L t_r + \phi)\cos\theta \qquad (5)$$

where e, m_e and E_i stand for the electron charge, mass and initial energy, $U_p(t) = e^2E_a^2(t)/4m_e\omega_L^2$ is the electron cycle-averaged quiver energy in the probe light field and θ is the angle between the IR field vector and the final momentum of the electron. This time-to-energy mapping allows to sample the electron emission with attosecond temporal resolution. A lifetime of 7.9 fs of M-shell vacancies was measured in this way.

Attosecond streaking has also been used to investigate the delay of the photoemission of a $2s$ electron relative to a $2p$ electron in neon [87], the impact of electronic correlations on electron dynamics in helium [99] and to measure photoemission time delays between valence electrons of two different atomic species (argon and neon)

[100].

Photoelectron interferometric pump-probe schemes have been also developed for attosecond electron spectroscopy measurements [101]. In this technique an attosecond XUV pulse creates a wave packet by excitation of a coherent superposition of bound and continuum states in helium, while the subsequent IR pulse ionizes the bound states. The interference of the wave packet generated in the continuum by the XUV pulse (reference) and the one created from XUV and IR excitation results on an delay-dependent photoelectron spectrum (interferogram) that encodes information on the quantum beats [102] and multipath interference , allowing thus to characterize the bound electron wave packet.

A complementary approach to photoelectron spectroscopy with isolated attosecond pulses is to monitor the temporal evolution of the ions. In this scheme, the attosecond XUV pulse initiates an ionization process and the delayed few-cycle IR pulse subsequently produced a doubly ionization of the sample. The dynamics of the ion yield as a function of time can thus be linked to the electron dynamics of the system. This technique has been used for probing real time electron tunnelling ionization in neon and xenon [52], concluding that in neon electrons escape from their atomic binding potential under the influence of a strong IR field in a time window of 380 as near each field maximum of the ionizing IR pulse.

Interferometric-based photoelectron spectroscopy techniques using trains of attosecond pulses have been widely used to investigate electron dynamics in atoms [88, 91, 103–107], since the combination of both high temporal and spectral resolution allows for a clearer interpretation of the data. Pioneering work by L'Huillier's group characterized the variations in the phase of a wave packet in helium by exploiting the interferences between continuum electron wave packets that are prepared by a sequence of attosecond pulses [103]. In analogy to traditional optical shear interferometry techniques used for wavefront retrieval, if two shifted replicas of an electron wave packet can be created, their interference can be used to retrieve information on the phase. The principle can be briefly explain as follows: the momentum distribution of an electron ionized by an attosecond pulse is shifted by $-eA(\tau)$ if an IR field with vector potential $A(t)$ is present at the time of ionization τ. If now the atom is ionized by a sequence of two attosecond pulses separated by half the oscillation period of the IR field, two electron wave packets are formed, which will interfere in the region where their momentum distributions overlap. Depending on the time of ionization with respect to the carrier of the IR field, the interference will depend on the difference in accumulated phase between the electron wave packets (if τ coincides with a zero of $A(t)$) or on the difference between the phases of the initial electron wave packet (if τ coincides with a maximum or minimum of $A(t)$). This experimental scheme was applied for the investigation of the single-photon ionization in helium [103], proving that it is possible to use attosecond pulses to modulate the probability of an ionization event [104].

RABBITT-based methods have been widely used for the investigation of photoemission time delays in atoms [74]. Recalling Eq. (1) if one can precisely measure

τ and $\Delta\phi_q$, the atomic phase due to the two-photon ionization process, $\Delta\phi_{atom}$, can be directly determined. However, these variables are difficult to obtain separately. This bottleneck can be overcome by simultaneously creating two independent wave packets from different shells: the measurement of the two electron wave packets cancels the term $\Delta\phi_q$ and allows for determining the phase delay difference $\Delta\phi_{atom,shell1} - \Delta\phi_{atom,shell2}$ at the same photon energy. This principle was exploited by Klünder *et al.* to study photoemission from the $3s^2$ and $3p^6$ shells in argon, at different excitation energies ranging from 32 to 42 eV [88] establishing a difference in delays between -40 as (for SB22) and -110 as (SB24). Importantly, they concluded that this phase delay can be decomposed in two contributions, $\Delta\phi = \Delta\phi_{CC} + \Delta\phi_W$: the phase accumulated by the photoelectron when escaping from the atom due tot the process of photoionization (also known as Wigner phase, $\Delta\phi_W$) and a phase inherent to the measurement process due to the laser-driven continuum-continuum transition ($\Delta\phi_{CC}$).

The RABBITT principle was also exploited by Isinger *et al.* to determine the photoemission time delay in neon [107]. Back in 2010 Schultze *et al.* measured a delay of 21 as in the photoemission of $2s$ electron relative to the $2p$ electron in neon by attosecond streaking [87]. Multiple theoretical efforts tried to understand the origin of this delay, underpredicting the observed delay by about a factor of two [108–110]. Isinger et. solved the puzzle by measuring the photoionization delays with RABBITT, which allowed them to combine high temporal (20 as) and spectral (200 meV) resolution over a broad energy range (65-100 eV). In the experiment a comb of harmonics is produced by HHG in neon (Fig. 3e), which was filtered with a combination of 200-nm-thick aluminum and zirconium foils (letting through three harmonics below 75 eV) and with two zirconium filters (75-105 eV). The attosecond pulse train is combined in a Mach-Zehnder-like interferometer with a weak IR pulse and both pulses are collinearly focused into a magnetic bottle electron spectrometer with spectral resolution better than 100 meV.

The first column in Fig. 3 shows the photoelectron spectra: for both the $2s$ and $2p$ sub-shells, ionization results in three peaks due to absorption of harmonics (H41, H43, and H45) and two sideband peaks (SB42 and SB44) reachable by two-color two-photon transitions. Thanks to the narrow bandwidth of the aluminium-zirconium filter set, the spectra generated from the $2p$ and the $2s$ sub-shells are well separated in energy (the difference in the ionization energies of both subshells is 26.8 eV, therefore larger than the energy bandwidth transmitted by the filter). This allows to obtain simultaneously two individual RABBITT traces containing information on the phase delay of the electrons ionized from $2s$ and $2p$. The experimental results for the difference between $2s$ and $2p$ time delays are displayed in Fig. 3d, which are in very good agreement with many-body perturbation theoretical calculations (black line). A Fourier analysis of the sidebands allowed them also to disentangle the contribution of a shake-up process on the $2s$ time delay measurement, which might be at the origin of the discrepancy between the results of [87] and theoretical calculations.

Spectrally resolved electron interferometry has also been applied to the study of

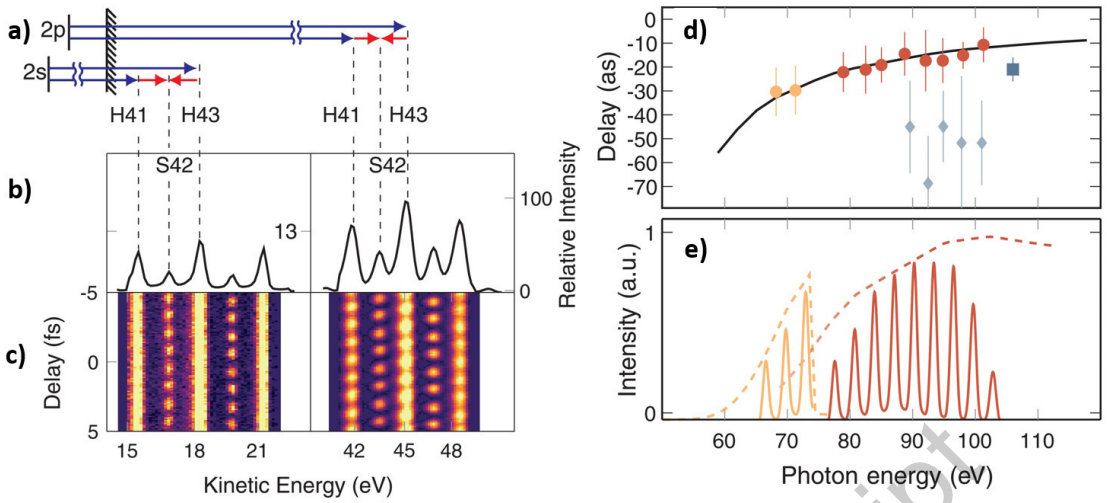

Figure 3. (a) Scheme of the RABBITT principle applied to the 2s and 2p shells in neon. Blue arrows represent the XUV pulse, whereas red stands for the IR photons. (b) Time-averaged photoelectron spectra. For both sub-shells, ionization results in three main bands corresponding to the absorption of photons of the 41st, 43rd and 45th harmonics and two side bands in between. (c) Photoelectron spectrum as a function of the XUV-IR time. (d) Difference in time delay $\tau_{atom}(2s) - \tau_{atom}(2p)$ in neon for different photon energies corresponding to the harmonics shown in panel (e). The square corresponds to delay measured in the experiment of Ref. [87] and the diamonds to the measured time delay differences between shake-up and $2p$ ionization. Black line represents the prediction by the numerical simulations. (e) High order harmonic spectra used in the experiment with a combination of aluminium and zirconium filters (yellow) and with two zirconium filters (red). From [107]. Reprinted with permission from AAAS.

ultrafast strongly correlated multielectron dynamics. Clear examples are the electron dynamics of autoionizing states [111], Cooper minima [112, 113] or shape resonances [91, 92, 114, 115]. In particular, the investigation of the wave packets created through Fano autoionizing resonances has attracted considerable attention in the last years [91, 92, 114–117].

Gruson *et al.* [91] were able to monitor the build up of a wave packet around a Fano resonance in helium, characterizing its amplitude and phase. In their experimental setup, a comb of harmonics derived from a mid-IR source photoionizes helium. The 63rd harmonic is driven into the $2s2p$ autoionizing resonance. Since the resonance width (37 meV) is much narrower than the harmonic width (400 meV), a broad resonant electron wave packet with complex spectral amplitude is generated. Simultaneously harmonics H61 and H65 create non resonant electron wave packets in the continuum, which serve as a reference to probe the resonant electron wave packet. A weak replica of the mid-IR is again used to induce the interference creating a RABBITT trace, which encodes information on the amplitude and phase of the resonant wave packet. In fact, the argument of the cosine in Eq. (1) reads in this case: $2\omega_{IR}\tau + \Delta\phi_q + \Delta\phi_{scat}$ where $\Delta\phi_{scat} = \Delta\phi_{scat,NR} - \Delta\phi_{scat,R}$ is the difference between the nonresonant and resonant

scattering phases of the two intermediate states. In the presence of a Fano resonance the terms $\Delta\phi_q$ and $\Delta\phi_{scat,NR}$ are negligible with respect to $\Delta\phi_{scat,R}$ and therefore a Fourier analysis of the fringes in the spectrogram allows for the phase retrieval of the resonant wave packet.

More recently Cirelli *et al.* investigated the photoemission time delays in argon in the vicinity of the $3s^{-1}np$ autoionizing resonances [92]. The experimental approach combined detection with a VMI and a reaction microscope, which enables the retrieval of the full 3D momentum vector in coincidence for electrons and ions. This provides additional information with respect to the previous examples, as it allows to explore the angular behaviour of resonant atomic time delays. The results obtained by Cirelli *et al.* showed that indeed the time delay measured in the vicinity of these resonances depends strongly on the electron ejection angle with respect to the ionizing field polarization.

2.3. TR-photoelectron(ion) spectroscopy on molecules

One of the most interesting applications of attosecond science has been the implementation of this technology to visualize and control the electron motion in molecules opening the possibility for the ultimate real-time control of chemical reactions, one of the central problems in modern chemistry. In this section we will review the progress on attosecond measurements in molecules, starting from diatomic molecules and evolving towards more complex targets. For a deeper insight, we refer the reader to the most recent reviews on the topic [11, 118].

2.3.1. Molecular Hydrogen The examples covered in this section are fundamental works in the field of attosecond science, as they represent the first extension of attosecond spectroscopy from atoms to molecular targets. The majority of these studies addressed the case of molecular hydrogen (H_2) and deuterium (D_2), for which reliable theoretical simulations were possible. The potential energy curves of the states involved in the dissociative ionization of H_2 are shown in Fig. 4.

One of the most remarkable achievements in time-resolved experiments was the demonstration and control of electron localization in H_2 and D_2. In a pioneering work Kling *et al.* [96], used two intense, few-cycle near-IR pulses to observe electron localization in the dissociative ionization of D_2 molecules by modifying the relative CEP of the IR pulses.

A few years later, in 2010, Sansone *et al.* achieved the control onto the localization of the electronic charge distribution by combining for the first time a few-cycle IR beam with an isolated attosecond pulse [53]. The 300-400 as pulse, covering a bandwidth extending from 20 to 40 eV, triggers ionization in H_2 or D_2 molecules, which results in the generation of H^+ or D^+ fragments. A delayed IR pulse redistributed the charge within the ion and the three-dimensional momentum distribution of the fragments is then mapped using a VMI spectrometer. In particular, they observed an asymmetry in the ion yield, interpreted as a clear indication of electron localization, which occurs by

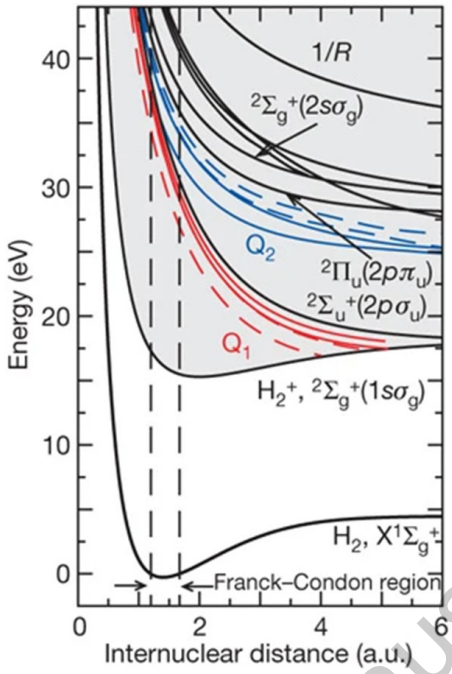

Figure 4. Potential energy surfaces of the states involved in the dissociative ionization of molecular hydrogen. Adapted figure with permission from [53], Copyright (2010) by the American Association for the Advancement of Science.

means of two mechanisms, as illustrated in Fig. 5.

Due to the broad bandwidth of attosecond pulses, several dissociative ionization channels can be accessed. In the absence of the IR, for photon energies between 25 and 36 eV, a parallel transition preferentially excites molecules aligned along the polarization axis to the doubly excited $Q_1^1\Sigma_u^+$ states; subsequent autoionization to the $^2\Sigma_g^+(1s\sigma_g)$ state produces ionic fragments with a kinetic energy primarily between 2 and 7 eV. At 30 eV it is possible to access the repulsive $^2\Sigma_u^+(2p\sigma_u)$ state. Above 31 eV, a perpendicular transition preferentially excites molecules aligned orthogonally to the laser polarization axis to the $Q_2^1\Pi_u$ doubly excited states; these states autoionize to the two lowest electronic states of the cation $^2\Sigma_u^+(2p\sigma_u)$ and $^2\Sigma_g^+(1s\sigma_g)$, resulting in ionic fragments with kinetic energies of 5-8 eV and 1-5 eV, respectively.

This kinetic distribution of the ion fragments changes in the presence of the intense IR pulse. Further information on the charge localization can be extracted by analyzing the angular momentum distribution of the ejected fragments, and more in particular the laboratory-frame asymmetry parameter:

$$A(E_k,\tau) = \frac{N_R(E_k,\tau) - N_L(E_k,\tau)}{N_R(E_k,\tau) + N_L(E_k,\tau)}$$

where E_k denotes the kinetic energy, τ the time delay and N_R and N_L are the number of fragments emitted at 45° of the polarization axis on the right and left-hand sides of the detector. As shown in Fig. 5b the asymmetry parameter displays distinct oscillations

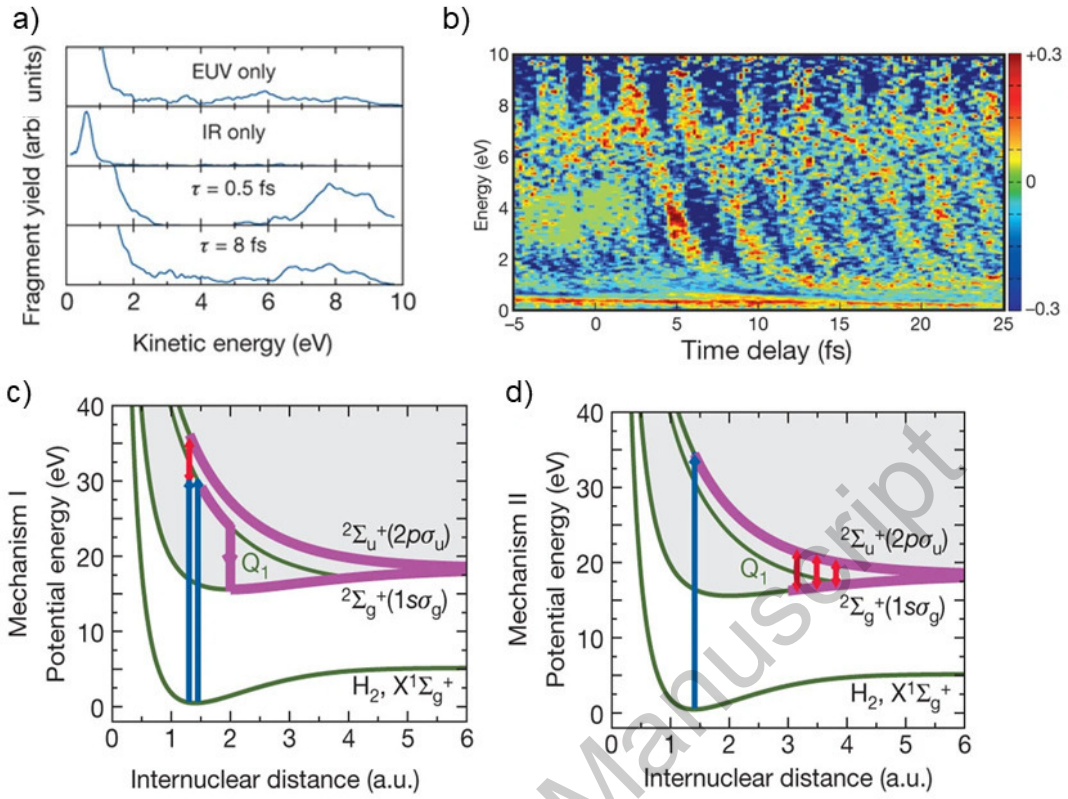

Figure 5. (a) Experimental kinetic energy distributions of D^+ fragments at selected time delays, compared with the distribution in the presence of the XUV or IR fields only. (b) Experimentally extracted asymmetry parameter as a function of the delay between the IR and XUV pulses: the map displays clear oscillations whose phase strongly depends on the kinetic energy. Mechanisms underlying the observed asymmetry in the dissociative ionization of hydrogen: (c) the IR probe acts in on the photoionization of the molecule or (d) on the dissociation of the molecular ion. Blue arrows represent XUV photons, red IR photons and purple internal paths. Adapted figure with permission from [53], Copyright (2010) by the American Association for the Advancement of Science.

as a function of the delay between the XUV and IR pulses. In absence of the IR there is a symmetric distribution of N_R and N_L since the electronic states $^2\Sigma_u^+(2p\sigma_u)$ and $^2\Sigma_g^+(1s\sigma_g)$ that can be accessed by one XUV photon absorption have opposite parities. The asymmetry is therefore the result of the coherent superposition of states of different parity but identical kinetic energy of the ion and angular momentum of the photoelectron, and can only be achieved in the presence of the IR field. The authors identified two different mechanisms leading to this scenario (Fig. 5, bottom panels): (I) the interference between the direct ionization through the $(^2\Sigma_u^+(2p\sigma_u)$ continuum by simultaneous absorption of an XUV and an IR photon and the autoionization decay into $^2\Sigma_g^+(1s\sigma_g)$ state and (II) the XUV ionizes to the $(^2\Sigma_u^+(2p\sigma_u)$ state and the IR pulse couples it to the $^2\Sigma_g^+(1s\sigma_g)$ surface. While the first mechanism occurs only when the XUV and IR pulses overlap, the second requires only the IR pulse to be intense during

the dissociation of the molecule. This work therefore demonstrated that it is possible to control the electron localization following dissociative ionization in hydrogen by using an appropriate timing of the IR field.

Using trains of attosecond pulses the role of the nuclear motion in the induced electron dynamics was investigated in D_2 [119].The experimental data on the fragment ion yields displayed oscillations with a period half of the IR optical cycle, which were explained as an interference between ionization pathways involving different harmonic orders and an IR-induced coupling between the states of the molecular ion. As a result of this IR-induced coupling, the dependence of the photoelectron spectra with the pump-probe delay is different with respect to that obtained from RABBITT measurements in atomic systems. A few years later, this scheme was extended by using trains of vacuum-UV (VUV) attosecond pulses tunable in the frequency domain to investigate the nuclear-electronic coupling. In their experiment, Ranitovic *et al.*[120] employed three different attosecond VUV harmonic combs, leading to the population of the $B^1\Sigma_u^+$ and $EF^1\Sigma_g^+$ states through different one and two- photon pathways. Each harmonic comb was used to create a different vibronic wave packet, which evolves along the potential energy surfaces of the $B^1\Sigma_u^+$ and $EF^1\Sigma_g^+$ states covering different regions of the internuclear distance. By using this approach, the authors demonstrated the coherent excitation of multiple wave packet dynamics, as well as a possibility of controlling bond-breaking and dissociation through the pathways in D_2.

More recently Cattaneo *et al.* made use of the RABBITT technique in combination with COLTRIMS to time resolve the coupled electron–nuclear dynamics in H_2 [121]. In the experiment, they pumped H_2 molecules with a train of attosecond pulses in the energy range 24–42 eV and probed with a weak IR pulse of about 30 fs and peak intensity between 1.4×10^{11} and 3.0×10^{11} W/cm^2. The XUV pulse train populates the cationic ground state $^2\Sigma_g^+(1s\sigma_g)$ for energies around 25 eV (resulting in molecular fragments with a kinetic energy release - KER - of about 1 eV), the first excited state of the ion $^2\Sigma_u^+(2p\sigma_u)$ for energies above 30 eV (resulting in 10-12 eV KER) and the doubly excited states Q_1 (for molecules oriented parallel to the XUV polarization axis) and Q_2 (for molecules oriented orthogonally). The two latter autoionize to $^2\Sigma_g^+(1s\sigma_g)$ and $^2\Sigma_u^+(2p\sigma_u)$, but the resulting ionic fragments have higher kinetic energy with respect to those from the direct path. It is thus possible to separate the paths leading towards Q_1 and Q_2 from the two molecular orientations (parallel and perpendicular to the XUV polarization). The associated KER (Fig. 6, panels a and b) contain in turn information on the ionization mechanism: the direct ionization gives a contribution to the KER between 0-2 eV, whereas the cross section for the autoionization is nonzero over a broad range of energy and therefore it is the only contribution above 2 eV. On the other hand, information on the coupled electron-nuclear dynamics can be inferred from the photoion-photoelectron spectra by exploiting the RABBITT technique (Fig. 6, panels c and d), which allows to extract the phase of the molecular wave packet. In this case

the oscillatory term in Eq. (1) reads

$$S_{2q}(\tau) \approx \cos(2\omega_{IR}\tau - \Delta\phi_q - \Delta\phi_{n-e}) \tag{6}$$

where ϕ_{n-e} is what the authors called the coupled nuclear–electron phase. By analyzing this phase as a function of both the electron kinetic energy and the KER, they demonstrated that the changes of the ionization phases with the nuclear kinetic energy can be as big as variations with the electron kinetic energy, meaning that the outgoing electron wave packet and the nuclear wave packet cannot be separated.

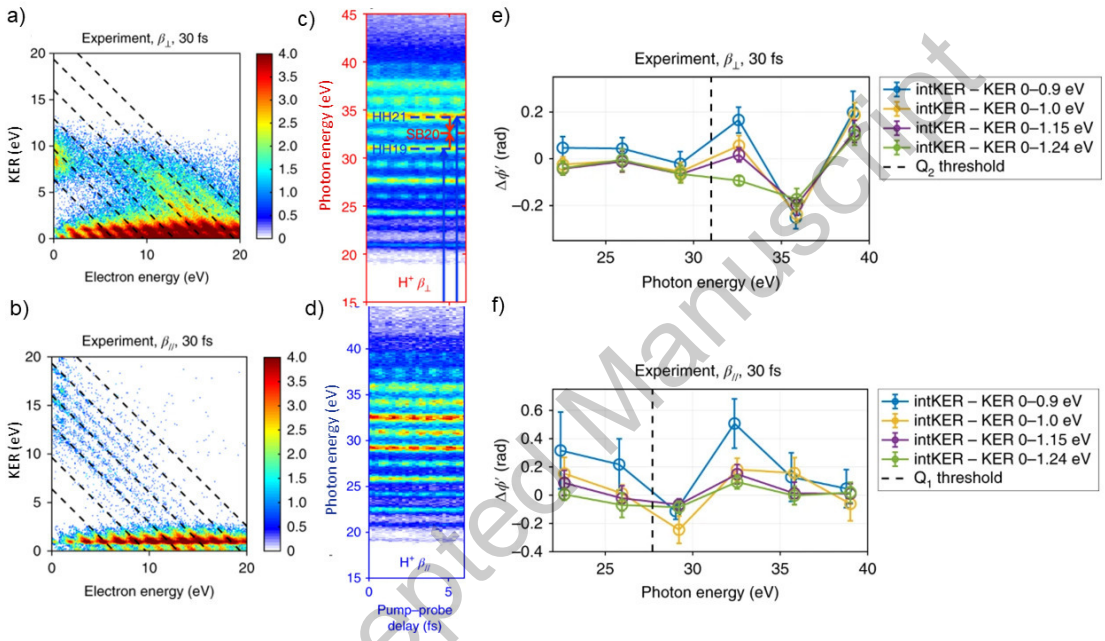

Figure 6. Experimentally measured KER as a function of the electron energy for (a) perpendicular and (b) parallel molecular orientations. (c) and (d) RABBITT traces of photoelectrons in coincidence with H^+ and (e), (f) extracted phase delays. Adapted figure with permission from [121], Copyright (2018) by Springer Nature.

In recent years considerable effort has been made to increase the photon flux from HHG sources to perform XUV pump - XUV probe experiments [10, 35, 122, 123]. The first experimental XUV pump-XUV probe measurement in a molecule was obtained by Carpeggiani *et al.* in H_2 [124]. A XUV pulse with a spectrum spanning from 12.5 to 18 eV excites a manifold of electronic states with the corresponding vibrational levels (Fig. 7a). The dynamics of the excited electronic and vibrational wave packets are probed through absorption of a photon from the second temporally delayed XUV pulse. Since the ionization potential for the dissociative channel in H_2 is 18.15 eV, this channel is only accessible by two-photon absorption and therefore it can be used as an observable to track the electron-nuclear coupling dynamics [125]. In the experiment, they observed a minimum at zero delay and a subsequent increase of the proton yield in the first 1 fs (Figs. 7b,c), which is rationalized as follows: at $\tau = 0$ fs the dissociation pathway

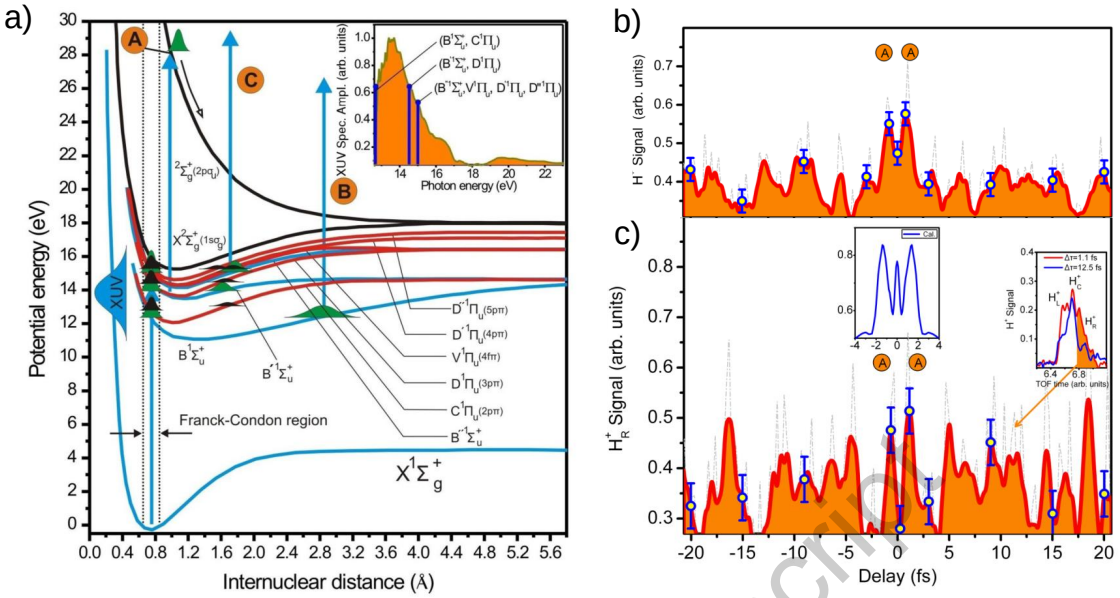

Figure 7. (a) Energy diagram of H_2: a first XUV pump pulse (blue arrow, spectrum shown in the inset) creates a wave packet over the states comprised between 12.5 and 18 eV. A second XUV pulse is then used to track the dynamics triggered by the pump in a two-photon scheme: with increasing internuclear distances (i.e., the molecule stretches) the second ionization threshold $2p\sigma_u$ opens, leading to ionization with nonzero energy protons. Experimental traces of (b) the total proton yield and (c) the yield of nonzero kinetic energy photons. A local minimum is observed at $\tau = 0$ fs succeeded by a build-up, which is attributed to the dynamics of the opening of the dissociation channel through the $^2\Sigma_g^+(2p\sigma_u)$ channel. Adapted figure with permission from [124], Copyright (2014) by the American Physical Society.

through the $^2\Sigma_g^+(2p\sigma_u)$ is mainly closed but, due to the stretching of the molecules, it becomes accessible from the intermediate states after 1 fs.

A similar scheme, but using trains of attosecond pulses was employed by Midorikawa and co-workers to demonstrate the control of the dissociation pathway originating from the $2p\sigma_u$ state against that from the $2p\pi_u$ state in molecular hydrogen [126]. To this end the authors generated a XUV comb composed by the 3rd to the 19th harmonics. The duration of the corresponding attosecond pulse train was estimated to be around 4 fs with an energy exceeding 1 μJ, which allowed them to split the pulse in two replicas with sufficient energy to perform the experiment. The H^+ fragments were mapped as a function of the delay between the two replicas in a VMI spectrometer. The harmonics 3 to 11 excite the $2p\pi_u$ state (Fig. 8a) and are therefore correlated to the signals in the KER spectra of the H^+ fragments parallel to the polarization direction of the pulse train; in contrast, the 9th-, 11th- and 13th-harmonic components are responsible for the signatures in the perpendicular direction, since they populate the $2p\pi_u$ state (Fig. 8b). The spectra showed clear oscillations in the H3 and H5 KER components as a function of the scanning delay (Fig. 8a) due to the interference due to the vibrational motion of the wavepacket created in the $1s\sigma_g$ state. Similarly the H9 and H11 KER components

oscillate between 0 and 280 fs (Fig. 8b), equal to the time of the half-revival of the vibrational wave packet. Based on this, the authors demonstrated a route to switch between the two dissociation pathways. At 8 fs before the time of the half-revival of the wavepacket the vibrational wavepacket is confined around the inner turning point in the $1s\sigma_g$ curve. Due to the close photon energy of the H9 with the energy difference between the $1s\sigma_g$ and $2p\sigma_u$ states at the inner point, the photoexcitation with the 9^{th} harmonic should favour this transition (Fig. 8c, upper panel). After the half-period of the vibrational motion (8 fs), the wave packet reaches the outer turning point, where the H9 is energetically closer to the transition to the $2p\pi_u$ state (Fig. 8c, bottom panel).

Further progress in attosecond XUV pump-XUV probe experiments requires phase-locked XUV pulses, which would allow for example to retrieve the excitation dynamics and identify both electronic and nuclear phases [125, 127]. Recent developments in free electron lasers have been proved to be very promising in this direction [128–130].

2.3.2. Small and medium size molecules The experiments discussed in Sect. 2.3.1 paved the way towards the investigation of electron dynamics in molecules of larger complexity. In the case of diatomic molecules, extensive studies have been performed in O_2, CO and N_2.

By varying the relative delay between an IR field and an attosecond pulse train, Siu *et al.* showed a dependence of the branching rations of different ionic fragmentation channels in O_2 [131]. A similar scheme was employed in [132], but this time using a reaction microscope for the detection: by measuring over a large pump-probe delay range, the authors were are able to resolve the first (half-)revival of the wave packet (40 fs). This oscillation is caused by a time-dependent vibrational wave packet in the potential of the binding $O_2^+(a^4\Pi_u)$ state, which is then probed by resonant absorption of an IR photon to the $O_2^+(f^4\Pi_g)$ state. By comparing the experimental spectra with coupled-channel simulations, the authors were able to discriminate between the calculated adiabatic cation potential energy curves. The autoionization process has also been investigated with few-femtosecond x-ray pulses [133], which populate the super-excited states of the $O_2{}^+$ molecular ion. This state evolves into an autoionizing state, but this decay can be interrupted by interaction with an ultrashort laser pulse. This allowed the authors to determine the minimum internuclear separation of the fragments for autoionization to happen (about 30 Å) and the onset of Feshbach resonances of the neutral oxygen atom.

Dissociative ionization of N_2 has been widely studied using attosecond pulse trains [134, 135], femtosecond time-resolved photoelectron and photoion spectroscopy [136] and isolated attosecond pulses [137]. Precise information on the shape of the potential energy surfaces involved in the dissociative ionization process was extracted by exploiting isolated attosecond pulses [137]. Particularly interesting are the results with attosecond pulse trains. The angularly-resolved pump-probe measurements in [134] showed that, in contrast with what previously observed in other diatomic molecules, autoionization becomes energetically allowed when the two nuclei are still very close (about 3 Å).

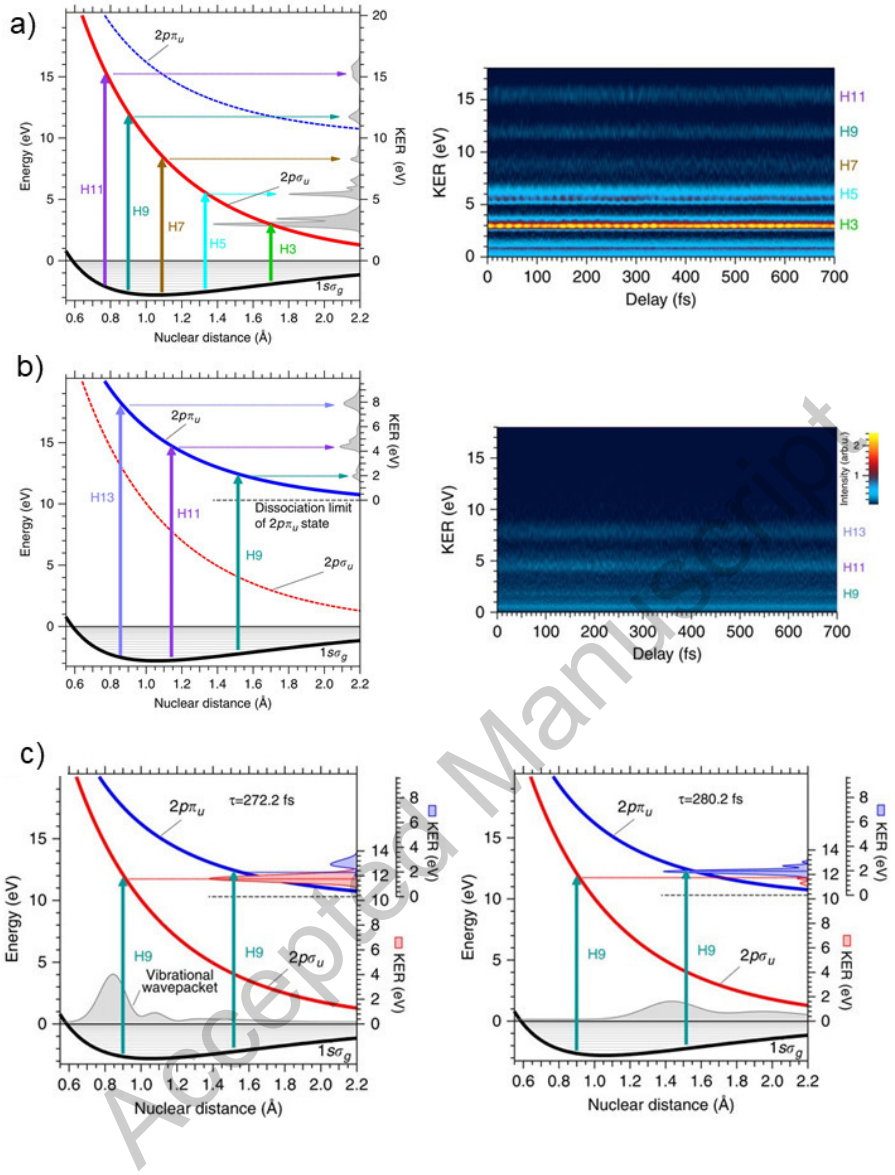

Figure 8. Schematic figure of the one-photon excitation from the ground $1s\sigma_g$ state (a) to the repulsive $2p\sigma_u$ state and (b) to the $2p\pi_u$ state in the molecular ion. The right hand side panels show the corresponding time-resolved KER spectra. (c) Potential curves of the $1s\sigma_g$ (black), $2p\sigma_u$ (red) and $2p\pi_u$ (blue) states. The KER spectra of the H^+ fragments generated via one-photon absorption to the $2p\sigma_u$ and the $2p\pi_u$ states are shown in the right axis as red and blue shaded areas, respectively. Left panel: excitation with the H9 efficiently populates the $2p\sigma_u$ state when the vibrational wave packet is localized around the inner turning point. Right panel: the vibrational wave packet arrives at the outer turning point and one-photon absorption from the 9^{th} harmonic efficiently populates the $2p\pi_u$ state. Adapted figure from [126].

Haessler *et al.* experimentally characterized the phase of the two-color two-photon ionization transition for different states of the ion [135]. Recalling Eq. (1), the intensity of the sidebands oscillates as:

$$S_{2q}(\tau) \approx \cos(2\omega_{IR}\tau - \Delta\phi_q - \Delta\phi_{mol}) \tag{7}$$

where $\Delta\phi_{mol}$ is the molecular phase. In order to isolate this term it is thus necessary to retrieve first the contribution of the XUV phase, $\Delta\phi_q$, which is done by performing a separate measurement in Ar. This analysis was applied to extract the molecular phases as a function of the sideband order for each ionization channel. As it can be seen in Fig. 9, most of the measured values for both channels rely around 0 rad, except for the 12^{th} sideband in the X state. In particular the authors measured a value of -0.35π rad for the electrons produced in the ionization channels leading to the $X^2\Sigma_g^+(v' = 0)$ state and -0.9π rad for $X^2\Sigma_g^+(v' = 1, 2)$ states. This behaviour was attributed to the presence of a resonance in the in the vicinity of the 11^{th} harmonic. This study represents a fundamental step towards the characterization of attosecond photoionization time delays in molecules, a hot topic in attosecond science in the last few years.

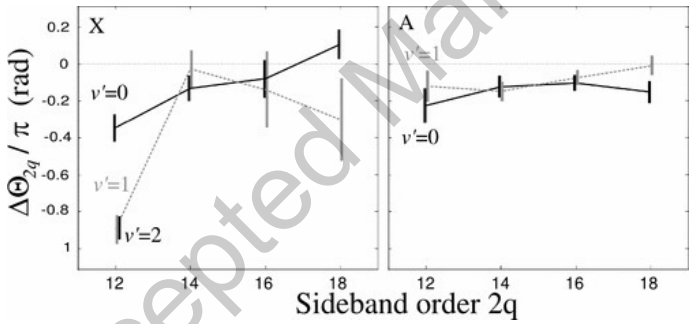

Figure 9. Experimental molecular phase difference as a function of the sideband order for the X and A states in N_2. Adapted figure with permission from [135], Copyright (2009) by the American Physical Society.

Beyond diatomics, the first extension of attosecond methods to the study of small- and medium-sized neutral molecules (N_2, CO_2 and C_2H_4 was reported by Neidel *et al.* [138], who monitored the time-dependent variations of the parent molecular ion yield using a two-color scheme: a moderately intense 30-fs IR pulse serves as the pump, whereas an XUV attosecond pulse train is used as a probe. The measured fragment yields presented pronounced oscillations as a function of the pump-probe delay. For N^{2+} ions, the amplitude of the oscillations is about 1%-2% with a period equal to half the fundamental pulse. Similar in-phase modulations were observed for N^+, indicating that the total ionization yield oscillates as a function of the pump-probe delay. This suggests that IR field induces a time-dependent molecular dipole moment giving rise to a time-dependent redistribution of the electronic density, which modulates the photoionization yield of the molecule. The amplitude of such oscillations was found to correlate with the magnitude of the molecular polarizability.

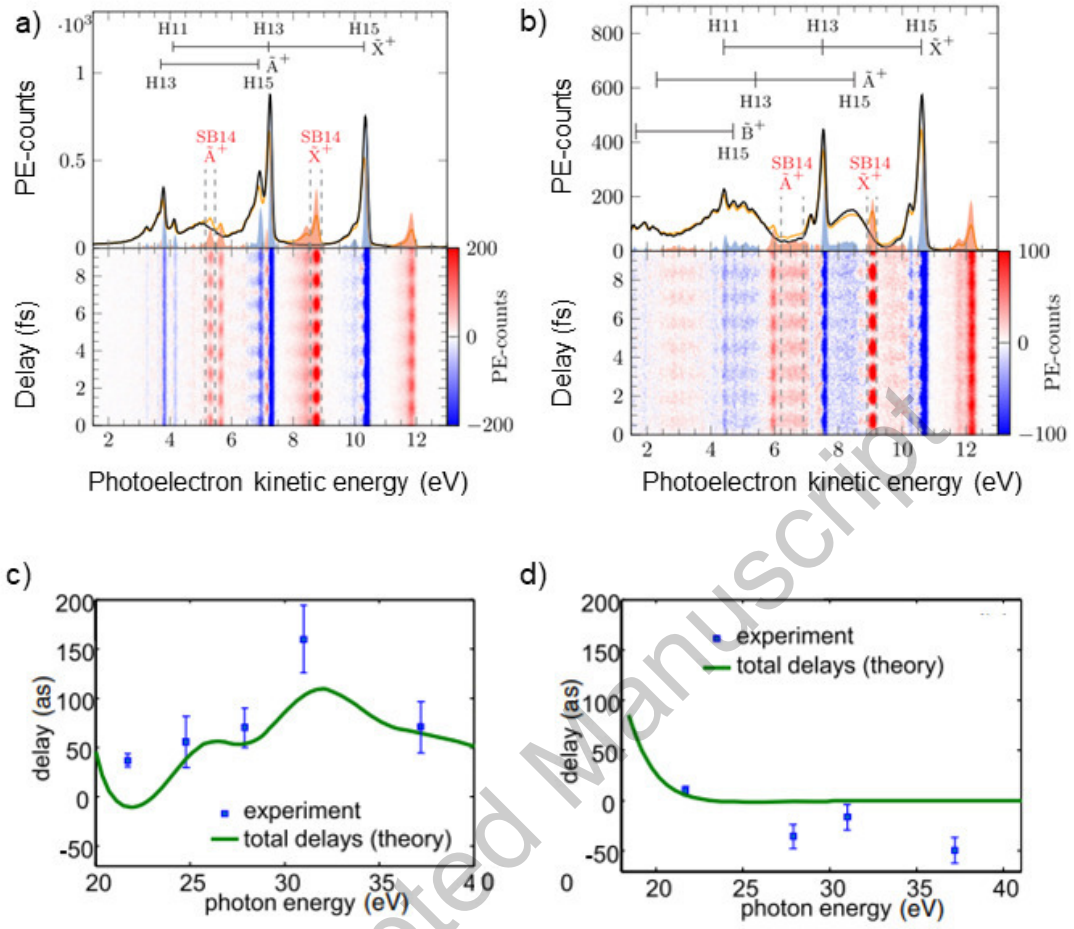

Figure 10. Photoelectron spectrum and difference spectrum as a function of the IR-XUV delay for a)N_2O and b) H_2O. Experimental molecular phase difference as a function of the sideband order for the X and A states in c) N_2O and d) H_2O. Adapted figure with permission from [139], Copyright (2016) by the American Physical Society.

As for atoms, interferometric measurements with trains of attosecond pulses enable the retrieval of attosecond photoionization delays in molecules. RABBITT measurements by Wörner's group [139] reported photoemission time delays in N_2O and gaseous water. For the experiment, trains of attosecond pulses were generated in Ar, which were recombined with the dressing IR pulse in an actively-stabilized beamline. Upon the interaction of the pulses with the molecular jet, photoelectron spectra were collected with a magnetic TOF spectrometer. Importantly, the XUV pulse train was spectrally filtered by thin metal foils. This removes the spectral overlap inherit to the broad bandwidth of attosecond pulses, which had previously prevented to extract time delays due to the congested spectra. In the case of N_2O delays up to 16 as were found in the 20-40,eV energy range, while in H_2O delays below 50 as were measured at the same photon energies. Panels (a) and (b) in Fig. 10 show the difference spectra, obtained

by subtracting the XUV only measurements from the spectra in the presence of the IR field, performed in N_2O and water when filtering the harmonics 11, 13 and 15 (black line). The spectrograms display two modulated sidebands (SBs), assigned to the SB14 of $\tilde{A}^+$ and SB14 of $\tilde{A}^+$. By Fourier transforming with respect to the delay axis, it is possible to extract the phases and therefore the relative time delay between the SB14 of $\tilde{A}^+$ and $\tilde{A}^+$ states. For N_2O this amounts to 35 as, while for water is about 10 as. Similar measurements were performed using different filters covering up to 40 eV. As it can be seen in panels (c) and (d) in Fig 10, delays as big as 160 as were measured for N_2O, while for water it is limited to 50 as. These large delays observed in N_2O were assigned to the trapping of the photoelectron in a molecular shape resonances.

The same experimental approach was applied for the investigation of photoemission delays in liquid water [140], being the first measurement of attosecond electron dynamics in liquids. To this end Jordan *et al.* combined the spectral filtering [88, 139] and the energy-dependent analysis of the sideband oscillation phases [91, 107] with the complex-valued principal components analysis. Liquid water was introduced into a vacuum chamber through a 25-μm nozzle; evaporation from the jet created gas-phase water in the surroundings. A XUV pulse train together with a 30 fs IR pulse were focused onto the liquid microjet, simultaneously measuring the electron contributions from both the liquid and gas phase water molecules. Signals from the liquid phase could be isolated since they were shifted and broadened with respect to the gas phase contributions. By applying Eq. (7) to the Fourier transform of the spectrograms (Fig. 11) photoemission time delays of 69 as and 49 as were obtained for the 14^{th} and 20^{th} sidebands, respectively. To rationalize these observations the authors developed a theoretical model combining the description of time delays at quantum mechanical level with a semiclassical-trajectory Monte Carlo simulations of electron transport. These calculations allowed to discriminate between the contribution of the local environment (solvation) and electron transport to the photoemission time delays, concluding that the latter was negligible.

The works regarding photoemission delays we have reviewed up to now do not consider the anisotropy in the molecular frame (i.e. the delays are an average over all possible orientations of the molecule). If one could gain access to the angular dependence of the photoemission delay, it would give direct information on the localization of the electron wavepacket within the molecular potential. This concept was first introduced in a theoretical study by Chacon *et al.* [141], who termed the relative delay between electrons emitted to the left and right in an asymmetric system as stereo Wigner time delay:

$$\tau_{SW} = \tau_W(left) - \tau_W(right) \tag{8}$$

where τ_W is the Wigner delay time [73] (i.e. the energy derivative of the scattering phase of the electron wave packet receding in the field of the ion).

Therefore by properly imaging the charged fragments after dissociation in a diatomic molecule, the timing measured for different recoil angles could be linked to the specific spatial region of the molecule where the electron wave packet originated. This

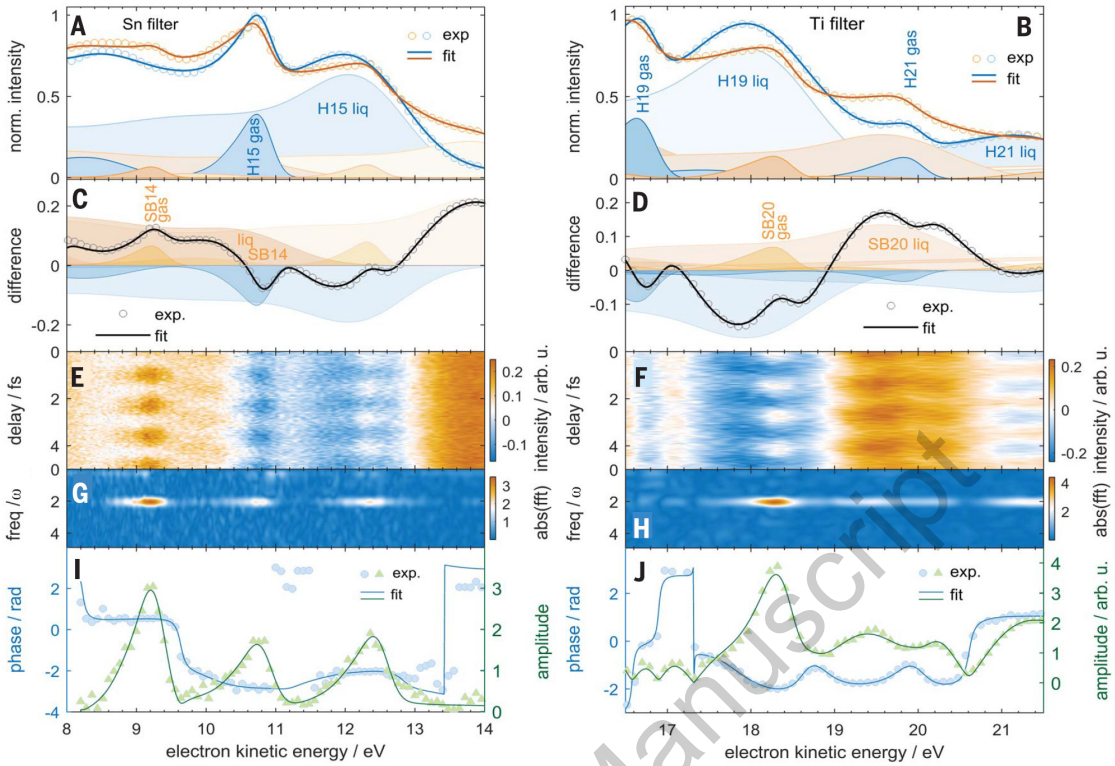

Figure 11. A and B show the photoelectron spectra of the XUV only data (blue) or in presence of the IR field (orange) together with the decomposition in their principal components. C and D are the difference spectra of the spectra in the presence and absence of the IR field. Difference spectrograms are displayed in E and F, with the corresponding Fourier-transform power spectra in G and H. Panels I and J show the amplitude and phase of the 2ω component of the Fourier transform. From [140]. Reprinted with permission from AAAS.

was actually demonstrated by Keller's group in carbon monoxide (CO) by combining the RABBITT technique with a COLTRIMS detection scheme. In such case Eq. (8) reads:

$$\tau_{SW} = \tau_W(Cside) - \tau_W(Oside) \tag{9}$$

In their experiment, photoionization dynamics was initiated by a train of attosecond pulses with a bandwidth extending from 23 o 42 eV. A portion of the driving IR pulse serves as a perturbative field. The two beams are then focused into a supersonically expanded cold jet of CO molecules and the angle-resolved momenta of the fragment ions and electrons are detected with the COLTRIMS apparatus.

After excitation three ionization channels can be accessed: the direct photoionization channel ($CO+h\nu \rightarrow CO^+ + e^-$) and two dissociative photoionization pathways ($CO+h\nu \longrightarrow C^+ + O + e^-$ and $CO+h\nu \longrightarrow O^+ + C + e^-$). The study focuses on the dissociative ionization channel involving the C^+ fragment. Due to the large bandwidth XUV pulses, electrons with overlapping energy distributions are released from ionization with different harmonics. This prevents the assignment of fragment ion

to an individual electronic state. Instead, in this work the relative contribution of the electronic states was enhanced by discriminating between dissociation events where the recoil axis is oriented parallel ($\beta_{\parallel}$) or orthogonal ($\beta_{\perp}$) to the XUV polarization. KER spectra for parallel (blue) and perpendicular (orange) orientations are shown in Fig. 12. Two peaks can be distinguished in the spectrum of perpendicularly oriented molecules: one around 1 eV (noted as low KER) and one around 3.9 eV (high KER). Quantum nonadiabatic dynamics simulations based on the multireference configuration interaction (MRCI) and nonadiabatic couplings allowed to determine the ratios of dissociation into the $C^+ + O$ channel for individual electronic states and therefore the contributions of states to the ($\beta_{\parallel}$) and ($\beta_{\perp}$) KER spectra. The former is dominated by $^2\Sigma^+$ states, whereas the latter has contributions from the $D^2\Pi$ and the $3^2\Sigma^+$ states (low KER) and $3^2\Pi$ state (high KER).

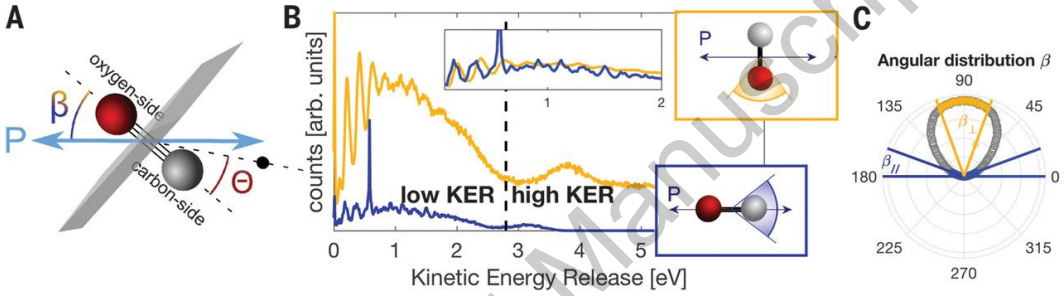

Figure 12. a) Scheme showing the system geometry and the recoil angle with respect to the laser polarization axis P, indicated by β.The dotted line and the black spot represent the escaping side of the electron wave packet. b) KER spectra separated for molecules oriented perpendicular (orange) and parallel (blue) with respect to the polarization axis. c) Angular distribution of the recoil angle with respect to the field polarization axis. Adapted figure with permission from [142], Copyright (2018) by the American Association for the Advancement of Science.

Once the data are decomposed into the RABBITT traces for the parallel and perpendicularly oriented molecules, one can extract the molecular phase delay from Eq. (7). The term $\Delta\phi_{mol}$ in Eq. (7) can be decomposed by the sum of two terms: $\Delta\phi_{mol} = \Delta\phi_W + \Delta\phi_{CC}$, where $\Delta\phi_W$ is the Wigner phase and $\Delta\phi_{CC}$ is the measurement-induced phase term originating from the continuum-continuum transition in the IR field. Since here one is interested in evaluating the stereo Wigner time delay, the term $\Delta\phi_{2q}$ (attochirp, inherent to the XUV pulse) cancels out and so does the term $\Delta\phi_{CC}$ (symmetric contribution of the long-range Coulomb potential). The stereo Wigner time delay can be therefore calculated from the RABBITT traces as:

$$\tau_{SW} = \frac{\tau_W(Cside) - \tau_W(Oside)}{2\omega} \tag{10}$$

The experimentally obtained values of τ_{SW} as a function of the electron energy are displayed for the two molecular orientations in Fig. 13. For perpendicularly oriented molecules the stereo Wigner delay times lie around 0 as ($\pm$351,as). This

trend is expected from symmetry considerations and further supported by numerical calculations. Molecules oriented parallel to the light polarization present instead an evolution from negative delays (-165 as at 5 eV) towards positive values (+30 as at 14.4 eV). This change in the sign implies that the stereo Wigner delay changes from $\tau_W(Cside) < \tau_W(Oside)$ (i.e. the electron wave packet escapes into the continuum via the C-site) to its inverse with increasing electron kinetic energy.

To elucidate the origin of this behaviour, two theoretical approaches were implemented: one based on the time-dependent resolution in ionic states method [143] and the second based on the combination of the approximate, classical propagation of the Wigner function of the photoelectrons with the quantum nonadiabatic dissociation dynamics. The joint interpretation of the experimental results and the numerical calculations allowed the authors to conclude that the negative delays at low energy arise from the initial localization of the electron wave packet in the carbon side of the molecules. It was thus concluded that photoelectrons originating from the dissociative ionization process of the CO molecule are preferentially emitted from the carbon end for dissociative Σ states and from the center and oxygen end for the 2Π states of the molecular ion. As we have seen in the previous examples, the broad bandwidth of

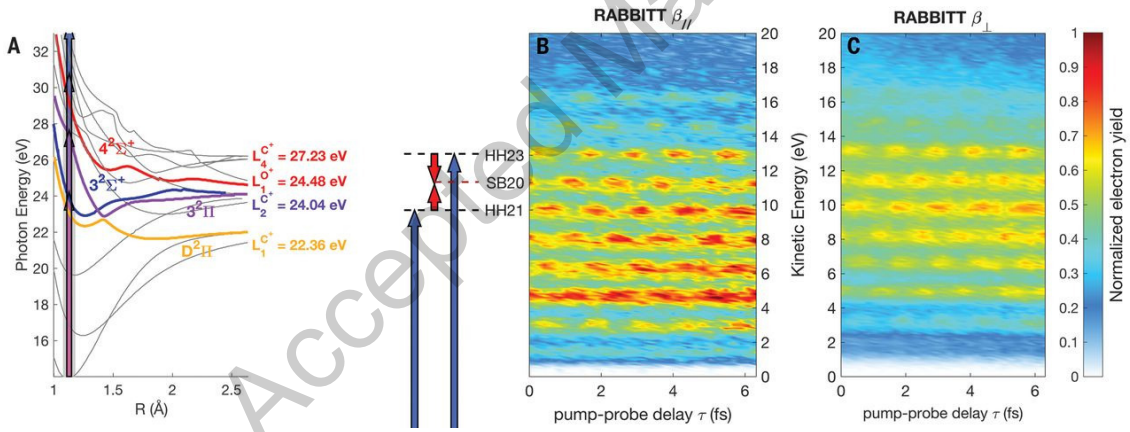

Figure 13. a) Potential energy surfaces of the CO^+ molecular ion (the most relevant states involved in the dissociative ionization are highlighted in red, purple, blue and yellow). RABBITT traces for molecules oriented b) parallel and c) perpendicular along laser polarization. Adapted figure with permission from [142], Copyright (2018) by the American Association for the Advancement of Science.

attosecond pulses and the close-lying levels at XUV photon energies, renders it very difficult to discriminate the correct initial electronic states based on the final electron energies. In addition, it is quite complex to disentangle the two steps in the ionization process (initial ionization of the electron and propagation of the electron wavepacket in the molecular potential) since no reference is available. Very recently Kling and co-workers demonstrated the potential of measuring photoemission delays to obtain sensitive information about the role of a functional group in a molecule if an inner shell reference is available [144]. To this end they measured the photoionization delay by

means of attosecond streaking in a polyatomic molecule (ethyl iodide) around a giant dipole resonance. Since this resonance is inner shell characteristic, it is largely unaffected when an atom becomes part of a larger molecule. This allowed the authors to use as a reference the iodine atom and disentangle the contribution of the functional group, finding a substantial additional delay ($\approx 38as$) caused by its presence.

2.3.3. Large polyatomic molecules With the advent of femtosecond spectroscopy[145, 146], many efforts have been concentrated on the investigation of the photo-induced dynamics in bio-relevant molecular systems such as photosynthetic complexes[147–149], proteins and aminoacids or the DNA subunits[150–153]. The response of many of these molecules is dictated by ultrafast processes that determine the ultimate chemical change. As a remarkable example, DNAs subunits exhibit efficient non-radiative decay pathways upon UV-photoexcitation on time scales ranging from sub-picosecond in isolated nucleotides to few hundreds of picoseconds in DNA strands [150, 154]. This efficient energy dissipation prevents the trigger of a chain of photochemical reactions that could end up on a photodamage of the base sequence. On even faster time scales, the electron delocalization occurs along the backbone chains of DNA in ca. 740 as [155].

Theoretical studies have shown that efficient charge transportation solely driven by electron correlation - taking place in temporal scales ranging from few femtoseconds down to tens of attoseconds - can precede any rearrangement of the nuclear skeleton [156]. This ultrafast charge transfer has been termed as charge migration. While charge transfer is predominantly mediated by the nuclear dynamics, charge migration is specifically driven by purely electronic effects (for a detailed review in this topic we refer the reader to Ref. [157]). Due to the rapid time scales in which charge migration takes place, its experimental investigation was possible only recently, upon the generation of attosecond pulses.

Prior to the development of attosecond light sources, the experiments on fragmentation of small peptides by Weinkauf *et al.* [158–160] motivated the investigation of charge migration from a theoretical perspective [161–165]. In these experiments, it was found that although a positive charge was originally generated on a given specific site of the molecule, the fragmentation had occurred at a different location. For instance, in [158] the analysis of the fragment mass spectra of a leucine-tryptophan dipeptide after two-photon UV excitation revealed a predominant peak of mass 86 Da, which corresponds to a positive charged N-terminal fragment (leucine). However, local ionization was performed at the aromatic amino acid (tryptophan), which is located at the C-terminal side of the peptide (see Fig. 14). Similar observations were reported for 2-phenylethyl-N,N-dimethylamine (PENNA) and phenylalanine. In the first case femtosecond spectroscopy experiments proved that after ionization of the phenyl chromophore, the charge is transferred to the amine site with subsequent fragmentation leading to the immonium cation [166, 167]. As for phenylalanine, pump-probe measurements with 1.5 fs XUV pump pulses and 6 fs IR probe pulses showed a fast biexponential decay (time constants of ≈ 10 fs and ≈ 25 fs) in the doubly charged

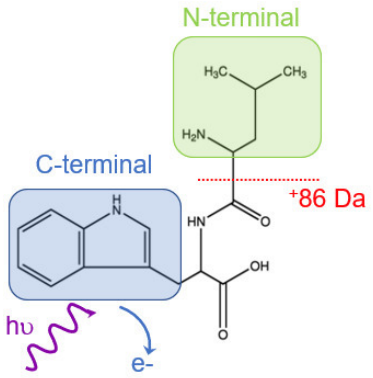

Figure 14. Schematic molecular structure of dipeptide of type leucine-tryptophan. Photoexcitation is realized at the chromophore side (C-terminal) Fragments with mass 86 Da can be explained only by electron migration from the N-terminal side to the chromophore residue.

immonium ion [168].

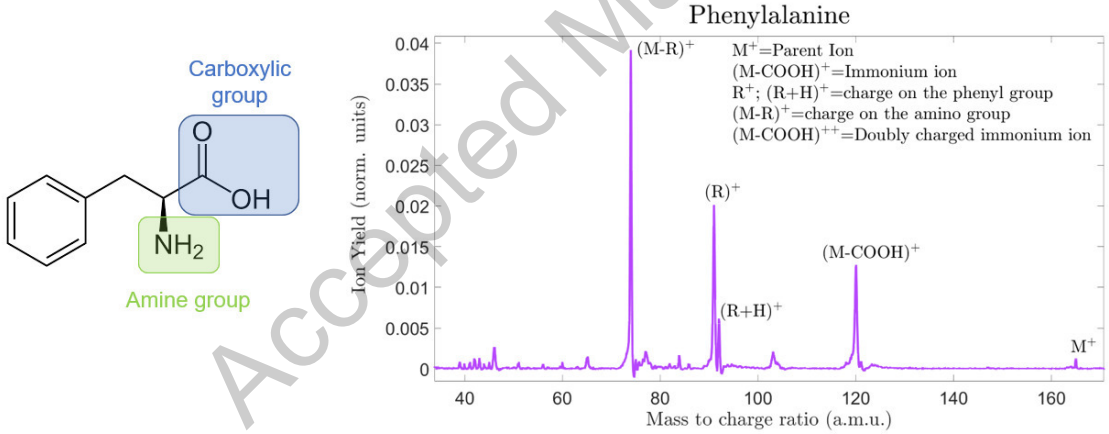

Figure 15. Molecular structure of phenylalanine and mass spectra obtained after ionization with an XUV pulse (see details in the text).

Direct proof of charge migration dynamics was only obtained in 2014 by Nisoli's group using XUV pump - IR probe with isolated attosecond pulses in phenylalanine [54] and one year later by Woerner's group using high-harmonic spectroscopy in iodoacetylene [169]. Here we will focus only on the first work, since high-harmonic spectroscopy is beyond the scope of this Review. In their work, Calegari *et al.* utilized isolated 290 as pulses, with a photon energy extending from 17 to 35 eV, to trigger prompt ionization. The chemical structure of phenylalanine and the mass spectrum resulting from ionization with an XUV pulses are shown in Fig. 15. The subsequent response of the system was probed with 4 fs IR pulse centered at 1.77 eV, which produces a doubly charged molecular fragment (immonium ion, mass/charge = 60) by ejection of

a second electron. The analysis focuses on the temporal evolution of this photofragment, whose yield is monitored as function of the pump-probe delay.

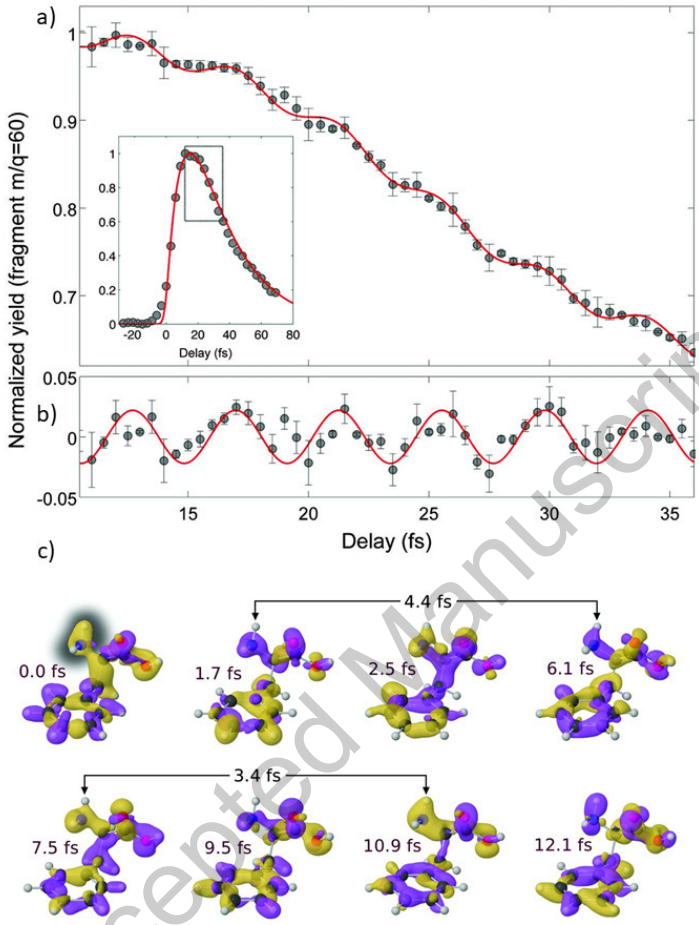

Figure 16. Pump-probe measurements in phenylalanine with isolated attosecond pulses: yield of doubly charged immonium ion (mass/charge = 60) as a function of pump-probe delay, measured with 3-fs time steps (inset) and with 0.5-fs temporal steps (main). b) Experimental data after subtraction of the exponential fitting (gray line in a). b) Snapshots of hole dynamics obtained by numerical simulations showing the relative variation of the hole density (yellow means positive hole density, whereas purple means negative). Adapted figure with permission from [54], Copyright (2014) by the American Association for the Advancement of Science.

Figure 16 shows the experimental data: on a 100-fs time window (inset in Fig. 16) the data are best fit with a build up time of 10 fs and an exponential decay with time constants of about 25 fs. A close look into the dynamics from 15 to 35 fs with finer time steps reveals an oscillatory pattern on top of the decay with a beating period of ca. 4.3 fs (Fig. 16b). A Gabor transform analysis of the oscillations finds frequency components at 0.14 PHz and 0.3 PHz dominating the response on the first 15 fs. This is followed by a broad component at 0.24 PHz, which forms and decays in 35 fs, spectrally

broadening with increasing pump-probe delay. Since the fastest stretching evolves in 8.9 fs (0.11 PHz) one can rule out that the observed 4.3 fs oscillations are due to vibrational motion (although the influence of nuclear motion cannot be excluded at longer delays). Therefore the authors attribute the periodic beating to a charge motion of purely electronic origin. This hypothesis was supported by theoretical calculations, which found that the temporal modulation of the hole dynamics maximizes around the amine group in spite of the initial delocalization of the charge.

Further studies conducted with the same experimental scheme have been performed in other amino acids, such as tryptophan [55, 170] or glycine [171].

More recently attosecond spectroscopy has been employed to investigate the response of DNA subunits (thymine [172] and adenine [173]) to highly-energetic radiation. In addition to the UV-induced photodamage, tissue and DNA can be exposed to high-energy ionizing radiation, for example during therapy of tumors. Actual DNA damage is mainly occurring via secondary electrons or radical molecules generated in water (the most abundant molecule in human tissue). The energy of the XUV photons perfectly matches that of the secondary electrons, providing a perfect benchmark to study the interaction of DNA with ionizing radiation. Mansson *et al.* investigated the correlation-driven charge migration process after ionization with a XUV attosecond pulse in adenine [173]. Their results show that the hole created in the inner valence by the XUV pulse decays with a distinctive transition period, which can lead to the excitation of a second electron into a bound excited state known as the shake-up state. By properly timing the IR pulse it is possible to generate intact doubly charged adenine via a second ionization event.

An alternative approach for the study of photoionization dynamics relies on multiphoton ionization by 400 nm pulses introduced by Zipp *et al.* [174]. Similarly to RABBITT, an IR dressing field is used to create photoelectron sidebands that can be accessed from two interfering paths. It is important to remark that, differently from RABBITT, the phase shifts measured by this technique can be attributed to a temporary retrapping of a photoelectron [175].This scheme has been successfully applied by Beaulieu *et al.* [176] to study the photoionization of chiral molecules. Depending on the helicity of light and the handedness of the molecules, the ejected photoelectrons from enantiopure chiral molecules can go forward or backward with respect to the light propagation axis. As a consequence, the angular distribution of the photoelectrons present an asymmetry, known as photoelectron circular dichroism. In their work, Mairesse and co-workers investigated the relative photoemission delays between electrons ejected forward and backward from a chiral molecule.

In the experiment, above-threshold ionization (ATI) is induced in camphor, a prototypical chiral molecule, with a 400-nm circularly polarized field. A weak co-propagating IR field serves as probe and detection of the photoelectron distribution is angularly resolved with a VMI spectrometer. The overlap of the 400-nm pulse with a weak IR pulse induce additional transitions, giving rise to sidebands between the main ATI peaks. As in RABBITT, the sidebands oscillates as a function of the delay between

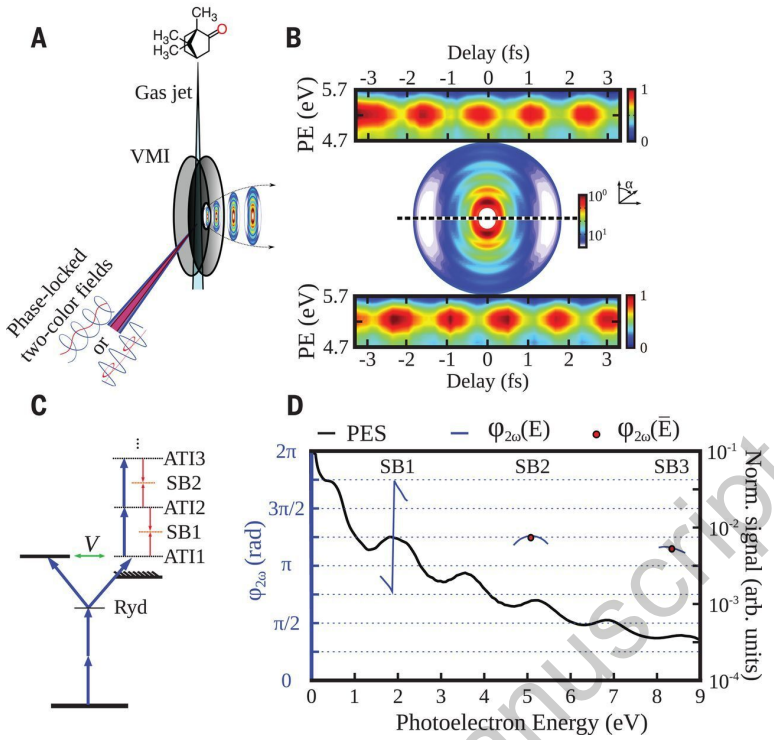

Figure 17. a) Scheme of the two-color multiphoton ionization approach. b) Experimental photolectron angular distribution and evolution of the second sideband as a function of delay between the two pulses. The π shift in the oscillations between the upper and lower half of the detector is due to the up-down asymmetry of the total ionizing electric field. c) Ionization scheme. The 400-nm pulse induces multiphoton ATI, whereas the 800-nm pulse produces additional transitions, leading to the creation of sidebands between the ATI peaks. d) Angle-integrated photoelectron spectrum. From [176]. Reprinted with permission from AAAS.

the two pulses. The phase of these modulations encodes the relative phase between the two adjacent ATI peaks and, which contains information on the time delays of the photoemission process. By comparing the phases of the sideband oscilations for the backward and forward electrons, the authors concluded that photoionization of camphor with circularly polarized light presents asymmetric delays in photoemission, of about 24 as in direct nonresonant photoionization.

2.4. TR-photoelectron spectroscopy in solids

Since the demonstration of the photoelectric effect towards the end of the nineteenth century [177], photoelectron spectroscopy (PES) has been used to investigate the electronic properties of solids [178]. In combination with ultraviolet (UV) photons, PES (also referred to as UPS, ultraviolet photoelectron spectroscopy) can be used to study the valence band states, i.e. those electrons that are less bound and that mostly determine the electrical properties of the system. Complementary information can be obtained with X-ray excitation (XPS, X-ray photoelectron spectroscopy). XPS gives access to

the core levels, characterized by higher binding energies. If combined with simultaneous detection of the angle of emission, PES can be used to map the electron dispersion in the energy-momentum space [179–181]. Angular resolved photoemission spectroscopy (ARPES) thus becomes a powerful tool to access the momentum-dependent electronic band structure of solids. First experiments were performed using the emission lines of discharge lamps like helium lamps (He I_α: 21.33 eV and He II_α: 40.82 eV), X-ray anodes like aluminium (Al-$K_{\alpha 1,2}$: 1486.6 eV) or magnesium (Mg-$K_{\alpha 1,2}$: 1253.6 eV) and synchrotron radiation [178]. These experiments mainly give direct information about the occupied states in the solid at the equilibrium, but when used with pulsed sources in a pump-probe scheme, ARPES can also give access to the unoccupied bands and electron dynamics.

The discovery of the HHG [2, 182] constituted an important step forward for time-resolved ARPES (tr-ARPES) in the hundreds-of-femtoseconds regime, in the spectral region from UV to soft-x-ray [183, 184], with a table-top setup, so that Single harmonics can be selected with multi-layer mirrors [185] or with monochromators [186–188], in order to obtain the required energy resolution. So far, HHG-based tr-ARPES has been successfully used in various applications with a resolution ranging from hundreds down to almost 10 fs. Remarkable examples are the studies of phenomena like: carrier dynamics at semiconductor surfaces [189], energy relaxation in photoexcited quartz [190], fast relaxation dynamics of atomic xenon adsorbed on a platinum [191], decay of excitations on a dye-doped organometallic material [192], hot-electron dynamics from platinum surface [193], transient surface voltage in optically excited semiconductors [194], photoinduced vaporization of charge-ordered state in the potential excitonic insulator 1T-$TiSe_2$ [195], melting transition of charge and lattice order in 1T-TaS_2 [196], a time-domain classification of charge-density-wave insulators [197], mapping the transient valence band structure of Gd during ultrafast demagnetization [198], anomalous femtosecond quasiparticle dynamics of hidden order state in URu_2Si_2 [199], and non-equilibrium distribution and thermalization events in graphene [200, 201].

Despite the plethora of interesting phenomena already accessible with femtosecond resolution, important fundamental physical processes happening in solids, like electronic screening [202–204], collective plasmonic excitation [205, 206], interfacial charge transfer [207] and transport [44, 208], are expected to develop on sub-femtosecond time scales. In this regards, harmonic radiation offers a unique opportunity to push the temporal resolution of tr-PES and tr-ARPES beyond the few femtoseconds, thus entering in this little-explored domain. In 2007 Cavalieri *et al.* [44] extended the streaking technique to the condensed matter [209, 210] performing one of the first photoemission delay measurements. By ionizing a W(100) crystal with a single attosecond pulse, they found a relative delay of 100 as between the electrons emitted from the $4f$ state and the conduction band, whose physical origin has been highly debated [211, 212].

Indeed mechanisms and phenomena absent in the gas phase like above threshold photoemission by the IR field [213], space charge and secondary electron background, together with the relatively high IR intensities required for streaking ($\sim 10^{12}$ W/cm^2)

and the complexity of the multi-body physics at play, render the implementation and interpretation of streaking experiments in solids a formidable task. For example, compared to a streaking experiment performed in gas phase, with solid samples it is not clear whether the interaction with the IR streaking field happens already inside the solid (incomplete field screening) or only outside (complete field screening). Modelling

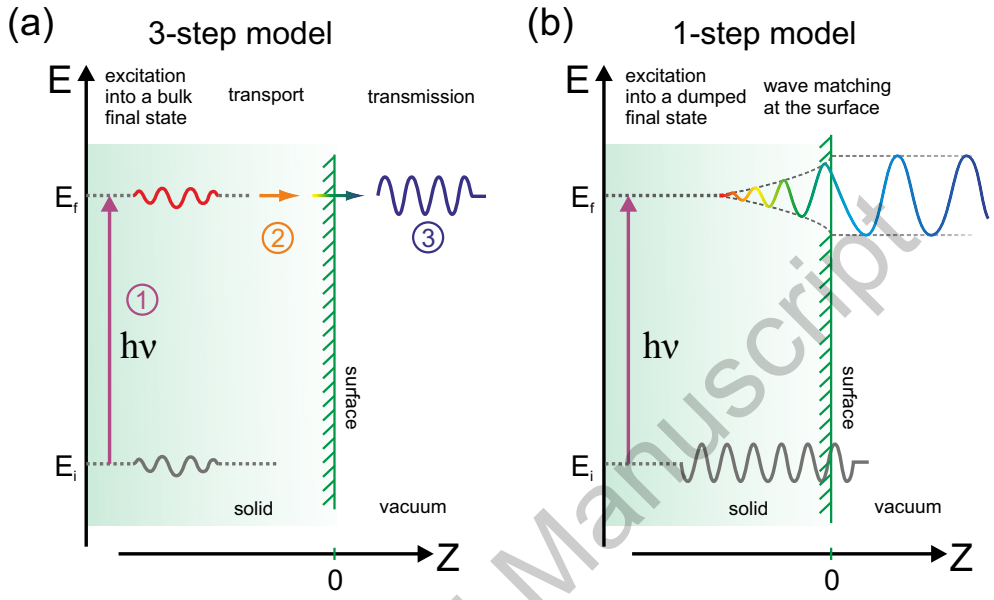

Figure 18. Schematic of the three-step model (a) or one-step model (b) used to describe the photoemission from solids. In (a) the electron is first photoexcited (1), then it travels to the surfaces (2) where it is transmitted into the vacuum (3). In the one step mode, instead, the Bloch electron is excited to a final state composed by a plane wave which decays while entering the solid (so called time inversed low-energy electron diffraction (LEED) state).

the XUV ionization in a solid is also not straightforward. While a more rigorous approach would require to describe the photoionization process in one step [214, 215], a phenomenological approach which has been proven to be useful is based on a three step model [181], where the photoionization can be interpreted as composed by (Fig. 18) a first excitation of the photoelectron (step 1), which then moves from the solid to the surface (step 2) and finally is transmitted through the surface into the vacuum (step 3). Whether or not one model is sufficient to explain the experimental results depends on the target and the level of accuracy required. Finally, the relatively strong IR field used to streak the photoelectrons not only limits the application of the technique to high photon energies (∼90 eV) to avoid the low-energy electron background [216], but also questions the validity of the static band-structure picture. A strong IR field can, in principle, modify the sample properties, deeply affecting the photoemission process and the physics behind.

For all the reasons mentioned above, important questions remained unsolved like: where does the streaking take place? Inside or outside the solid? How does the dynamical screening happens on an attosecond time scale? Is transport the main

mechanism dictating the photoemission timing in solids, or are there other processes to be considered, e.g. the effect of a different spatial localization of the initial state? In a ballistic transport picture, is the group velocity of the final state relevant or does the electron propagate as a free particle [217]?

This rendered the interpretation of the first results obtained in W not straightforward. Different theoretical approaches suggested that the observed delays may generate from two different mechanisms: *i*) different travel velocity of the escaping electrons (propagation) [218], or *ii*) caused by the interference of core-level photoelectrons that originate in different layers of the solid (initial wave-function localization) [204]. In order to find an answer, S. Neppl and coworkers repeated the streaking experiment on Mg(0001) [208], a free-electron metal where efficient screening of the IR field is expected at the first atomic layer, thus assuring that the interaction with the IR field happens only once the electron has left the solid. By measuring the relative photoemission delay between the $2p$ state and the valence band (VB), this material gives a unique opportunity to study the effect of the initial state. Indeed, as the free-electron like VB states are delocalized ($3s3p$-derived), while the $2p$ core states are localized, theoretical models predict that a substantial time delay ($\sim$100 as) should arise solely from differences in the initial state degree of localization. The authors found instead an almost simultaneous emission, which seems to suggest that the degree of initial localization has only minor influence. Their results are instead in agreement with a model where the photoemission delay can be explained by the differences in the inelastic mean free paths (IMFP), λ, and group velocities ,v:

$$\Delta\tau = \lambda_{VB}/v_{VB} - \lambda_{2p}/v_{2p}$$

To further investigate the role of the ultrafast dynamical screening at the interface and to disentangle the role of initial state localization from ballistic transport, the same authors repeated the experiment by adding a variable number of Mg layers on a W substrate [46] (Figs. 19(a),(b)). They found the delay between the W $4f$ and the Mg $2p$ states to increase with the number of Mg layers (Figs. 19(c)). As the final state is free-electron like for both transitions and since the IMFP is comparable for both classes of electrons, the authors interpreted the results with a ballistic model where the normal component of the streaking electric field is assumed to exponentially decay at the surface as:

$$E_{IR}(z,t) = E_0 e^{-z/\delta}$$

where the screening length δ along the propagation coordinate z is unknown. Since the experimental results can be reproduced only if $\delta \leq 3$ Å is assumed, the authors concluded that the screening of the streaking IR field must happen within one atomic layer in Mg.

Assuming perfect screening at the surface, one would expect the photoelectron wavepacket emerging from a solid to be longer than the initial excitation pulse because of the spread of the photoemission times. Following this idea, W.A. Okell and coworkers used the attosecond streaking technique to retrieve the temporal characteristics of

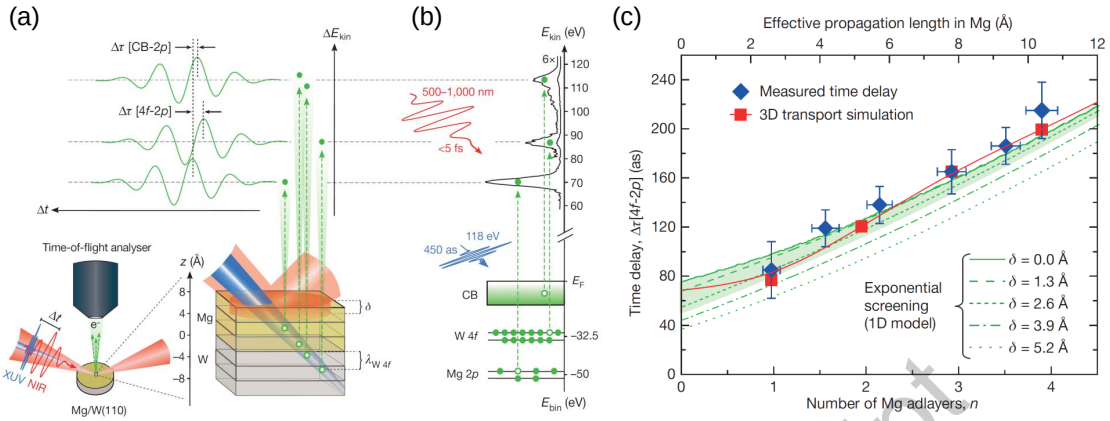

Figure 19. (a) Schematic of the experiment by Neppl *et al.* [46]. An XUV pulse ionizes a tungsten W(110) crystal capped with Mg atomic layers. The arrival time of the photoelectrons (green dots) at the surface is probed by the energy streaking caused by a sub-5 fs IR pulse. (b) Photoelectron transitions excited by the attosecond pulse (center energy of about 118 eV) together with a background subtracted photoelectron spectrum obtained with 4 Mg adlayers. (c) Measured time delays between the release of the W 4*f* and Mg 2*p* electrons as a function of the number of Mg adlayers (blue diamonds). The green lines show the theoretical prediction obtained with one-dimensional simulations which assume an exponentially decaying normal component of the IR field with variable screening length δ. The red squares represent the results of a full three-dimensional electron transport model. Adapted figure with permission from [46]. Copyright (2015), Nature Publishing Group.

the photoelectron burst emitted from WO_3 and Au [219]. Starting from an isolated attosecond pulse of about 248 ± 15 as, the authors found the outgoing photoelectron pulse to be 111 ± 60 as longer in WO_3 and 71 ± 60 as longer in Au. This quantities compare well with the time the photoelectrons need to travel one IMFP (about 90 as in WO_3 and 72 as in Au), further underlying the central role of transport in photoemission from solids.

Attosecond streaking spectroscopy has also been employed to get real-time access to electron scattering processes in dielectric nanoparticles [51, 220]. In these experiments, photoelectrons were generated inside the nanoparticles and both their transport through the material and photoemission were tracked on an attosecond timescale. The use of nanoparticles allowed to solve the problem of accumulative charging of dielectrics from the XUV-driven electron emission. It was demonstrated that the presence of an internal field inside the material cancels the influence of elastic scattering, enabling the selective characterization of the inelastic scattering time. The experimental technique, performed on a single-shot basis, was demonstrated on silica nanoparticles. The experimental approach enables the characterization of inelastic scattering in various dielectric solids and liquids, including water, which could be inserted in the experimental apparatus in

the form of droplets or as a thin jet. Moreover, a direct access to the measurement of the inelastic scattering processes in dielectrics for a wide range of energies including the otherwise inaccessible range below 50 eV holds promise for improving our understanding of radiation damage following tissue irradiation.

These first pioneering experiments demonstrated the potential of the streaking spectroscopy which has been later used to study a variety of physical phenomena initiated by light in solids, like the intrinsic and extrinsic excitation of plasmons in Mg [221], the role of intra-atomic electron-electron interaction in WSe_2 [50] and the role of surface resonances in Mg(0001) [222]. Nevertheless, its application remains a formidable task because of the associated technical and theoretical complexity. An alternative approach which is expected to relax part of the experimental difficulties while delivering comparable information [78, 223, 224], is based on the employment of the RABBITT technique instead of the attosecond streaking. Nevertheless, while the generation of an attosecond pulse train is generally less demanding, in a solid target the negative effect of the space charge and the background due to inelastic collision can be more severe when harmonic combs are used instead of single attosecond pulses. The artifacts and broadening introduced can widen the harmonics peaks, ultimately preventing a clear identification of the harmonic and sideband signals (Figs. 20(a),(b)) [225]. In addition, even if the IR peak intensity necessary to perform RABBITT is one to two order of magnitude lower than what requested for a streaking experiment, the low work function a solid target (few eVs) makes above-threshold ionization by the IR field more efficient, adding a dynamical background that can anyway prevent the investigation of electrons with low kinetic energy (Figs. 20(c)). All this renders the extension of the RABBITT technique to solid state not trivial and partially explains why it took almost 9 years from the first streaking experiment on W to successfully apply RABBITT to the condensed matter. The first example has been reported in 2015 by R. Locher and coworkers, who used an attosecond pulse train to study the photoemission from gold and silver [45]. Both in RABBITT and streaking the photoemission delays are derived from a phase measurement, thus being defined but an unknown constant, preventing the access to absolute photoemission delays. With energetic XUV photons (about 100 eV), this limitation is often overcome by studying relative photoemission delays obtained by looking at the difference between the timing of the photoelectrons emitted from two initial states of the same target. Unfortunately, in the energy range which corresponds to the minimum of the IMFP (about 5-10 Å at 50 eV [226]) and hence to the perfect condition to study electron excitation and transport in the first layers below the sample surface, this approach cannot be easily applied. One possibility is to deposit a reference gas target directly on the solid surface [227]. While conceptually smart, this method poses some technical challenges as the interaction between the atoms and the surface can, in principle, influence the photoemission process. In their work, Locher *et al.* introduced a different approach based on two spatially-separated focii [228]. They used XUV radiation centered around 30 eV to ionize electrons from the $5d$- and $4d$-valence bands of gold and silver (Fig. 21(a)) and obtained an external

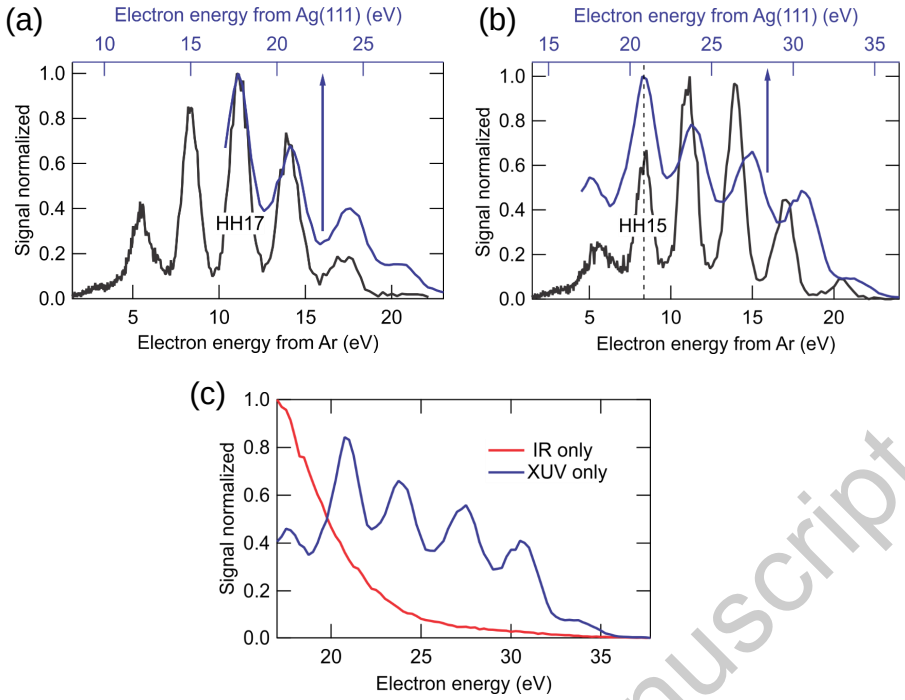

Figure 20. (a), (b) Photoelectrons emitted by an Ar atomic target, black, and an Ag(111) crystal (blue) excited by an attosecond pulse train. When the XUV photon flux is kept low, (a), the harmonic peaks from the atomic target and the solid coincides. If the photon flux is increased, (b), space-charge effects deform the Ag photoelectron spectrum, reducing the peak contrast and changing their relative spacing. (c) Comparison between the photoelectron signal from Ag, generated by the XUV, blue curve, and the IR radiation, red curve. Due to the relatively low work function of the Ag sample (about 4.7 eV), the IR electron yield is comparable to the XUV one even if the IR intensity is kept below 10^{11} W/cm^2. This effect is absent with atomic targets where the ionization potentials are typically bigger than 10 eV.

calibration by performing a simultaneous RABBITT trace on a reference gas target (Figs. 21(b), (c)). Knowing the physical properties of the chosen atomic target (e.g. Ar), it is possible to remove the unknown constant from the second RABBITT trace and access absolute delays. The energy dependent delays obtained with this approach are reported in Fig. 21(d) and show a non-trivial behavior, particularly evident for the case of silver. While at certain energies the photoemission delays agree with a ballistic model dominated by transport (Fig. 21(e)), in other energy regions the experimental data appear to deviate significantly, suggesting a prominent role of final state resonances which can significantly change the timing of the entire process [229]. The exact role of the final state in photoemission from noble metals like Ag and Au is not yet completely understood. More recent calculations based on a quantum-mechanical model, which includes the background contribution from secondary electrons, fail in reproducing the observe energy oscillations of Fig. 21(d). As the properties of the final state are not exhaustively included in the model, this result further suggests that final-state photoelectron-surface interactions may play a non-negligible role in the photoemission

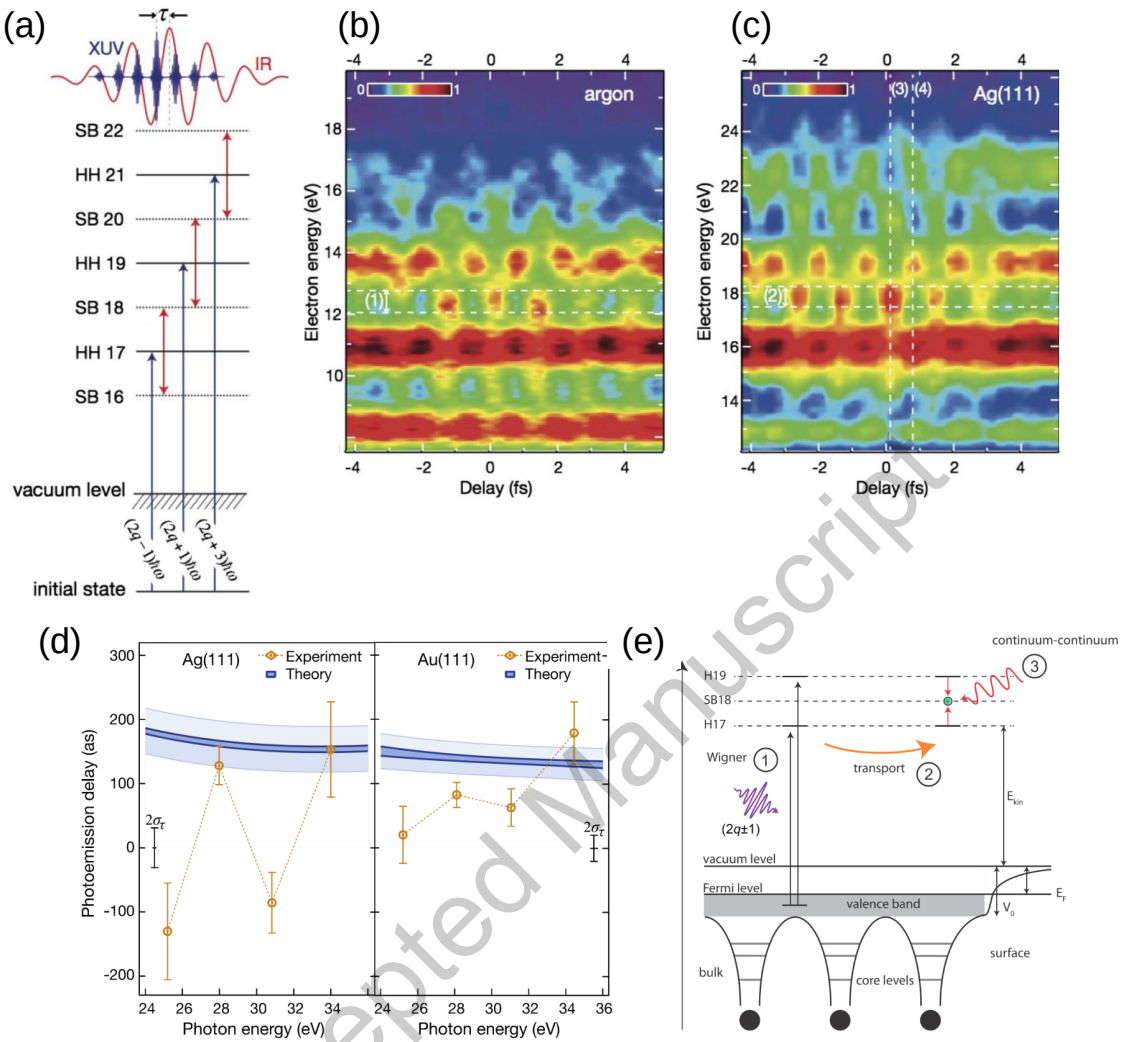

Figure 21. (a) Energy scheme of the RABBITT process where a valence-band electron is ionized by high-order harmonic photons (HH) at the presence of an IR field which generates the sideband (SB) signal. (b) Calibration RABBITT trace in Ar, (c) simultaneous trace in Ag(111). (d) Orange dots: photoemission delays for Ag (left panel) and Au (right panel) measured at the SBs position. In blue the theoretical prediction obtained with a ballistic model based on the three steps depicted in (e): first ionization by the XUV radiation, then transport to the surface and finally interaction with the IR field which generates the SBs. Adapted figure from [45].

process [230].

Soon after the first demonstration, it became clear that the RABBITT technique could be used to widen our knowledge of solid state physics. In 2016 Z. Tao *et al.* used RABBITT traces generated by different harmonic combs to investigate the photoemission process in Ni(111) over a broad energy range, from 20 to 50 eV [48]. Their results show an increase of the order of 200 as in the photoemission delays around 25 eV of photon energy, which has been interpreted as a clear the effect of the material band structure on photoemission time delays. In this case the authors explained their results

on the basis of a one-step model where the photoelectron lifetime can be understood as the time it takes to the associated wavefunction to evolve from a Bloch wave inside the solid to a free-electron wave outside. In a semiclassical picture this corresponds to the time the electron takes to travel an IMFP. Relating the time-domain measurements to the lifetimes and IMFPs of photoelectrons, the authors proposed that the increasing delay is the result of a bulk final state resonance happening when the final state corresponds to a short-lived excited state. Comparing the measured lifetimes with the IMFP obtained by assuming that the electrons propagate with their group velocity (i.e. by assuming that the electrons have acquired an effective mass) the authors further conclude that electrons behave more like plane waves, leaving the crystal before they can feel the influence of the lattice. Later, the same group observed a similar behaviour in the energy-resolved photoemission delays of Cu [231]. Compared to Ni, though, the RABBITT delays in Cu are about 100 as longer. The difference between the two materials has been attributed to the enhanced electron–electron scattering in the unfilled d band of Ni, showing that if the effect of screening is negligible, RABBITT can be used to directly address electron-electron scattering dynamics in solids.

Whether or not the escaping electrons propagate with free velocity ultimately questions the validity of the effective mass concept on atomic length and time scales [232]. By applying the RABBITT technique to investigate the photoionization of a Cu(111) crystal, L. Kasmi *et al.* [49] found that while most of the retrieved delays follow a monotonic behavior, decreasing with an increasing electron kinetic energy, at precise energies which correspond to bulk resonances, the photoemission delay increases (Fig. 22). This phenomenon could be explained by assuming that the excited electron propagates towards the surface with its group velocity, dictated by the final state band curvature, i.e. its effective mass. As the whole process takes places in less that 400 as, this establishes an upper limit to the time that an electron requires to assume the effective mass of its excited state and suggests that in case of a final-state resonance, the Bloch wavepacket forms within two atomic layers. Recent theoretical calculations performed with a quantum-mechanical model, which takes into account for the interaction between the excited photoelectron and the substrate, interpret the increased photoemission delay observed in Cu(111) at about 25 eV as due to an increase in electron propagation time [233]. At resonance, an effective shift of the final-state probability density away from the exit surface into the bulk is observed, thus inducing an effective increase of the photoelectron-escape depth and, in turn, of the associated photoemission delay. More recently S. Heinrich *et al.* revisited the photoemission process in W(110), studying its timing on a broad excitation energy range with the RABBITT technique [234]. Their results also show a clear effect of the final state which causes an increasing delay in valence band and core $4f$ states, plus an intra-band delay in the valence band due to different orbital contribution (sp vs d). In agreement with what reported by Kasmi *et al.* [49], the photoemission delays in W are better explained by assuming that the electrons propagate with a velocity based on the final band dispersion rather than considering free-electron propagation and not by a changing emission depth as done to explain the

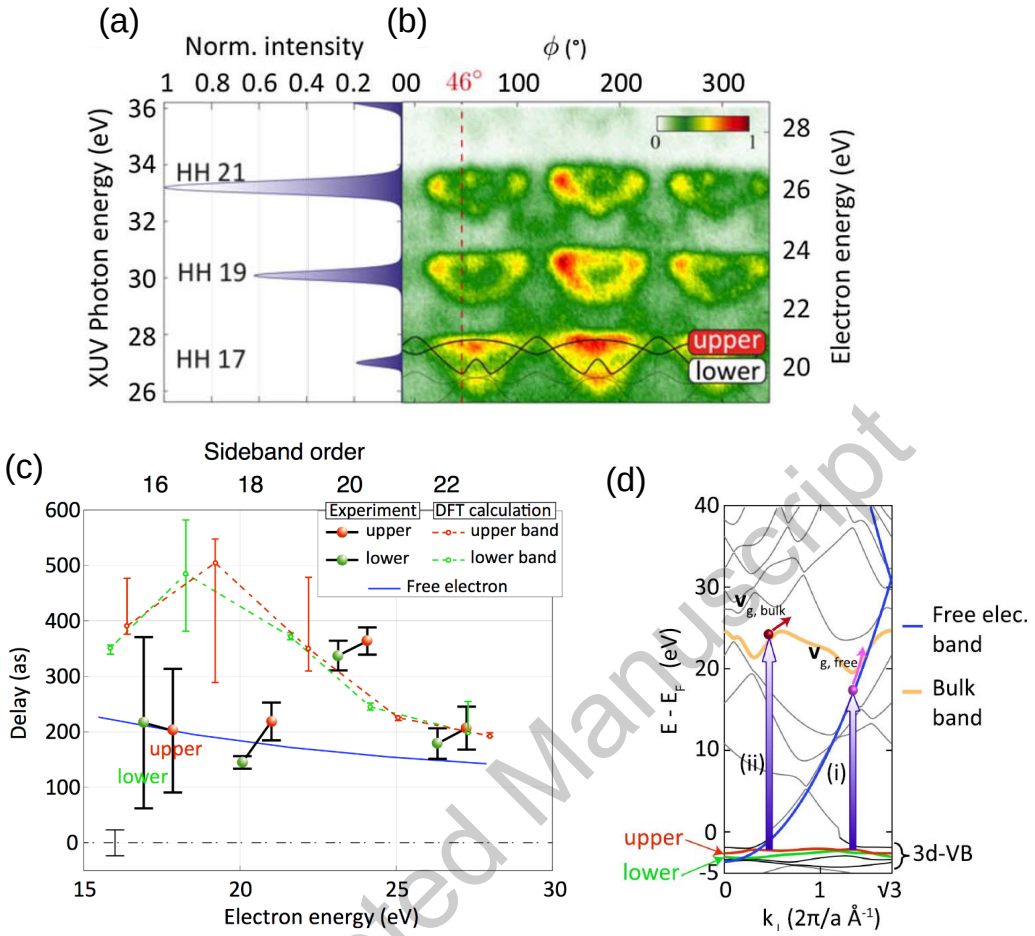

Figure 22. (a) Harmonic spectrum used to perform the RABBITT experiment in [49]. (b) Photoelectron spectra from the Cu 3*d* valence band, obtained by rotating the sample around the (111) direction. A clear split of the 3*d* VB in upper and lower sub-bands is visible. (c) Experimental photoemission delays (black) for the upper and lower part of the Cu 3*d* valence band against the theoretical prediction which assumes a free-electron like final state (blue curve - mechanism (i) in (d)) or an electron which propagates with a group velocity determined by the final state band structure (green and red curves - mechanism (ii) in (d)). (d) Schematic displaying the two types of excitation: through a parabolic free-electron final state (i) or through a resonant dispersive bulk state (ii). Adapted figure from [49].

Ni results [48], hence suggesting that the effective mass concept is still valid. The sensitivity of the attosecond photoemission delays obtained with RABBIT to the solid band dispersion and the effective mass have also been recently theoretically investigated by Q. Liao *et al.* [235], who showed that the energy dependence of the effective mass can induce an appreciable change even for small deviations from the free-electron behaviour, inducing negative photoemission delays like the one observed in Ag [45].

All the experiments described above clearly show that understanding and interpreting attosecond photoemission experiments from a solid target can be an hard

task. Not only because of the complex, multi-electrons effects present in condense matter physics and absent in atomic gas targets, but also because of the presence of a solid-vacuum interface: the surface. Compared to the experiments performed in gas, the surface of a solid breaks the symmetry and introduces possible reflection/refraction of the pump IR beam and of the outgoing electrons. While increasing the experimental complexity, this increases the level of information encoded in the measured RABBITT or streaking phases. For example, the RABBITT phases extracted are modelled as composed by two main contributions: one associated to the XUV photon absorption and one with the interaction with the IR field (so called continuum-continuum delay [88]). In a gas atomic target, the latter contribution does not carry direct information about the short-range atomic potential and it is often discharged as it can be modeled with an universal curve for Coulombic potentials [74]. An IR field impinging on a solid instead, is partially transmitted and reflected according to the sample physical properties. The 2D transient grating formed on the surface is thus sensitive to the electron-scattering rate, and the study of its properties can give access to collective electron dynamics at the surface like plasmon excitation/decay or the dynamical screening process [236]. M. Lucchini *et al.* performed attosecond delay measurements on Cu(111) at two different light incidence angles from the surface normal: 15° and 75° [47]. They found that the photoemission delays can vary by more than 300 as solely due to the temporal properties of the different IR transient grating which forms at the surface. Comparing their results with Monte Carlo simulations based on a semi-classical model where the surface has infinitesimal thickness [237], they could show that macroscopic Fresnel equations are still valid on an atomic length and on an attosecond time scale despite the unrealistic field discontinuity at the interface. In turn, this proves that efficient and fast electron screening renders negligible the effect of the transmitted wave, thus further confirming that the interaction with the IR field happens outside the solid for noble metals. Despite the simplicity of the Monte Carlo model, the calculations reproduce well the experimental data apart from a constant temporal offset. The calculated absolute delays are approximately 50 as smaller. This discrepancy may arise from the too crude description of the solid surface (assumed to be an infinitesimally thin plane) or from an erroneous estimation of the IMFP [238, 239]. To further investigate this aspect M. J. Ambrosio and U. Thumm tried to reproduce the experimental results of Fig. 23(e) with a quantum-mechanical model which includes a more realistic description of the surface [240]. In this case the discontinuity of the normal component of the IR electric field at the solid-vacuum interface is removed by introducing a gradual transition function which damps exponentially the total IR field inside the solid. While their results qualitatively agree with the experimental data, thus confirming that the RABBITT phases are strongly affected by the phase of the reflected IR pulse [241], they also underestimate the photoemission delays by almost 50 as, being in agreement with the Monte Carlo simulations. This offset may indicate an anisotropy of the dielectric constant in Cu(111), not accounted for in the calculations, or an incomplete description of the initial state. Further investigation is needed to find an answer and widen our

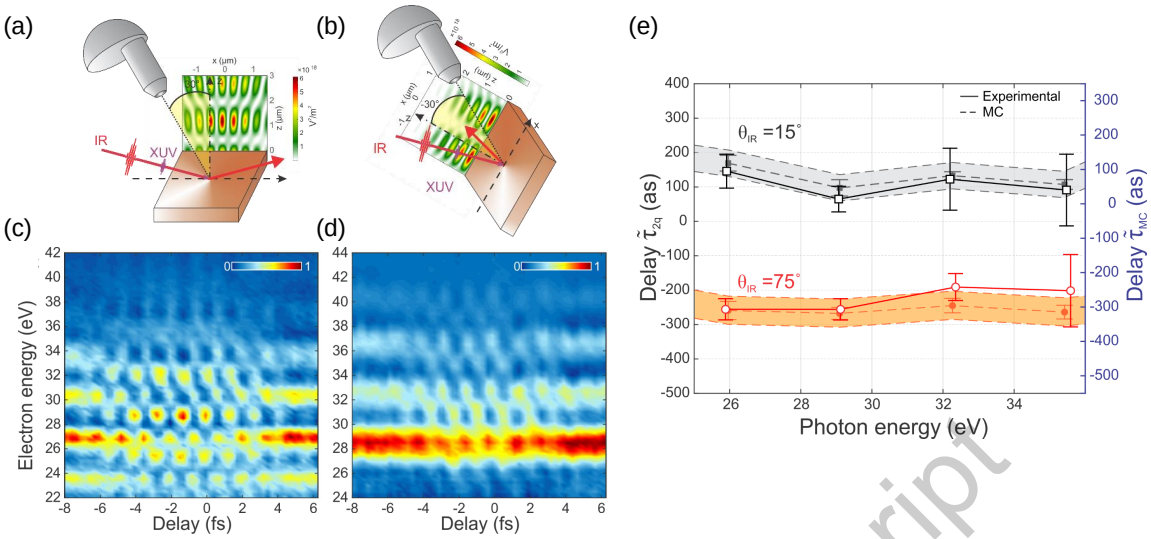

Figure 23. (a), (b) Photoelectron detection geometry and IR field distribution at the Cu(111) surface (false colors) for the two incidence angles used in Ref. [47]. (c), (d) associated background-subtracted RABBITT traces. (e) Energy dependent photoemission delays extracted from the experimental traces (open markers) or calculated with a semiclassical ballistic model based on macroscopic Fresnel equations (dashed lines and shaded areas). Adapted figure with permission from [47], Copyright (2015) by the American Physical Society.

description of laser-assisted photoemission from metals. It is important to stress that a complete brute-force solution of a multi-body system represents a formidable task. Therefore, multi-electron effects are usually included in an approximated way by using effective potentials or time dephasing parameters. How to describe non-equilibrium electron dynamics in solids including many-body effects is indeed a current open issue in theoretical solid-state physics [242], where advanced approaches based on the many-body perturbation theory suggest a promising route towards the solution of the problem [243].

In conclusion, whether it is based on isolated pulses or pulse trains, attosecond PES and ARPES of solids has proven to be a powerful investigation tool which can at once widen our knowledge of the complex multi-electron physics happening on ultrashort time scales and provide a unique benchmark for the future development of the physical models we currently use to describe light-matter interaction.

3. Attosecond transient absorption and reflection spectroscopy

A powerful, all optical technique for ultrafast spectroscopy is attosecond transient absorption spectroscopy (ATAS) [12, 95, 244–247]. The typical scheme of ATAS employs a few-femtosecond visible or near-infrared (NIR) pulse to excite the sample and an attosecond pulse, in the form of an isolated pulse or a train of pulses, to probe the dynamics induced by the excitation pulse. Typical photon energies of the attosecond

pulses determine excitation of an electron from an inner shell to the valence shell. In ATAS, the femtosecond pulse determines variations in the absorption cross-section of the sample, which are experienced by the attosecond pulse. The spectrum of the attosecond pulse transmitted by the sample is then measured by using an XUV spectrometer, as a function of the pump-probe delay. The XUV spectrum is measured at each time step, with (I_{on}) and without (I_{off}) the pump pulse, and the measured quantity is the change in optical density, $OD = -\log_{10}(I_{on}/I_{off})$ (equivalently, changes in the optical depth $Abs = -\ln(I_{on}/I_{off}) = \alpha L$, with α being the absorption coefficient and L the medium thickness). This technique is characterized by high temporal and spectral resolution. This is typically accompanied by higher data collection efficiency, compared to photo-electron or photo-ion spectroscopic techniques. Moreover, the broad and continuous spectrum of isolated attosecond pulses offers the possibility to probe simultaneously multiple absorption features vs the pump-probe delay.

In a second ATAS scheme the attosecond pulse excites the sample and a femtosecond pulse follows the XUV pulse at various and controlled time delays. In this configuration the attosecond pulse creates a polarization, triggered by the generated coherent superposition of states, which remains in the medium after the transit of the XUV pulse. The polarization results from the collective action of a large number of individual atomic/molecular oscillating dipoles and persists in the medium on a time scale determined by the dephasing time of the oscillating dipoles. Then, the femtosecond pulse perturbs this polarization by introducing couplings between different states or between discrete and continuum states. Since the oscillating dipoles emit radiation, the spectrum of the XUV light transmitted by the sample changes as a function of the delay between the broadband attosecond pulse and the femtosecond pulse. This ATAS configuration has been employed in the case of gases, since in this case the dephasing time of the oscillating dipoles generated by the XUV excitation can be of the order of a few femtoseconds, or even a few nanoseconds for an atomic Rydberg state. On the contrary, in the case of solids, dephasing time can be of the order of a few tens of attoseconds. For example, in the case of silicon, the dephasing time of the polarization induced by an XUV pulse was estimated to be ~ 100 as [248].

From a general viewpoint, the transient absorption spectrum can be calculated starting from the calculation of the single atom response function, $\tilde{S}(\omega)$, from the time-dependent energy exchange between the atom and the light field as [249–251]:

$$\tilde{S}(\omega) = 2\,\mathrm{Im}[\tilde{d}(\omega)\tilde{E}^{*}(\omega)] \tag{11}$$

where $\tilde{d}(\omega)$ is the Fourier transform of the dipole moment, $d(t)$, and $\tilde{E}(\omega)$ is the Fourier transform of the full electric field, $E(t)$, consisting of the sum of the dressing femtosecond IR laser and the XUV fields. The dipole moment can be calculated by solving the time-dependent Schrödinger equation (TDSE) using the full electric field $E(t)$ in the single-active-electron (SAE) approximation. With this definition, the integral of $\tilde{S}(\omega)$ over all frequencies yields the total excitation probability. For positive frequencies, $\omega\tilde{S}(\omega)$ is the energy gained or lost per unit frequency by the atom. In the weak-IR limit, the

absorption cross-section $\tilde{\sigma}(\omega)$ can be written as [249]

$$\tilde{\sigma}(\omega) = 4\pi\alpha \frac{\omega \tilde{S}(\omega)}{|\tilde{E}(\omega)|^2} \tag{12}$$

where α is the fine-structure constant. By using the definition of $\tilde{S}(\omega)$ given by Eq. (11), the cross section can be written as:

$$\tilde{\sigma}(\omega) = 8\pi\alpha\omega \,\mathrm{Im}\left[\frac{\tilde{d}(\omega)}{\tilde{E}(\omega)}\right] \tag{13}$$

Then, in order to calculate the transient absorption, the Maxwell wave equation for the time propagation of the light fields through the atomic medium must be solved, using polarization and ionization source terms. The polarization is given by $\rho\tilde{d}(\omega)$ where ρ is the atomic density and the ionization source term is related to the space- and time-dependent free-electron contribution to the refractive index [252]. An interesting result is that macroscopic absorption spectra calculated by considering the propagation of XUV and IR pulses are similar to the single-atom results, scaled by the density, so that the experimental results can be analysed by calculating the single-atom response.

From its first implementation, ATAS has been recognized as a very powerful experimental approach to understand and control the ultrafast dynamics of electrons in matter. At a very fundamental level, electron dynamics can be studied in atoms and the first applications of ATAS were reported in atomic physics.

3.1. ATAS in atomic physics

The first demonstrations of ATAS were reported in 2010, with the investigation of ultrafast electron dynamics in krypton [56] and argon [57], soon followed by application to helium atoms [253]. In the case of krypton, sub-4-fs, 750-nm pump pulses were used to ionize Kr atoms from the $4p$ subshell. In this way a krypton ion was produced in a superposition of its two lowest energy states, the spin-obit split $4p^{-1}_{1/2}$ and $4p^{-1}_{3/2}$, separated by an energy difference $\Delta\mathcal{E} = 0.67$ eV. The temporal evolution of the generated wave packet is characterized by an oscillation period $T = h/\Delta\mathcal{E} = 6.3$ fs (where h is the Planck's constant). Snapshots of the time-dependent hole wave packet were acquired using sub-150-as probe pulses, centred at 80 eV, used to excite another electron from the deeper-lying $3d$ shell of Kr^+ into the hole: this was obtained by measuring the spectrum of the transmitted XUV light as a function of the pump-probe delay. A modulation of the XUV absorption spectrum as a function of the pump-probe delay was measured, with a period of 6.3 ± 0.1 fs, directly related to the quantum mechanical motion of the electron wave packet generated by the $4p^{-1}$ sub-shell coherent superposition [56]. The possibility to observe this quantum motion was related to the degree of coherence of the generated hole wave packet, crucially linked to the duration of the NIR pump pulse. The measurement of both the amplitude and phase of the oscillations allowed the

reconstruction of the temporal evolution of ensemble-averaged hole density distributions in the $4p$ subshell of Kr^+.

In the case of argon, ATAS was first employed for the investigation of the autoionization process, which is intrinsically governed by electron-electron correlation [57]. Autoionization was initiated by isolated attosecond pulses and monitored by measuring, with a spectrometer, the time integral of the interference between the XUV fields transmitted and radiated by the induced dipole. This interference results in a Fano-like profile which can be modified if a delayed few-cycle pulse centred at 750 nm is used to couple the autoionizating state to the neighboring bound states or to the continuum states. By measuring the evolution of the Fano profile as a function of the the pump-probe delay it was hence possible to obtain a signature of the autoionization process itself. We recall that Fano resonances are characteristic resonant features with an asymmetric shape, clearly different from the common Lorentzian lineshape, first studied by Ugo Fano [254, 255]. The asymmetric shape originates from the interference between two indistinguishable pathways leading to the same final state into the continuum: direct ionization or excitation and subsequent decay from the metastable configuration state. In the case of argon discussed by Wang *et al.* [57], the Fano resonance was produced by the interference between the continuum of singly ionized argon and discrete states $3s3p^6np$, coupled to the continuum by autoionization.

The same technique was applied to measure the lifetimes of the autoionizing $5s5p^66p$ and $5s5p^67p$ channels of xenon [256], to observe interference processes in electronic Rydberg wave packets [257–259] and to observe sub-cycle changes in the absorption spectrum of neon, excited by isolated attosecond pulses, resulting from both sub-cycle ac Stark shifts and from quantum interferences between different multiphoton excitation pathways [260].

In the case of helium, Holler and coworkers performed the first ATAS experiment based on an attosecond pulse train rather than a single attosecond pulse [253]. In particular, the authors used a comb of harmonics centered around the first ionization potential of He ($\sim$ 24.59 eV) to either populate the np states many-fold or directly ionized the atom. A few-femtosecond IR pulse was then used to control the ionization probability on attosecond time scale. They observed fast modulation of the harmonics absorption which was found to oscillate with twice the IR frequency. In line with what reported by Johnsson *et al.* [104], Holler and coworkers suggested that these ultrafast oscillations mainly originated from the interference of transiently bound electron wave packets created by subsequent pulses of the attosecond train (Fig. 24(a)). This interpretation was later refuted by Lucchini *et al.* [261] who repeated the experiment bu varying length the number of pulses in the XUV train, down to the single pulse. Their results show that the oscillation amplitude does not scale as a function of number of XUV pulses as expected by the proposed interference mechanism. 2ω-oscillations of comparable strength were observed also with a single attosecond pulse (Fig. 25) as previously reported by Chini *et al.* [262], and rather originates from phenomena like: resonant absorption lines of the $1snp$ atomic states affected by sub-

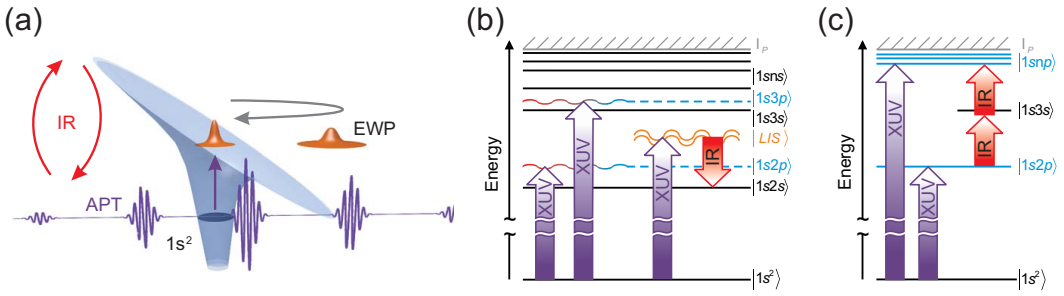

Figure 24. Schematic of the main mechanisms proposed to explain the oscillation of the photoabsorption probability in helium. (a) Interference between two parts of a transiently bound electron wave packet excited by subsequent pulses. (b) Resonant absorption lines of the $1snp$ series affected by sub-cycle ac Stark shift and light-induced states (wavy lines). (c) 'Which-way' interference between direct XUV excitation and an IR-assisted two-color transition. Reprinted figure with permission from [261], Copyright (2013) by IOP Publishing.

cycle ac Stark shift [263], light-induced structures associated with two-photon/two-color processes (XUV±IR) which populate a non-dipole coupled s or d state [250] (Fig. 24(b)) and "which-way" interference [101] between the direct population of the $1snp$ states near threshold (n> 5) and indirect population via a three-photon/two-color process (XUV+2IR) involving the $1s2p$ state (Fig. 24(c)). As two consecutive harmonics are separated by two IR photons, in the case of attosecond pulse trains 2ω-oscillations can also originate from an interference process where the IR field couples one harmonic with the subsequent by means of additional two-photon absorption or emission. Increasing the IR intensity it is possible to couple two non-consecutive harmonics via interaction with four IR photons, inducing 4ω-oscillations onto the harmonic absorption [264]. As Herrmann and coworkers showed, these high frequency oscillations can be used to obtain a fine calibration of the delay axis for pump-probe measurements where He is used as a buffer gas[264, 265]. Moreover, ATAS in He gives the opportunity to study other important phenomena like Autler-Townes splitting, quantum beating, virtual transitions [266, 267], the possibility to control light-induced states with the laser polarization [268] or to investigate the effect of propagation into a dense medium [93, 269].

A far reaching application of ATAS was reported by Ott *et al.* [270], with the demonstration of the possibility to control the electron motion within an atom, by using a few-cycle NIR pulse. A crucial problem, which can be addressed by ATAS, together with suitable theoretical models, is understanding the very first effects of a laser field on matter. A moderately intense ($10^{11} - 10^{13}$ W/cm^2) laser field can control the absorption of light on the attosecond time scale. In 2013 Ott used a train of attosecond pulses to excite helium atoms and the spectrum of the transmitted XUV light was measured by a high-resolution spectrometer in the vicinity of the sp_{2n+} doubly excited state resonance series [270]. A 7-fs NIR laser pulse of controlled intensity was focused on the sample at a fixed delay of ~ 5 fs after the XUV pulse. At a NIR intensity of about 2 TW/cm^2 the asymmetric Fano profiles of the doubly excited states of helium around ~ 64.6 eV were

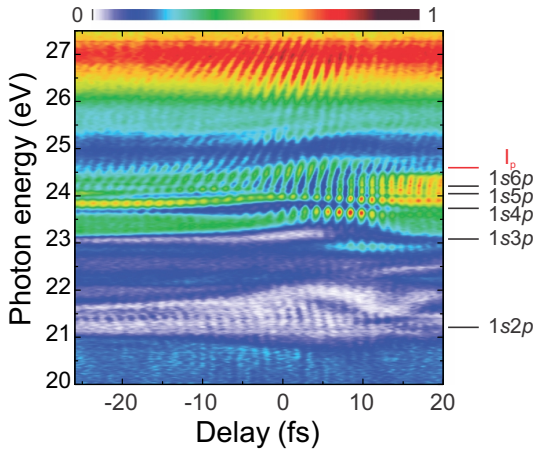

Figure 25. Transient He transmission measured with an isolated attosecond XUV pulse. The black lines mark the energy position of single-photon accessible atomic states of helium. Fast modulation of the transmitted signal and distortion of the atomic lines are evident around the region of zero pump-probe delay. Adapted from [261], Copyright (2013) by IOP Publishing.

modified into symmetric Lorentzian profiles, while the symmetric profiles of the singly excited states around ~ 24.3 eV, were turned into asymmetric ones. The variation of the lineshape symmetry was explained in terms of an additional phase acquired by the Fano resonances in the presence of the NIR pulse, thus demonstrating that the optical properties of a medium can be modified at will by controlling the quantum states of inner-shell electrons with light pulses.

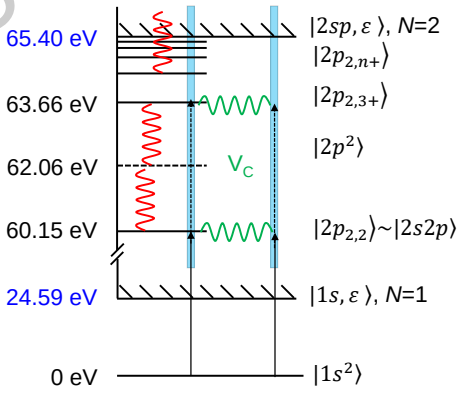

Figure 26. Schematic level diagram of helium, with the relevant transitions induced by the XUV and IR pulses. The $|sp_{2,n^+}\rangle$ states couple, as indicated by the green wavy lines, to the $|1s, \epsilon p\rangle$ continuum by configuration interaction V_C. The NIR laser field (red wavy lines) creates an additional time- and intensity-dependent coupling.

A natural extension of this work was the reconstruction of a correlated time-dependent, two-electron wave packet from a 1.2-fs quantum beat among low-lying doubly

excited states in helium [271]. This experiment represents a very nice demonstration of the precise control of correlated electronic motion in atoms, which can be achieved by few-cycle NIR pulses in combination with ATAS. The idea is to use the Fano resonance as a phase-sensitive quantum interferometer. Figure 26 shows a schematic diagram of the energy level of helium, with the relevant transitions induced by the XUV and IR pulses. Without the NIR pulse, Fano resonances are produced by the coupling, by configuration interaction, V_C, between the $|1s, \epsilon p\rangle$ continuum (one electron is in the $|1s\rangle$ ground state of helium and the second electron is in the continuum with kinetic energy ϵ) and the $|sp_{2,n+}\rangle$ doubly excited states (i.e., the Coulomb interaction among the two electrons of the doubly-excited states leads to autoionization, thus coupling the discrete state and the $1s$ continuum). The few-cycle NIR pulse introduces a coupling between the $|2s2p\rangle$ and $|sp_{2,3+}\rangle$ states, populated by the XUV pulse, whose energy difference is equal to two NIR photons (two-photon dipole coupling), thus introducing an additional relative phase, $\phi(t)$, between the two states which form a coherent wave packet

$$|\psi(t)\rangle \propto \exp\left(-\frac{\Gamma_{2s2p}}{2}t\right)|2s2p\rangle + a\exp\left(-\frac{\Gamma_{sp_{2,3+}}}{2}t\right)e^{-i\phi(t)}|sp_{2,3+}\rangle \tag{14}$$

where Γ represents the natural decay widths of the states. The difference in the phase evolution between the two states manifests itself as a periodic modulation of the transmitted XUV spectrum, which, in combination with a theoretical model, allows one to retrieve the relative phase of the two-electron wave packet and to reconstruct the correlated electron dynamics.

The time-dependent formation of the $|2s2p\rangle$ Fano absorption line has been measured by ATAS (and, independently, by attosecond photoemission spectroscopy [91]) by using the few-cycle NIR pulse to interrupt the autoionization process of doubly-excited states of helium, produced by attosecond XUV pulses [90]. The NIR pulse ionizes the excited atoms thus depleting the autoionizing level and ending the buildup process of the spectral line. It is worth to point out that the potential applications of this experimental approach are not limited to helium, but could be extended to molecules as a way to control the electronic motion within single molecules.

3.2. ATAS in molecular physics

3.2.1. Wave packet dynamics in diatomic molecules The extension of ATAS to molecular systems was reported in 2016 by various groups in the case of homonuclear diatomic molecules: hydrogen [272] and nitrogen [273, 274]. In the case of molecular hydrogen, a molecular wave packet in an excited state of H_2 was created by an attosecond pulse with a spectrum extending from ~ 12 to ~ 17 eV, thus overlapping the excited-state manifold of neutral H_2, obtained by using an indium foil filter after the gas cell for HHG [272]. The broadband attosecond pulse excites the molecule from the $X\ ^1\Sigma_g^+$ ground state to a coherent superposition of excited vibrational wave packets in both the $B\ ^1\Sigma_u^+$ and $B'\ ^1\Sigma_u^+$ states (see Fig. 27). The two WPs evolve independently, since they experience different potential energy surfaces. At variable and controlled time

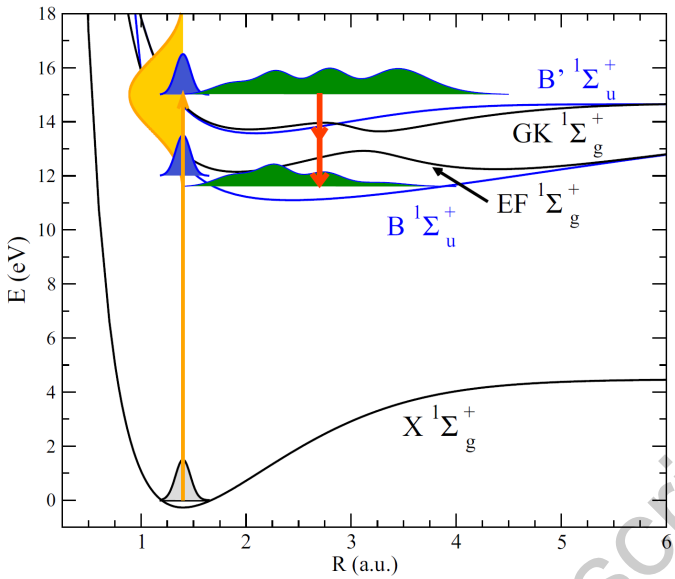

Figure 27. Potential energy curves for the $X\ ^1\Sigma_g^+$ ground electronic state and the first two singly excited $B\ ^1\Sigma_u^+$ and $B'\ ^1\Sigma_u^+$ (blue curves) states of H_2. The molecule, initially in its ground state (gray shaded area), is excited by an attosecond pulse (orange arrow), with a broad spectrum (orange shaded area). The two WPs (blue shaded area at time $\tau = 0$), evolve independently (green shaded areas). After a time delay τ, the NIR pulse determines an exchange of population between the two potential energy surfaces, B and B', by a two-photon transition (red arrows), assisted by the EF and $GK\ ^1\Sigma_g^+$ states. Reprinted figure with permission from [272], Copyright (2016) by the American Physical Society.

delay, τ, a NIR pulse determines an exchange of population between the two potential energy surfaces, B and B', by a two-photon transition, assisted by the $EF\ ^1\Sigma_g^+$ and $GK\ ^1\Sigma_g^+$ states. If the NIR pulse duration is much shorten than the time scale of the evolution of the two WPs, the WP promoted to the B surface is a replica of the WP on the B' surface at time τ multiplied by a two-photon dipole transition amplitude with a smooth radial dependence. This process creates $\sim$ 1-fs beatings in the transient absorption spectrum in the region between 11 and 12 eV, corresponding to the spectral position of the first four vibrational peaks in the $B\ ^1\Sigma_u^+$ band, as shown in Fig. 28. These beatings are produced by the interference between the direct excitation from the ground state, induced by the attosecond pulses, and the stimulated emission of two NIR photons from the $B'\ ^1\Sigma_u^+$ state, populated by the attosecond pulses, whose contributions add up coherently. Therefore, the molecular WP produced in the B' band is holographically imprinted on the vibrational states of the B band, so that the instantaneous beating amplitude and phase of the B absorption feature contain all the information required for the reconstruction of the B' vibronic WP generated by the VUV pulse. The procedure is the following: the beating absorption of the B states are fitted by $f_v(\tau) = B_v(\tau) + A_v(\tau)\cos[\omega\tau + \phi_v(\tau)]$, as shown by the dashed lines in Fig. 28, where

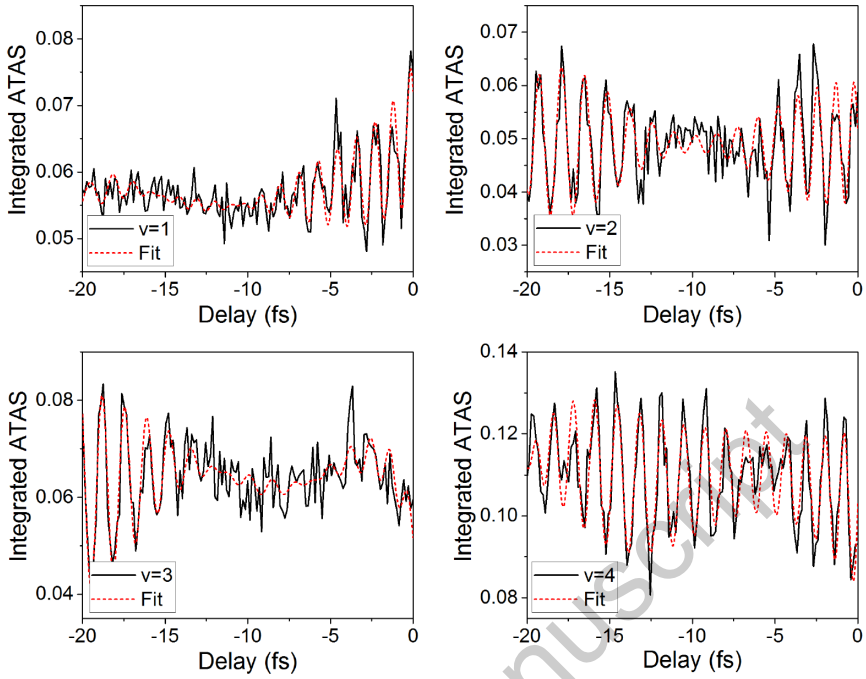

Figure 28. Measured transient absorption variation (black curves) of the first four vibrational peaks in the $B\ ^1\Sigma_u^+$ band. The red dashed curves are the fits to the experimental data. Reprinted figure with permission from [272], Copyright (2016) by the American Physical Society.

$B_v(\tau)$ is a smooth background, $A_v(\tau)$ and $\phi_v(\tau)$ are independent fitting parameters. The reconstructed WP in the B' state is given by $|\nu_{B'}\rangle = \sum_v |\nu_B\rangle A_v(t)\exp(-i\phi_v(t))$. This result demonstrated the capability of ATAS to capture electronic and nuclear dynamics in molecular structures with extreme spectral and temporal resolution at the same time.

The evolution of WPs generated in molecular nitrogen was investigated by various groups [273–275]. Tunable broadband XUV continua were used by Reduzzi *et al.* to generate two different WPs [273]. By using low-energy excitation (LEE) pulses around 15 eV (generated in Xe and filtered by indium foils, with a duration of $\sim$ 1.4 fs) the bound excited states of N_2 were mainly populated, while by using high-energy excitation (HEE) pulses around 18 eV (generated in Xe and filtered by tin foils, with a duration of $\sim$ 930 as) two series of Fano resonances were excited. In both cases, the tails of the XUV continua, towards the high energies for the LEE pulses and towards the low energies for the HEE pulses, were able to generate an electronic WP with components below and above the ionization threshold. Since the bound excited states, below and around the ionization threshold, and the Fano resonances are spaced by $\sim$ 3.1 eV, the NIR pulse, with photon energy of 1.55 eV, produced a two-photon coupling between the bound states and the Fano resonances, with a corresponding modulation of the absorption cross section. Oscillations, with a period of $\sim$ 1.3 fs, were measured in the region of Fano resonances (around 18 eV) in the case of LEE and on the bound excited

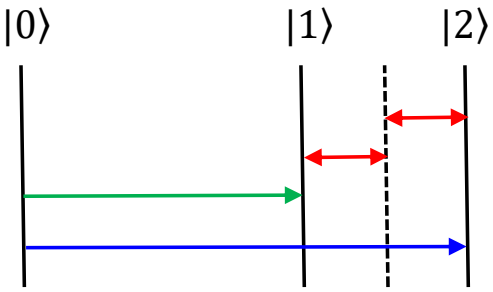

Figure 29. Three level model used in [273]. The blue and green arrows indicate the XUV excitation; the two-NIR-photon coupling between the excited states $|1\rangle$ and $|2\rangle$ is indicated by the red double arrows.

states (around 15 eV) in the case of HEE, originated by the two-photon NIR coupling. The process can be understood in the framework of a simple three-level model, as shown in Fig. 29, where the bound excited states correspond to the state $|1\rangle$ and the Fano resonances to the state $|2\rangle$. The simulations obtained using this model confirmed that in the case of LEE, the amplitude of the Fano resonances, only weakly excited by the XUV pulses, are the result of the interference between the weak direct XUV excitation and a second excitation path involving the XUV excitation of the bound states and two-photon NIR excitation. A similar interference effect explains the modulation of the bound states in the HEE case. Therefore, ATAS, in combination with tunable XUV radiation, allows one to achieve a direct control, with attosecond temporal resolution, of the population of Fano resonances and of the bound excited states. An additional result was the measurement of the dynamics of autoionizing states, from the evolution of the depletion in the autoionizing region. The measured lifetimes were $\tau = 10.2$ fs for the $3d\sigma_g\ ^1\Sigma_u^+$ and $\tau = 13.8$ fs for the $3d\pi_g\ ^1\Pi_u$ resonances.

The ultrafast coherent dynamics of a molecular WP composed by valence and Rydberg states of nitrogen were investigated by Warrick *et al.* [274, 275], using 6-fs NIR pulses and broadband attosecond pulses generated in xenon and transmitted by an indium foil to select the low-energy portion of the spectrum, between 11 and 17 eV. The transient absorption measurement as a function of the XUV-NIR time delay shows two main characteristics: an energy shift of the excited states in the presence of the strong NIR field, related to ac Stark effect, and oscillations of a few absorption features with different periods. Sub-cycle quantum beating with a period of 1.3 fs was measured at 15.8 eV, due to NIR-induced population transfer between energy levels separated by $\sim$ 3 eV, related to two-NIR-photon transitions mediated by a resonant XUV-dipole-forbidden state. Oscillations with period in the range between 5 and 10 fs, at 14.5 eV and 16.5 eV, were determined by NIR-induced coupling of individual states in the molecular WP to multiple neighbouring states. Oscillations of the bound states of N_2 with a period of 50 fs were investigated in more detailed in Ref. [275]. These oscillations were associated to nuclear dynamics in the $b'\ ^1\Sigma_u^+$ valence state, visible in the transient absorption spectra due to NIR-induced coupling of adjacent vibrational levels in the b'

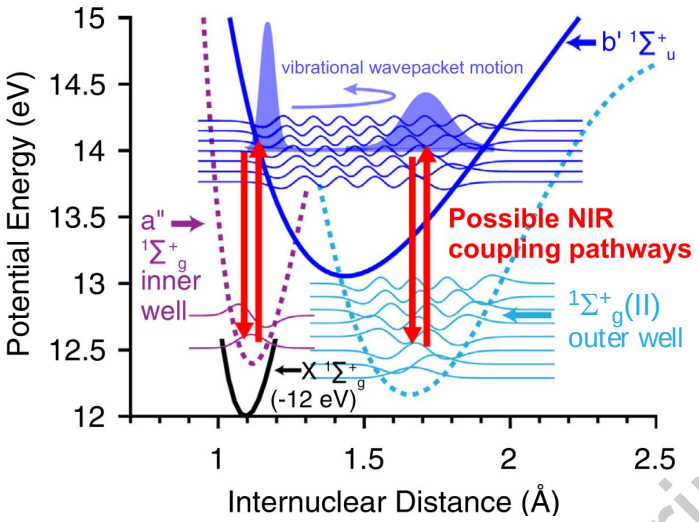

Figure 30. NIR-induced coupling of adjacent vibrational levels in the b' state through the double-well structure composed by the mixed a" $^1\Sigma_g^+$ Rydberg state (inner well) and $^1\Sigma_g^+$(II) valence state (outer well). The wavepacket vibrational levels v = 10–16 are illustrated. Adapted figure with permission from [275], Copyright (2017) by the Elsevier.

state through the double-well structure composed by the mixed a" $^1\Sigma_g^+$ Rydberg state (inner well) and $^1\Sigma_g^+$(II) valence state (outer well) [276], as schematically shown in Fig. 30. This double-well structure is a dark state energetically resonant with the b' valence state via 1-NIR photon. Due to the relative position between the double-well state and the b' state, the coupling is strongly dependent on the internuclear distance. The use of a 12-curve model, based on Born-Oppenheimer approximation, together with the high frequency resolution of ATAS, allowed the authors to measure the anharmonicity of the b' potential energy curve, thus opening the way to the use of ATAS as a structural tool able to characterize the potential well not only of diatomic molecules but also of larger molecules.

An extension of ATAS to polyatomic molecules was reported by Drescher *et al.* [277] with the investigation of the induced dipole response in iodomethane (CH_3I) molecules. An attosecond pulse was used to excite $4d$ core electron of iodine into valence and Rydberg states and a few-cycle NIR pulse was employed to introduce coupling between states and to drive ac Stark shifts of the excited states. The important observation, which turns out to be general in polyatomic molecules and never reported in atoms and diatomic molecules, was the notable differences between the ATAS features of valence and Rydberg states. The main conclusion was that, while the valence states dominate the XUV absorption in the absence of the NIR field, the Rydberg states dominates the NIR-dressed XUV absorption.

3.2.2. ATAS measurements in molecules at absorption edges In all the applications of ATAS to molecular physics discussed so far, a few-femtosecond NIR pulse was

employed to introduce couplings on states excited by attosecond pulses, thus changing the absorption cross section of the sample under investigation. Another class of ATAS measurements in molecules is based on the use of few-femtosecond IR/NIR/visible/UV pulses to excite a molecule and of broadband attosecond pulses to probe the induced dynamics. The approach, in this case, is similar to the one commonly adopted in femtosecond spectroscopy, where a broadband continuum is typically used to probe the evolution of the nuclear dynamics initiated by the absorption of IR/NIR/visible/UV photons. ATAS presents notable advantages, in particular the use of broadband XUV radiation gives access to core levels of different elements, which are spectrally well separated. Spectroscopic methods in this spectral region are sensitive to the elements (due to the highly localized nature of core orbitals on specific atoms of a molecule), to their chemical environment, to their oxidation and spin states, thus offering an extremely rich set of information. For example, in the case of metal complexes (like metalloporphyrinate complexes, such as hemes, porphyrins and chrorins), the measurement of the temporal evolution of transient absorption at the M- and L-edges of the metal contained in the molecular structure is oxidation- and spin-state specific [278]. A few applications of ATAS have been reported in the case of molecules containing halogens or transition metals, since their core-levels (M- and L-edges) are accessible with XUV spectra extending to ~ 150 eV, which can be easily generated with a reasonable XUV photon flux. More recently, ATAS measurements in the water window have been reported: this is of particular importance for the investigation of biologically relevant molecules.

Particularly relevant in molecular physics is the investigation of nonadiabatic processes related to the coupling of vibrational and electronic degrees of freedom, which are at the heart of various processes such as internal conversion, isomerization, proton and electron transfer [279]. In this case the Born-Oppenheimer approximation cannot be adopted, due to the strong coupling between electronic and nuclear degrees of freedom. In particular, this adiabatic approximation cannot be used near a conical intersection of potential energy surfaces belonging to different electronic states [280], where the electron dynamics slow down to the femtosecond time scale of nuclear motion [281]. A detailed experimental and theoretical investigation of the ultrafast processes near a conical intersection represents a challenging problem in molecular physics, since various electronic states are involved and the temporal evolution of the nonadiabatic state-switching can be ultrafast. ATAS is particularly well suited for the investigation of these nonadiabatic processes due to its ability to resolve multi-state dynamics, obtained by measuring the resonant transitions from core orbitals into unoccupied valence orbitals, which provide extreme sensitivity to the orbital occupation, the symmetry and the spin characteristics of the electronic states.

In the last few years, Leone and his group reported on the application of ATAS to the study of conical intersections in diatomic [282] and polyatomic [283, 284] molecules containing halogen atoms to take advantage of the position of M- and N-edges well below 100 eV. In the case of IBr (which is a prototype molecule for nonadiabatic photo-

dissociation dynamics [285]), 200-as pulses, with spectrum extending from 45 to 72 eV, were used to simultaneously probe the $N_{4,5}$ edge ($4d$ orbitals) of iodine and the $M_{4,5}$ edge ($3d$ orbital) of bromine, after excitation induced by visible ($\lambda = 530$ nm), 8-fs pump pulses [282].

The potential of ATAS to investigate the ultrafast molecular dynamics around a conical intersection is not limited to diatomic molecules, as demonstrated by Timmers *et al.* in the case of methyl bromide (CH_3Br) molecules [283]. A 4-fs NIR pulse was used to generate multiple valence WPs in the molecule: a neutral excited-state WP, a ground-state vibrational WP and an ionic spin-orbit coupled WP. The temporal evolution of these WPs was probed by isolated attosecond pulses, with spectrum in the range 60-75 eV, covering the region which corresponds to the transitions from the Br $3d$ core states to valence levels, able to follow the evolution of various competing molecular dynamics with extreme temporal resolution. In particular, it was possible to follow the nonadiabatic population transfer in ~ 15 fs between two states through a conical intersection between the $^1Q_1$ and $^3Q_{0^+}$ excited states, leading to two dissociation pathways converging to Br and Br*. In addition, a vibrational motion with a period $T \approx 54$ fs was measured in the spectral region around 71 eV, which agrees well with the C-Br vibrational period in the ground state of CH_3Br [286], thus indicating that these dynamics are related to a ground state vibrational WP. Finally, a third well distinguished spectral feature in the spectral region between the previous two, has been associated to the evolution of a coherent spin-orbit WP in CH_3Br^+, prepared by tunnel ionization induced by the high-intensity of the NIR pump pulse. In analogy to what measured by Goulielmakis in the case of Kr [56], the pump pulse generated a coherent superposition of two spin-orbit split ground state in the molecular ion, $(e_{3/2})^{-1}$ and $(e_{1/2})^{-1}$, with an energy splitting $\Delta\mathcal{E} = 320$ meV, corresponding to an oscillation period $T_{12} = h/\Delta\mathcal{E} = 12.9$ fs, much longer than the driving pulse. This oscillatory behaviour, with a period $T = 12.7$ fs, was observed by summing over the three ionic transitions L1, $(e_{3/2})^{-1} \rightarrow (3d_{5/2})^{-1}$, L2, $(e_{1/2})^{-1} \rightarrow (3d_{3/2})^{-1}$ and L3, $(e_{3/2})^{-1} \rightarrow (3d_{3/2})^{-1}$: the result is reported in Fig. 31, showing an oscillation with a period $T = 12.7$ fs, as evidence by a Fourier analysis of the experimental data (shown in the inset of Fig. 31). Three snapshots of the oscillation in the electron hole density between p_x and p_y character about the C-Br axis are reported in Fig. 31. Another application of ATAS to the investigation of conical intersection was recently reported by Chang *et al.* [284] in iso-propyl iodide and tert-butyl iodide molecules (i-C_3H_7I and t-C_4H_9I), by measuring the iodine $4d$ core-to-valence transitions after excitation by UV pump pulses (277 nm, 50 fs).

3.2.3. ATAS measurements in the water window A natural extension of the ATAS technique is offered by the extension of the harmonic cutoff up to and even above the water window, since in this case it is possible for example to probe simultaneously the carbon, the nitrogen and the oxygen edges, thus offering the possibility to investigate, with extreme temporal resolution, the electronic and nuclear dynamics in organic matter. The first experimental demonstrations of transient absorption spectroscopy in this

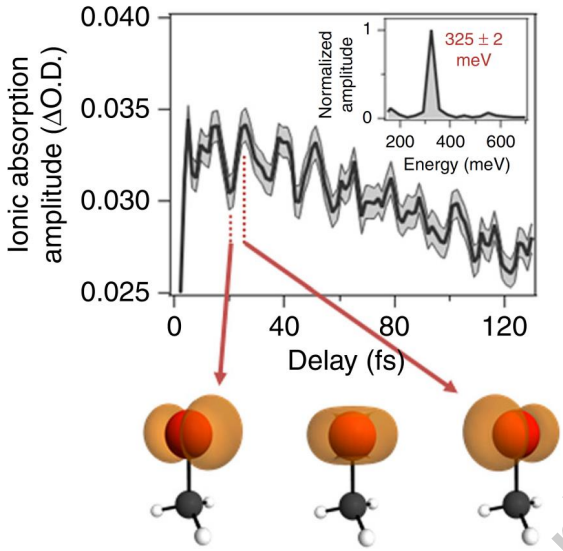

Figure 31. Spin-orbit wavepacket dynamics generated by the strong field ionization process in CH_3Br molecules. The transient ionic absorption amplitude was obtained by summing over the three spin-orbit transitions. The inset reports a Fourier analysis of the experimental data. Lower panel: three snapshots of the electron hole density for CH_3Br^+. Reprinted figure from [283].

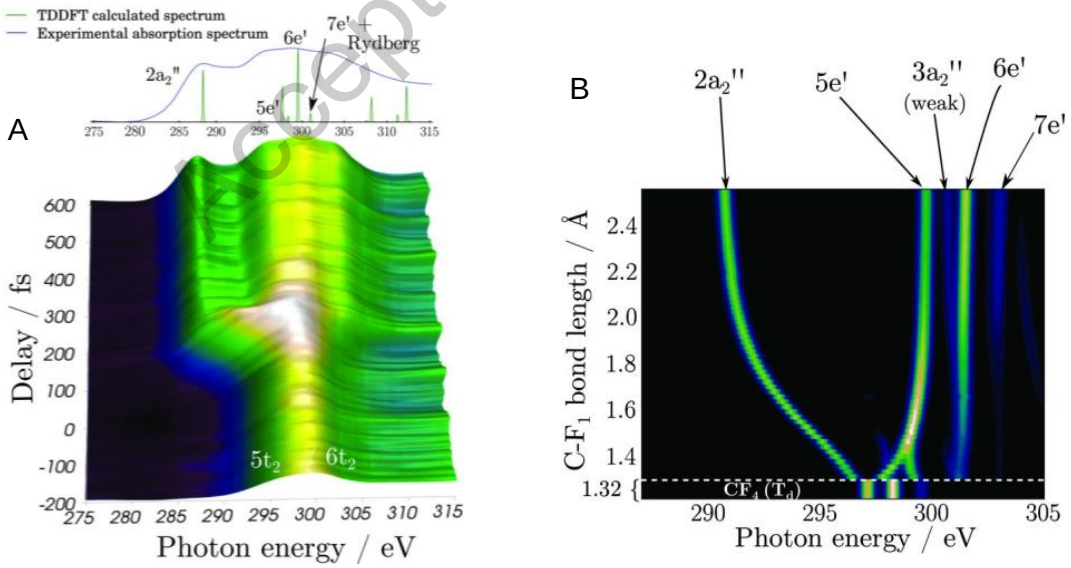

Figure 32. (a) Transient absorption spectrum of CF_4 molecules excited by intense NIR pulses and probed by broadband soft-x-ray pulses. Negative time delays correspond to the soft-x-ray pulse preceding the NIR pulse. (b) Calculated x-ray absorption spectra as a function of the distance of the dissociating C-F bond for the reaction $CF_4 \longrightarrow CF_3^+ + F$. The CF_4 x-ray absorption spectrum is shown below the dashed line. From [287]. Reprinted with permission from AAAS.

spectral region with harmonic sources were reported in 2017 [287, 288]. Pertot *et al.* reported on the investigation of the dissociative ionization of CF_4 and SF_6 induced by intense NIR pulses and probed by transient absorption at the K-edge of carbon and at the L-edges (L_1- and L_{23}-edge) of sulfur. In the case of CCF_4 the dissociation of the initially tetrahedral $CF_4{}^+$ cation into the trigonal planar $CF_3{}^+$ cation breaks the symmetry of the system and leads to the creation of new spectral features in the transient absorption spectrum around the K-edge of carbon, as shown in Fig. 32A. This is corroborated by quantum-chemical *ab initio* calculations: the main result is reported in Fig. 32B, where the calculated absorption spectra around the carbon K-edge is shown vs the distance of the dissociating C-F bond for the reaction $CF_4 \longrightarrow CF_3{}^+ + F$. In agreement with the experimental results, the lowest-energy x-ray absorption $2a_2''$ band undergoes a very large energy shift during the transition from the $CF_4{}^+$ to $CF_3{}^+$ and the absorption spectrum progressively splits into multiple bands. From the measured time-dependent position of the $2a_2''$ absorption band and its position calculated as a function of the C-F separation it was possible to reconstruct the C-F internuclear distance as a function of the pump-probe delay during the dissociation of $CF_4{}^+$.

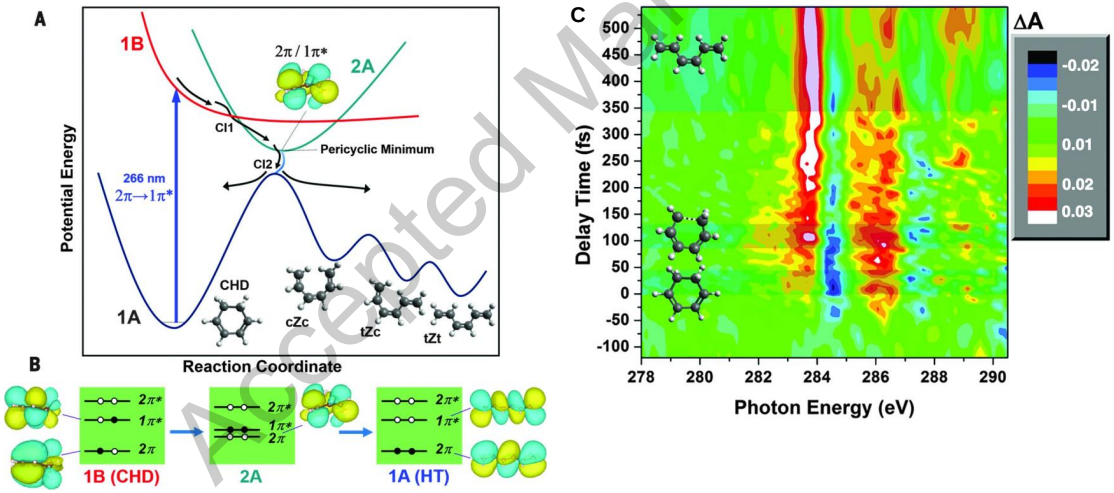

Figure 33. (a) Schematic diagram of the relevant potential energy curves of CHD molecule along the ring-opening reaction coordinate. (b) Schematic orbital diagrams and relevant energy levels at particular points along the reaction coordinate. (c) Transient absorption spectra vs photon energy of the attosecond probe pulses and delay time. Negative time delays correspond to the soft-x-ray pulse preceding the NIR pulse. From [288]. Reprinted with permission from AAAS.

A second application of femtosecond transient absorption spectroscopy based on HHG in the water window was the investigation of ultrafast electrocyclic ring-openings reaction of 1,3-cyclohexadiene (CHD) [288]. In this case 266-nm pump pulses, with a duration of 100 fs, were used to excite the CHD molecules from the 1A ground state to the 1B excited state, photo-exciting an electron from the 2π highest-occupied (HOMO) to the $1\pi^*$ lowest-unoccupied (LUMO) molecular orbital, as displayed in Fig. 33A, thus

initiating the electrocyclic ring-opening reaction. The photo-excited molecule relaxes to the 1A ground state of open-chain hexatriene by means of two conical intersections (CI1 and CI2) and through an intermediate 2A state, where the $1\pi^*$ orbital is doubly occupied and the 2π orbital is unoccupied, as shown in the schematic orbital diagram of Fig. 33B. Around the pericyclic minimum of 2A, these two orbitals are energetically overlapped and mixed. The molecular evolution described above was probed by broadband soft-x-ray pulses, with a spectrum extending from $\sim$ 160 eV to $\sim$ 310 eV. The evolution of the carbon K-edge as a function of pump-probe delay is shown in Fig. 33C, which shows that the molecule evolves towards the 2A state from the initially excited 1B state Franck-Condon region in 60 ± 20 fs and subsequently decays within 110 ± 60 fs to the 1A ground state of the ring-open hexatriene molecule. By using the same experimental setup, the femtosecond intersystem crossing in acetylacetone was measured [289].

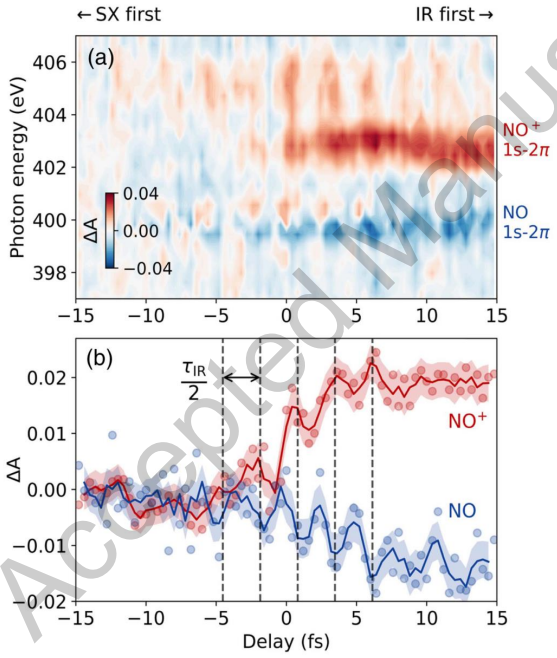

Figure 34. (a) Measured attosecond transient absorption spectrum of NO. (b) Transient absorbance corresponding to the NO $1s \rightarrow 2\pi$ peak (blue circles, averaged from 398.7 to 400.6 eV) and the NO^+ $1s \rightarrow 2\pi$ peak (red circles, averaged from 401.7 to 403.6 eV). Reprinted figure from [290].

A very nice application of ATAS in the water window was reported by Saito *et al.* [290], with the simultaneous measurement of electronic, vibrational and rotational dynamics in nitric oxide (NO) at the nitrogen K-edge (400 eV), after strong-field ionization triggered by 10-fs pump pulses at 1.6 μm. The induced electron and nuclear dynamics were then probed by broadband soft-x-ray pulses. Figure 34a shows the measured transient absorption spectrum. The main absorption features correspond to the $1s \rightarrow 2\pi$ transition of neutral NO around 400 eV and to the $1s \rightarrow 2\pi$ transition of NO^+ around 403 eV. Oscillations are visible on both absorption peaks, with a period of a

half optical cycle of the pump pulse (2.7 fs), as evidenced in Fig. 34b, which displays the transient absorbance corresponding to the two peaks as a function of the pump-probe delay. Interestingly, the phase of these oscillations is opposite for the NO and NO^+ peaks, thus supporting the hypothesis that the origin of the oscillations is the change in the hole population in NO during strong-field ionization, in analogy to what measured in xenon atoms [100]. Upon extending the temporal delay between pump and probe pulses it was possible to measure simultaneously femtosecond vibrational dynamics. Indeed, the delay-dependent central energy of the NO^+ peak at 403 eV was characterized by an oscillation with a period of 14.5 ± 0.1 fs, in very good agreement with the value reported in literature for the vibrational period of NO^+ of 14.23 fs [291]. A vibrational WP is generated on the electronic ground state of NO^+ by ionization, which evolves on the potential energy curve. The corresponding oscillation of the internuclear distance is then directly mapped to the $1s \rightarrow 2\pi$ transition energy. Finally, sub-picosecond rotational dynamics were also measured.

The feasibility of ATAS measurements in the water window was recently demonstrated also with organic molecules and inorganic salts in aqueous solution [292], by using soft-x-ray pulses produced by HHG with spectrum extending from 280 up to 450 eV, generated by multi-mJ, 1.8-μm driving pulses. Static soft-x-ray absorption measurements in transmission were reported on the solvated compounds $O{=}C(NH_2)_2$, $CaCl_2$ and $NaNO_3$ using flat-jet technology.

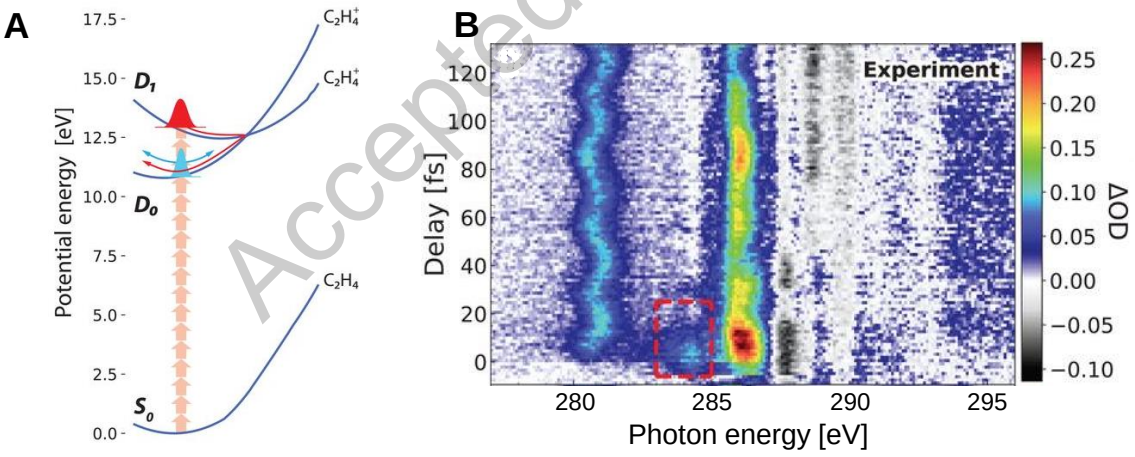

Figure 35. (a) Schematic diagram of the conical intersection between the D_1 and D_0 states of $C_2H_4^+$. (b) Measured attosecond transient absorption spectrum. From [293]. Reprinted with permission from AAAS.

More recently, sub-7-fs conical intersection dynamics were measured by using ATAS at the carbon K-edge in ethylene molecules [293]. Strong-field ionization of C_2H_4 was initiated by $\sim$ 10-fs pulses at 1.6 μm. The IR pump pulse creates WPs both in the ground state, D_0, and in the first excited state, D_1, of the $C_2H_4{}^+$ cation (see Fig. 35A). The WP generated in D_1 undergoes a fast electronic relaxation to the ground state D_0 through a planar conical intersection, which was probed by a broadband attosecond

pulse with spectrum extending to above 450 eV. The measured transient absorption spectrum is shown in Fig. 35B and is characterized by the formation of an absorption peak at 281 eV, with a periodic oscillation of its central position, corresponding to the carbon $1s \rightarrow \pi$ transition into the singly occupied π molecular orbital and a shift to higher energy of the $1s \rightarrow \pi^*$ transition around 286 eV. A remarkable feature of the transient absorption spectra is the absorption peak around 284 eV, indicated by the red-dashed box in Fig. 35B, which decays with a time constant of 6.8 ± 0.2 fs. This short lived band was assigned to the D_1 state and its temporal evolution was interpreted in terms of ultrafast relaxation from the D_1 to the D_0 state through a conical intersection.

3.3. ATAS in solids

The outstanding results obtained in the gas phase motivated the application of ATAS to solid samples [247, 294], especially in dielectrics, where a deeper understanding of the electronic properties is of great importance for the development of high power electronics and signal processing [295].

As in the case of gas samples, the attosecond pulses are combined with phase-locked few-femtosecond IR pulses in a pump-probe fashion. Typically, the few-fs pulse is used to perturb the system while the induced dynamics are probed with the XUV pulse through a resonant transition between an inner level and the material valence and/or conduction bands. Since most common attosecond sources efficiently generate photons below 150 eV, the first experiments in solids traced the system optical response by measuring the absorption around M or L edges (see Tab. 1). Nowadays, the development of attosecond sources in the soft-X region extends the applicability of ATAS to more energetic L or K transitions [296].

In a simplified picture, the optical pump modifies the material charge distribution, e.g. by promoting carriers from a lower occupied state/band to the conduction band, leaving the system in a non-equilibrium state. The excited carriers start then to thermalize mainly through electron interactions (carrier-carrier scattering) or interactions with the lattice (carrier-phonon scattering). Once this process is over (about 100 ps) carrier recombination between the conduction and valence bands brings the system into its initial state. The possibility to disentangle the physical mechanisms responsible for the initial ultrafast relaxation has been long sought in solid-state physics as a better identification and understanding of these processes is a prerequisite for the achievement of active control, material engineering and optimization.

By combining chemical sensitivity, broad band probing and extreme time resolution, ATAS is one of the most promising techniques to disentangle the electron and lattice dynamics unfolding in solids after ultrafast optical excitation. In 2013, using a comb of harmonics in combination with 80-fs pulses centered at 400 nm, J. Vura-Weis and coworkers [298] employed ATAS to study the sub-100-fs charge transfer between O and Fe in $\alpha-Fe_2O_3$. By monitoring the absorbance of the material around the $M_{2,3}$ edge of Fe (Fig. 36), the authors could demonstrate that the peculiar structures observed in the

Element	Edge	Energy (eV)
N	L_1	37.3
O	L_1	41.6
Mg	L_1, $L_{2,3}$	88.7, ∼49.6
Al	L_1, $L_{2,3}$	117.8, ∼72.75
Si	$L_{2,3}$	∼99.62
Ti	M_1, $M_{2,3}$	58.7, 32.6
V	M_1, $M_{2,3}$	66.3, 37.2
Fe	M_1, $M_{2,3}$	91.3, 52.7
Ni	M_1, $M_{2,3}$	110.8, ∼67.1
Ge	$M_{4,5}$	∼29.6
As	$M_{4,5}$	41.7
Se	M_4, M_5	55.5, 54.6
Mo	N_1, $N_{2,3}$	63.2, ∼36.5
Te	N_4, N_5	41.9, 40.4
Bi	O_3, O_4, O_5	92.6, 26.9, 23.8

Table 1. Electron binding energies of some common elements in the XUV spectral region [297].

visible spectrum of hematite originate from a ligand-to-metal charge transfer transition rather than a $d-d$ transition as some calculations seemed to suggest. Moreover, they

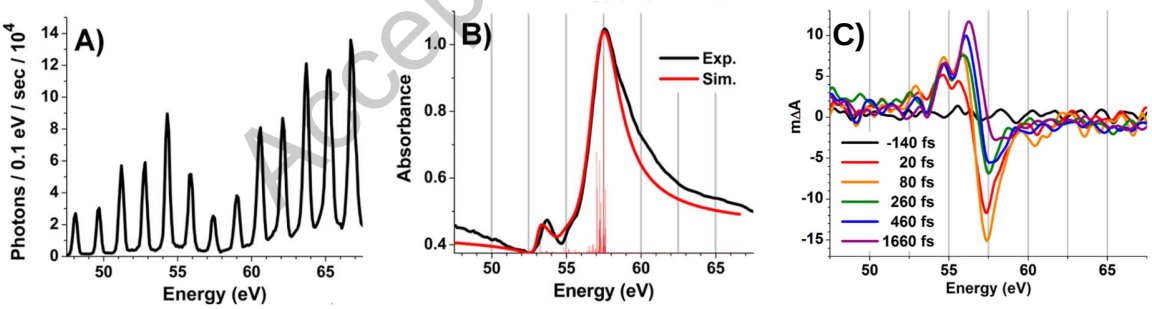

Figure 36. (a) XUV harmonic spectrum passing through a 14-nm thick $\alpha-Fe_2O_3$ pellicle on 100-nm Si_3N_4 substrate. (b) Experimental (black) and calculated (red) absorbance of the $\alpha-Fe_2O_3$ film. (c) XUV transient absorption spectra after 400-nm excitation. Adapted figure from [298], Copyright (2013) by the American Chemical Society.

proved the capability of ATAS to address charge transfer in transition metal oxides. Indeed, one year later, C-M. Jang *et al.* used the same technique to investigate charge transfer between O and Co in Co_3O_4. By measuring the transient absorption of Co around its $M_{2,3}$-edge at 58.9 eV they where able to identify the main mechanism out of six possible excitation pathways [299].

Few years later Zürch *et al.* demonstrated that ATAS is a valuable tool to address the ultrafast energy distribution after excitation in solids [300]. In particular they showed that information about high symmetry points in the k space can still be retrieved even if ATAS is not a momentum-resolved technique. The authors used single attosecond pulses to monitor the $M_{4,5}$ edge in a nanocrystalline Ge film pumped by few-fs IR pulses at 800 nm. Due to the relatively small energy gap of the material (about 667 meV) Ge offers the possibility to monitor directly both the valence and conduction band, which in turn further complicates the interpretation of the data. In order to access the carrier dynamics, the authors made use of an iterative procedure to separate the contribution of the spin-orbit splitting of the core state as well as carrier- and heat-induced band shifts. This allowed the authors to show that after few hundreds of femtoseconds the carrier have scattered to different valleys of the band structure (Fig. 37).

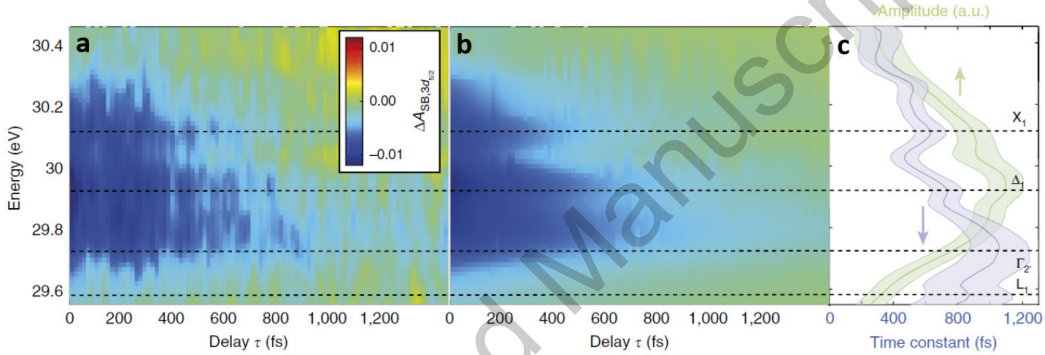

Figure 37. (a) Measured and (b) fitted change of Ge absorbance due to carrier dynamics in the spectral region of the conduction band (CB). (c) Extracted carriers lifetime versus energy. Adapted figure from [300].

More recent experiments in Si [301] and Si-Ge alloys [302] further proved the capability of ATAS to resolve carrier and phonon dynamics from the few femtosecond to the picosecond domain. On these time scales, the possibility to unveil the interplay between the initial electronic excitation and the lattice with element-sensitive probing makes ATAS an ideal tool to study other important phenomena like the formation of coherent optical phonons [303] and polarons [304], as well as to study inter- and intra-band carrier relaxation [305]. Being capable to address structural and charge dynamics, ATAS can also be used to investigate ultrafast phase transitions in solids. A remarkable example are metal to insulator transitions (MIT) which happen in correlated materials where, for most of the cases, it is not clear whether the primary mechanism of the MIT is an electron-lattice interaction (Peielrs transition) or an electron-electron interaction (Mott transition) [306]. In 2017 M.F. Jager *et al.* [307] used ATAS to investigate the ultrafast MIT that happens in a prototypical Mott insulator like VO_2 (Fig. 38). The authors used a few-fs IR pulse centered at 800 nm to initiate the MIT while the ultrafast dynamics of conduction and valence bands have been monitored with an attosecond pulse centered at the $M_{2,3}$ Vanadium edged (at about 39 eV). Their results indicate that in polycrystalline VO_2 the MIT occurs on a time scale of 26 ± 6 fs,

well above the 6-fs instrument response function of their setup. While this result seems to exclude a purely photon-driven mechanisms, thus supporting a Mott-like transition as opposed to Peierls, structural involvement cannot be completely ruled out. Indeed, a pure electron-correlation-driven transition is expected to evolve on a much faster time scale, comparable to inverse of the plasma frequency, i.e. about 4 fs. Further investigation is needed to understand whether the MIT is driven by tightly intertwined electronic and structural effects [308], or whether the results depend on the crystallinity degree of the sample.

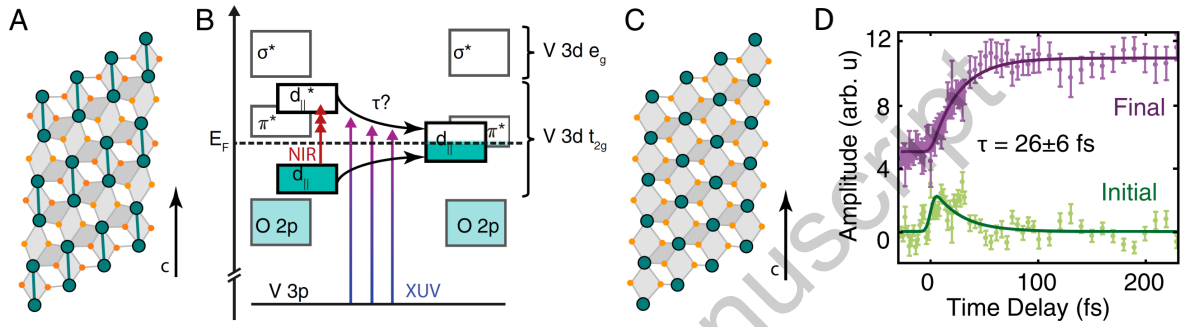

Figure 38. (a) Monoclinic crystal structure of the insulating VO_2 ground state characterized by the existence of dimerized chains of V atoms (green lines). (b) Schematic of the electronic structure and the pump-probe mechanism. The IR pulse initiates the phase transition which is monitored via core-level transitions by the attosecond XUV radiation. (c) Rutile structure of the system metallic phase. (d) Kinetic behaviour of the spectral signatures of the initial (green) and final (violet) charge distributions underling the transition from a insulator to metallic phase. Adapted figure from [307].

To extend ATAS to the X-ray spectral region constitutes a fascinating field of research which will widen the applicability of the technique, enhancing its chemical and state sensitivity. First steps in this direction have already been moved. A. Britz *et al.* studied femtosecond carrier dynamics in 2 H−$MoTe_2$ by using soft x-ray transient absorption spectroscopy at the x-ray free-electron laser (XFEL) of the Pohang Accelerator Laboratory [309]. In their experiment the authors excite electrons above the 2 H−$MoTe_2$ band gap with a 400-nm pulse and then probe the carrier distribution by monitoring the absorption probability at the Te M_5 edge (572-577 eV). This allowed them to investigate at once hot electron relaxation and electron-hole recombination in real time. This pioneering work paves the way for the exploitation of the unique capabilities of XFELs. Indeed, by working at high photon energies these sources offer the possibility to perform time-resolved studies at deeper core edges where the large spin-orbit splitting minimizes the adverse overlap of adjacent transitions. Moreover, the high photon flux, the tunability and the smaller spot sizes make these sources extremely versatile widening even further the applicability of attosecond time-resolved full-optical techniques.

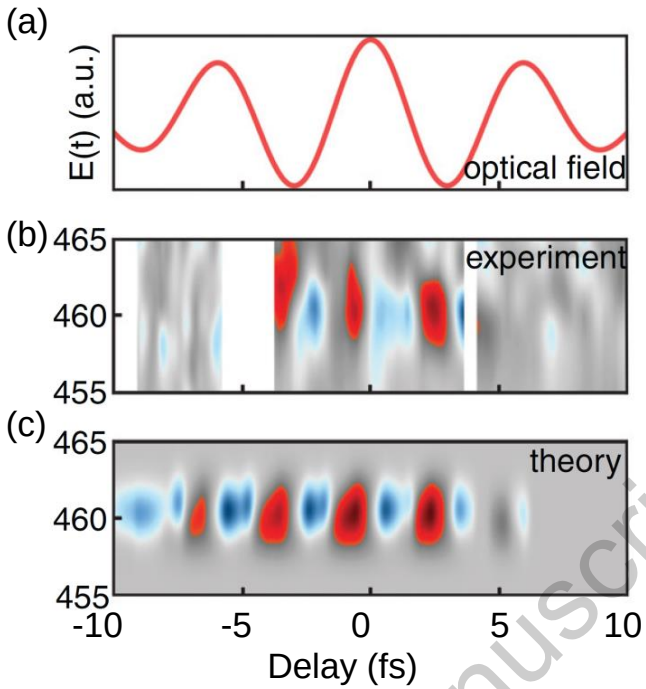

Figure 39. (a) Optical pump field. (b) measured, (c) calculated, transient absorbance trace measured in TiS_2 as a function of the pump-probe delay around the Ti L-edge at 460 eV. Both traces show clear sub-cycle oscillations which appear during the pump-probe temporal overlap and originate from ultrafast carrier motion. Adapted figure with permission from [310], Copyright (2021) by AIP Publishing.

XFELs are not the only option to access energetic core level transitions. B. Buades *et al.* generated isolated attosecond pulses around the Ti L-edge (at about 460 eV) with a table-top setup and used this radiation to perform X-ray absorption near-edge spectroscopy of TiS_2 with attosecond resolution [310]. In this latter case, instead of addressing the relaxation mechanisms which happen after optical excitation the authors exploited the extreme time resolution of ATAS to study carrier motion during light-matter interaction (Fig. 39). This constitutes a unique feature of ATAS which has been recognized since the first pioneering experiments with condensed targets. In 2012 M. Schultze *et al.* first extended ATAS to solid samples and studied sub-fs carrier dynamics in SiO_2 (energy gap $E_g = 9$ eV) [311]. They used a 4-fs NIR pulse to pump a 125-nm thick free-standing SiO_2 sample and later probed the induced dynamics with a 72-as pulse centered around the Si $L_{2,3}$ edge at ~ 99 eV. Similar to what found by Baudes *et al.*, the recorded pump-probe absorption trace showed a modulation of the transient signal which oscillates with twice the NIR central frequency (Fig. 40(a) and (b)). Outside the region of temporal overlap between pump and probe the system absorption shows no pump-induced modifications. On the one hand, this suggested that 2ω-oscillations originate from strong-field phenomena like Wannier-Stark localization [313]. On the other hand these results proved that NIR pulses could be used to induce reversible changes in the optical response of dielectrics whose underlying physical properties could

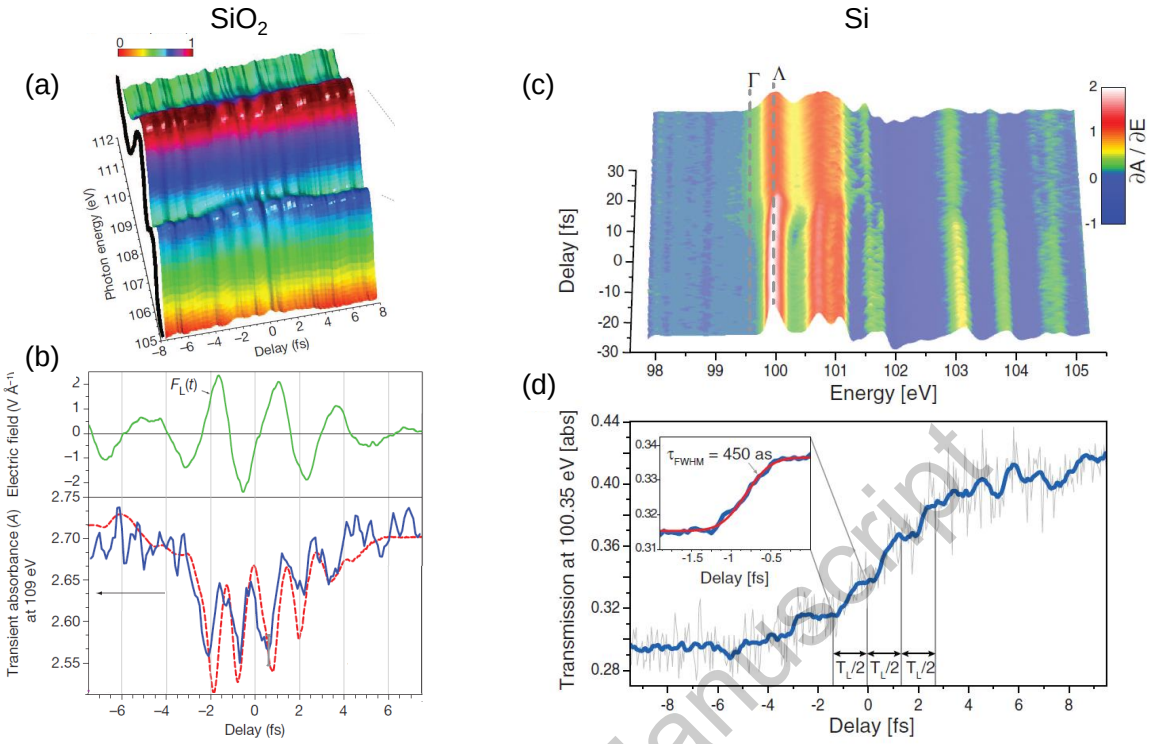

Figure 40. (a) Attosecond transient absorption trace of SiO_2 around its $L_{2,3}$ edge. (b) The NIR pump electric field (green curve, top panel) and the transient change of the absorption in a 1-eV window centered at 109 eV (blue curve, bottom panel) along with the theoretical prediction (red dashed curve). The transient signal recovers soon after the temporal overlap and shows clear 2ω-oscillations. (c) Energy derivative of the Si XUV absorbance plotted as a function of the pump-probe delay. (d) Temporal evolution of the XUV transmission at 100.35 eV revealing a step-like build-up connected to the carrier injection by tunnelling. Adapted figure from [311] (copyright (2012) by Springer Nature) and [312] (reprinted with permission from AAAS).

be controlled on the time scale of the pump optical period. Few years later A. Moulet *et al.* repeated the experiment and showed that the ultrafast features observed in the SiO_2 absorption between 104 and 110 eV originate from the formation of an exciton made by a conduction-band electron and a Si $2p$ core hole [314]. Due to Auger decay and phonon coupling these core-excitons are characterised by a relatively short lifetime (of the order of few fs) and therefore need the high time resolution of ATAS to be observed.

The possibility to disclose the nonlinear processes which govern light-matter interaction in solids on sub-fs time scales [315–317] motivated the scientific community to further explore the applicability of ATAS to dielectrics, semiconductors and metals. In 2014 M. Schultze *et al.* applied the same scheme to investigate the carrier injection mechanisms in Si, where they found a transient signal which does not recover immediately after the pump-probe temporal overlap [312] (Fig. 40(c) and (d)). Si is a semiconductor characterized by a direct energy gap of about 3.2 eV, closer to the NIR central photon energy of $\sim$ 1.6 eV. In this case the pump field can promote real

carriers from the material valence band (VB) to the conduction band (CB) via tunnel ionization, which in turn modifies the XUV absorption probability around the $L_{2,3}$ Si edge. By linking the temporal profile of the absorption edge with the number of injected electrons in the CB, the authors found an upper limit of ~ 450 as for the carrier-induced band-gap reduction and the electron-electron scattering time in the CB.

As already evident in these first two experiments, the exact dynamics initiated by a strong few-cycle NIR pulse strongly depends on the energy gap of the material under consideration. When the energy gap is comparable to the NIR photon energy, carrier injection in the CB can happen either by resonant one photon absorption, by tunneling or multi-photon absorption. The parameter which is used to discriminate between the two regimes is the Keldysh parameter [318] defined as:

$$\gamma_K = \frac{\omega}{|e|E_0}\sqrt{m^* E_g}, \tag{15}$$

where e is the electron charge, E_0 is the electric field strength in the material, ω is the field central frequency, m^* is the reduced electron-hole mass and E_g is the material energy gap. Figure 41(a) shows the Keldysh parameter calculated for SiO_2 as a function of the field strength and frequency. When $\gamma_K \ll 1$ the interaction with the field is at the quasi-static limit (QS), while for $\gamma_K \gg 1$ multi-photon absorption is expected. For intermediate values, i.e. $\gamma_K \sim 1$, the carrier injection across the forbidden region happens by tunneling. As reported in Fig. 41(a), at 800 nm pump field intensities

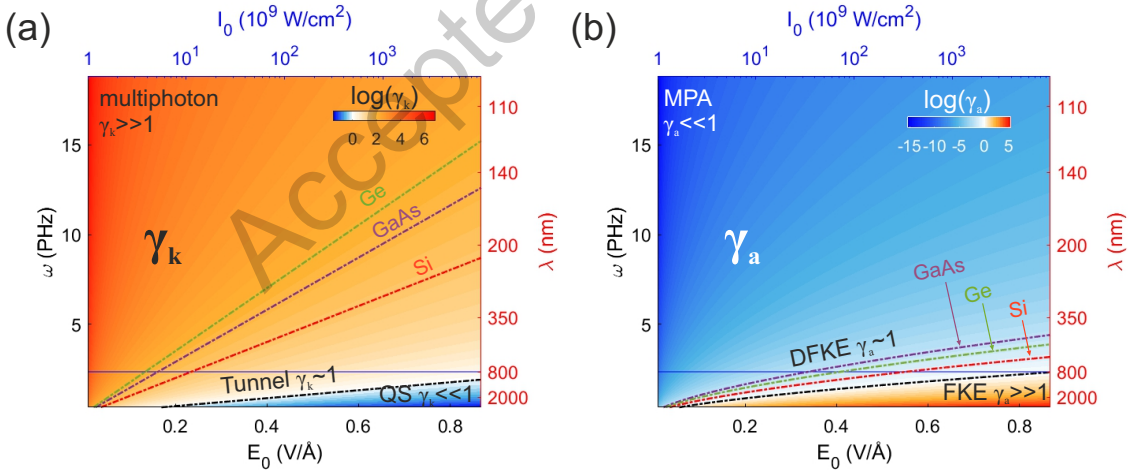

Figure 41. (a) Keldysh parameter, γ_k, and (b) adiabaticity parameter, γ_a, calculated for SiO_2. In both panels, false colors represent the logarithm of the parameter. The horizontal blue line marks the position of $\lambda = 800$ nm, while the black dash dotted curves indicate the values for which γ_k or γ_a equal one. The red, violet and green dash-dotted curves represent the same quantity but for Si, GaAs and Ge, respectively. MPA stands for multi-photon absorption, FKE and DFKE indicate the static and dynamical Franz-Keldysh effect, while QS stands for quasi-static regime. The values of energy gaps and reduced masses used for the computations are taken from [319].

higher than 10^{13} W/cm^2 are needed to reach this regime in SiO_2. In Si, instead, the

tunneling regime is reached at significantly lower intensities (red dot-dashed curve in Fig. 41(a)) thanks to the reduced energy gap. If the field peak intensity and the energy gap of the material are carefully chosen, the NIR few-fs pulses typically used in ATAS experiment can also allow for investigating the case of $\gamma_K \gg 1$. Using a NIR intensity of about $10^{10}\,\mathrm{W/cm^2}$, almost 100 times smaller than what used in Si, and moving to a dielectric with bigger energy gap as GaN ($E_g \simeq 3.35\,\mathrm{eV}$), H. Mashiko and coworkers studied the opposite multi-photon carrier injection regime [320]. Probing directly the VB and CB with attosecond pulses, without the need for a core level transition, the authors observed fast oscillations with a period of 860 as in the transient absorption trace. These oscillations are localized in the temporal region of pump-probe overlap and originate from a multi-photon process where an electron is promoted from the VB to the CB upon absorption of three NIR photons. As such, it corresponds to a 3ω frequency component, at about 1.16 PHz. Therefore, with this experiment the authors reported the first evidence for PHz carrier manipulation in dielectrics, demonstrating that it is, in principle, possible to envision high-speed signal processing technologies based on wide-bandgap dielectrics which go beyond the current THz operation limit [295]. More recently the same group repeated the experiment in Cr:Al_2O_3 where they observed the absorption to oscillate with higher frequencies, up to 7ω, providing clear evidence for multi-photon carrier injection with simultaneous absorption of ≤ 7 NIR photons [321]. This result suggest the possibility to manipulated carrier in dielectrics with even higher frequency, up to 2.6 PHz.

Starting from what observed in Si, one may wonder what will be the main carrier injection mechanism with intense IR pulses ($10^{11} - 10^{12}\,\mathrm{W/cm^2}$) when the energy gap is comparable to the photon energy. To study this problem F. Schlaepfer *et al.* used few-fs NIR pulses to promote carriers from the VB to the CB ($E_g = 1.42\,\mathrm{eV}$) in a single crystalline 100-nm-thick GaAs target and probed the resulting dynamics by exciting electrons from the As-3*d* core levels to available states around the bandgap region (40.73 eV below the VB top [322]). As a consequence of the carrier injection by the NIR field, the authors found a reduced probability for the As-3*d* to CB transition (respectively increased absorption in the VB). On top of a monotonic decrease of the absorption the pump-probe trace shows clear 2ω-oscillations around the zero delay (Figs. 43(a), (b)). These oscillations may originate either from the inter-band transition initiated by the NIR field or by the intra-band motion of virtual and real charges. While the first mechanism can be associated with a resonant one-photon transition where the pump can be described in a quantized photon picture, the latter relies on a classical description of the NIR field. In order to distinguish between the two effects the authors evaluated the relative phase delay of the 2ω-oscillating patters with respect to the NIR pump and compared it with first-principle calculations (Fig. 43(c)). Contrary to what suggested by the intuition, intra-band motion is found to play a dominant role in defining the timing of the oscillatory signal. In addition, the authors showed that the virtual carriers created by the intra-band motion significantly boost the injection of real carriers from the VB into the CB (Fig. 43(c)). This new excitation regime was never observed before and

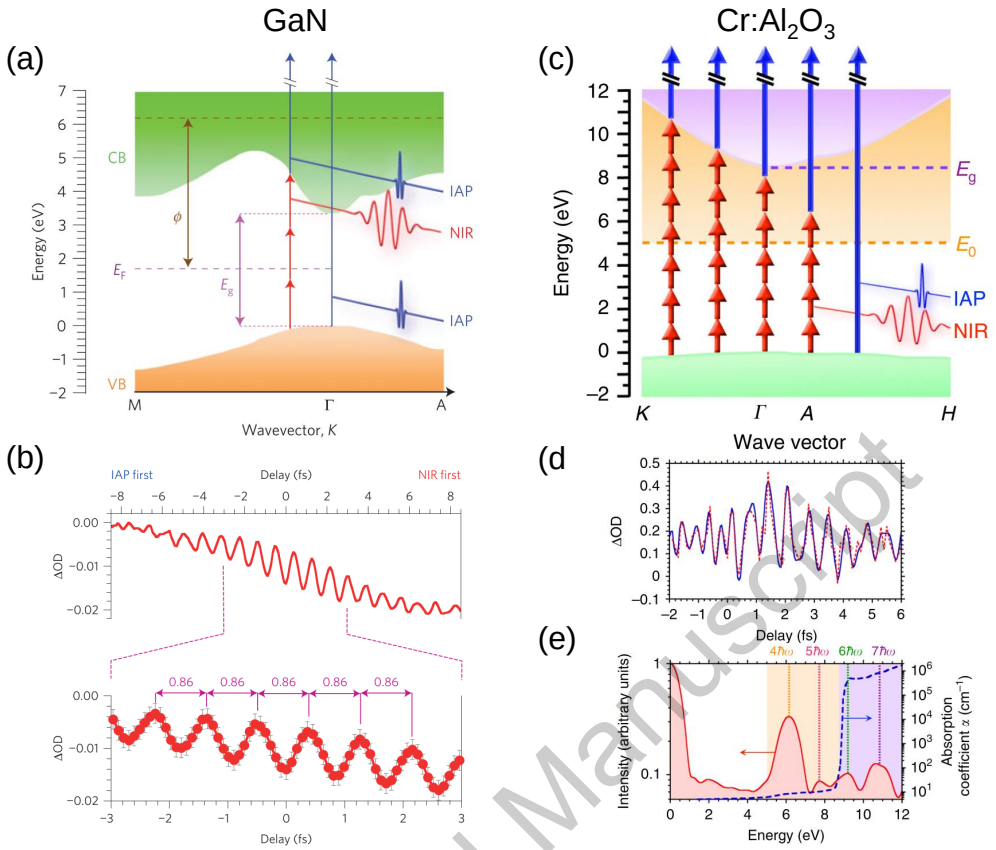

Figure 42. (a) Valence and conduction bands of GaN together with a schematic of the 3-NIR absorption process and the XUV probing mechanism. (b) Integrated optical density variations in the region between 17.5 and 23.5 eV. Clear oscillations with a period of 860 as, corresponding to three times the NIR frequency, are observed. (c) Same as in (a) but for Cr:Al_2O_3. Due to the wider energy gap (about 8.7 eV) higher order multi-photon process can occur. Indeed the transient optical density between 38 and 46 eV, (d), shows higher frequency components, clear evident in its Fourier transform (e) and correspond to the absorption of 4 to 7 NIR photons. Adapted figure from [320] (copyright (2016) by Springer Nature) and [321].

showed that strong field effects may allow ultrafast optical control of carrier injection also with a resonant pumping mechanism [316].

It is worth noticing that the interplay between inter-band transitions and intra-band motion is object of debate in solid-state strong-field physics [324, 325]. A parameter often used to discriminate between the classical and quantum description of the pump field is the adiabaticity parameter γ_a, defined as the ratio between the ponderomotive energy and the photon energy [326]:

$$\gamma_a = \frac{U_P}{\hbar\omega} = \frac{e^2 E_0^2}{4m^*\hbar\omega^3} \tag{16}$$

As observed for the Keldysh parameter, also γ_a scales with the field intensity and frequency (Fig. 41(b)). When $\gamma_a \ll 1$ the field is better described by its quantum nature and multi-photon absorption. When $\gamma_a \gg 1$, instead, the field classical

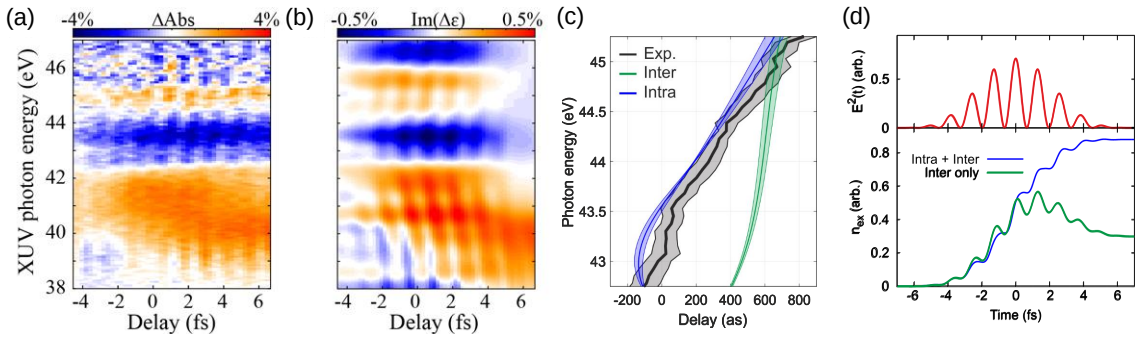

Figure 43. (a) Measured, (b), calculated transient absorption trace for a single-crystal GaAs around the As 3*d* to CB transition. (c) Energy dependent phase delay of the 2ω-component of the transient signal in A. The black solid curve displays the experimental results while the phase delays computed by including only intra-band motion or inter-band transitions are shown in blue and green, respectively. (d) upper panel, square of the instantaneous pump electric field. The lower panel reports instead the computed CB population as obtained with a model that allows both inter- and intra-band mechanisms (blue curve), or considering only vertical transitions between the VB and the CB (green). Adapted figure with permission from [323], Copyright (2018) by Springer Nature.

description prevails and fundamental processes related to intra-band motion, like the Franz-Keldysh effect (FKE), dominate [327]. In brief, the external field bends the crystal potential accelerating the electron-hole pair. The exponential tail of the electron-hole wavefunction extends into the energy gap allowing for the absorption of photons of energy $\hbar\omega < E_g$. For this reason FKE is often referred to as photon-assisted tunneling through a distance that depends on the field strength. When the field description transits from classical to quantum ($\gamma_a \sim 1$) induced above-gap transparency and optical side bands formation are observed in addition to the below-gap absorption [328]. This phenomenon, called dynamical Franz-Keldysh effect (DFKE) is an ultrafast non-resonant process based on virtual carrier intra-band motion. The DFKE effect can be observed around the energy gap of dielectrics with time-resolved experiments in the terahertz regime (picosecond time scales) [329, 330]. Its observation in the PHz domain is hindered by the required high field intensities which can either excess the material critical field or promote too many real carriers into the CB, making the detection of pure virtual carrier dynamics a practically impossible. A remarkable example is the above cited work on GaAs, where the real carrier injection makes the system response to deviate from a pure DFKE picture, even if $\gamma_a \simeq 1.4$.

One way to overcome this limit is to follow the approach proposed by M. Lucchini *et al.* and observed the material response deeper into the CB at higher probing energies [331]. In this work the authors used an attosecond pulse of 150 as, centered at about 42 eV in combination with few-fs NIR pulses to study the optical response of a 50-nm polycrystalline diamond pellicle. Following the ATAS scheme the authors observed a transient signal oscillating with 2ω frequency, confined to the region of pump-probe

temporal overlap. The oscillations show a distinctive V-shaped pattern (Fig. 44(a)) which shape and timing can be fully reproduced by time-dependent density functional theory calculations (TDDFT) [332]. As the V-shaped dispersion can be reproduced with a simplified 2-band model based solely on intra-band motion and developed to describe the DFKE [326], it is clear that it originates from this process. Nevertheless, a clear explanation of why DFKE should manifest in a V-shaped dispersion of the 2ω-oscillations is still missing. Theoretical simulations have shown that both the phase of the oscillations and the aperture of the V-shape depend on the pump field intensity [326] and wavelength [331]. Furthermore, the actual value of the electron-hole reduced mass could also play a role. Therefore, the DFKE observed between different couples of valence and conduction sub-bands, characterized by different curvatures, may result in a different dispersion pattern. This interesting scenario offers the possibility to use ATAS and DFKE to study the electronic bands in dielectrics without the need for resonant core-level transitions.

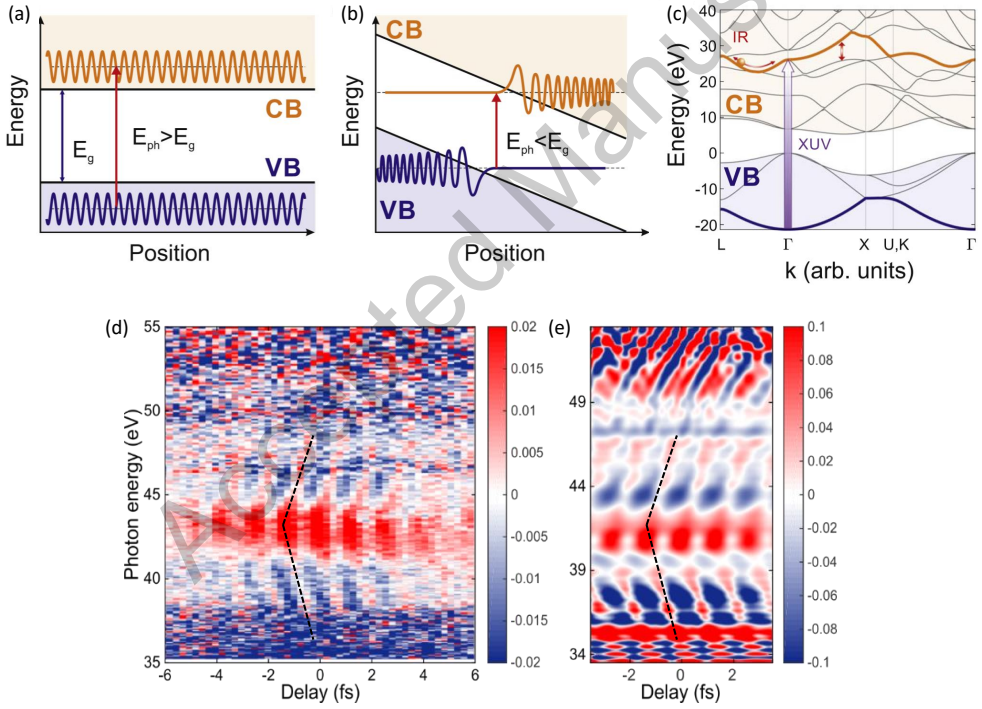

Figure 44. (a) Schematic of two electronic states in conduction and valence band (CB, VB). Normally only photons with an energy $\hbar\omega > E_g$ can be adsorbed. (b) Same situation in the presence of an external field that induces DFKE. Absorption below the energy gap becomes feasible. (c) Diamond band diagram showing the VB and CB sub-bands involved in the DFKE which characterized the material optical response at about 42 eV. (d) Experimental transient absorption trace showing the characteristic 2ω-oscillations with V-shaped dispersion (black-dashed line) associated with the DFKE. (e) TDDFT calculations fully reproducing the experimental results. Adapted figure with permission from [331] and from [332], Copyright (2016) by the American Association for the Advancement of Science.

All the materials discussed so far are characterized by a finite band gap. The

question might come natural if ATAS is limited to semiconductors and insulators, or whether it can be apply to conductors where $E_g = 0\,\text{eV}$ [333]. In 2019 Volkov and coworkers used ATAS to study ultrafast carrier dynamics in a Ti free-standing film, pumped with a strong ($10^{12}\,\text{W/cm}^2$) few-fs NIR pulse [334]. Their results show that the NIR field induces clear changes in the sample transmission around the Ti $M_{2,3}$ edge at 32.6 eV. Instead of showing oscillations, in this case the transient signal is found to rather increase monotonically, following the pump laser fluence (Fig. 45). Comparing their results with TDDFT calculations the authors showed that the transient signal is sensitive to the dynamics of screening and collective electron motion via many-body effects. In particular, the enhanced absorbance is associated to an ultrafast screening process around the Ti atom due to increased electron localization. The calculations showed that the NIR pump induces an increase in the population of the Ti $3d$ orbitals. Due to the inefficient screening of the $4s/4p$ electrons, this process causes a build up of the charge density around the Ti atom which follows the laser fluence in a fashion similar to the absorption transient signal (Fig. 45(e)). This ultrafast photo-induced change in electron localization depends only on the different properties of the d orbitals and not on the particular material under investigation. Therefore, the observed phenomenon is expected to govern the first steps of light-interaction in transition metal compounds, suggesting a way to manipulate electron localization prior thermalization.

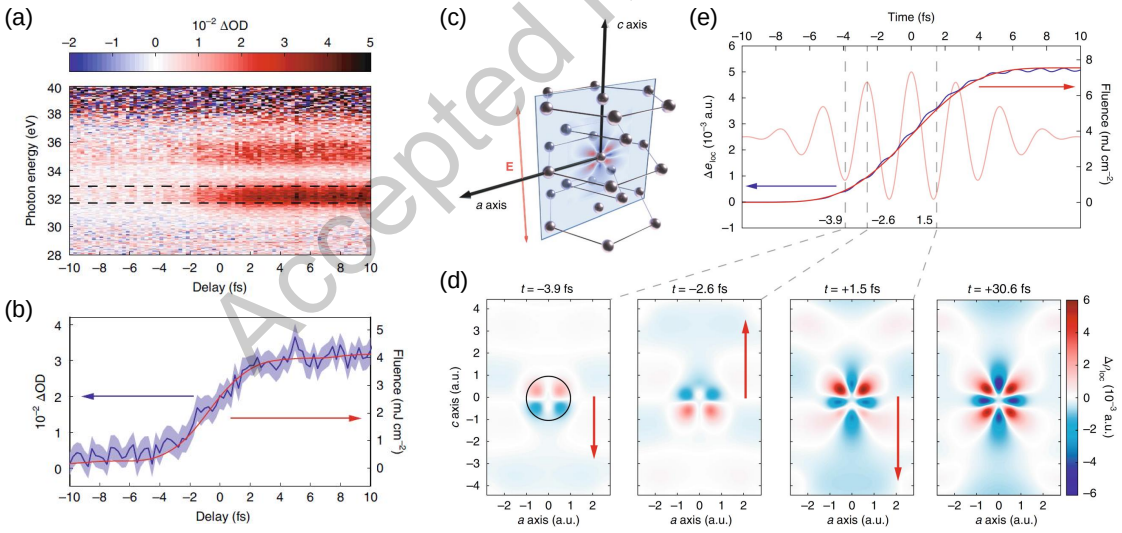

Figure 45. (a) ATAS trace recorded around the $M_{2,3}$ edge of a Ti pellicle. (b) Delay-dependent variation of the Ti optical density, obtained by integrating the signal in (a) between 31.7 and 32.9 eV (blu curve), compared to the pump laser fluence (red curve). (c) simulated Ti hcp cell with the c axis parallel to the pump laser field. (d) Pump-induced electron density changes in the c-a plane (blue area in C) for different instants of time. (e) Pump laser (orange curve), and laser fluence (red curve), compared to the induced changes of the charge density around the Ti atom (blue curve), as calculated in the area delimited by the black circle in D. Adapted figure with permission from [334], Copyright (2019), the Authors, under exclusive licence to Springer Nature Limited.

Electron and lattice dynamics are not the only ultrafast processes of interest that

can be tackled with ATAS in solids. When combined with circularly polarized XUV radiation, [335–339] ATAS is a perfect tool to investigate the magnetic properties of matter. The existence and nature of the mechanisms which govern coherent magnetic dynamics during light-matter interactions are a highly debated topic in solid state physics. The proposal of such effects, which may originate in relativistic quantum electrodynamics, beyond spin-orbit interaction, traces back to 2009 [340]. Ten years later F. Siegrist *et al.* used a circularly polarized attosecond to probe the transient absorption of a Ni/Pt-multilayer sample around Ni $M_{2,3}$ edge, for opposite target magnetizations [341]. Performing one of the first examples of attosecond time-resolved magnetic circular dichroism, the authors observed optically induced spin and orbital momentum transfer (OISTR) [342], investigating the ultimate speed limit of future coherent spintronic applications, spin transistors and data storage media.

3.4. ATRS

The relatively low photon flux of the actual attosecond sources and the different propagation speed of pump and probe light into dispersive matter, are the main reasons which limit the applicability of ATAS to relatively thin samples (typically $\leq 200\,\mathrm{nm}$). Since not all samples can be prepared in regular thin films, this strongly limits the range of applicability of ATAS. Moreover, even when it is possible to produce the samples of the required thickness, due to the poor heat conduction of thin films negative effects like thermal damage or unwanted persistent absorption artefacts such as heat-induced band shifts [300] can happen at lower pump intensities that what required for a bulk sample. To avoid these issues and be able to probe massive targets one way is to measure the sample reflectivity rather than the sample transmission, thus performing attosecond transient reflection spectroscopy (ATRS).

ATRS clearly profits by a wider range of applicability, making it the technique of choice for those samples which cannot be reduced to thin samples. In addition, while ATAS is bulk sensitive, ATRS in the XUV is mostly surface sensitive [343] and allows for the study of the chemistry of interfaces [344, 345]. While one of the first implementation of ATRS traces back to 2008 [346], where E. Papalazarou and coworkers used harmonic radiation to a study coherent phonons in Bi, so far only few examples of ATRS are reported in literature. The main reasons being the increased complexity of both the setup and data interpretation. For example, to measure the static reflectivity is more complex than to measure the static absorption of a pellicle. While the latter can be done by simply removing the sample from the beamline, without changing the subsequent light path, the first requires the accurate measurements of the incoming radiation flux, typically done by measuring the reflection after a known target (e.g. a gold mirror). Any geometrical misalignment between the unknown sample and the reference surfaces could introduce artefacts in the measured static reflectivity. Moreover, if it is relatively easy to change the light incidence angle in an ATAS setup (it is sufficient to rotate the sample), with ATRS the same operation requires additional motorized

folding mirrors in order to guarantee that the alignment with the XUV spectrometer is not lost [347], thus increasing the beamline complexity. As the reflectivity properties and the sensitivity to the induced dynamics strongly depend on the light incidence angle, for an ATRS setup it is almost mandatory to be able control the incoming light direction. This dependence further complicates the physical interpretation of an ATRS trace too. While the absorption properties of a material are related to the real part of its dielectric function solely, the reflection coefficient depends on both the imaginary and real part [348], with a sensitivity that changes with the incidence angle. To mitigate this aspect, usually the experiments are performed at the critical angle for total external reflection of the XUV light $\theta_c(\omega) = \arcsin(n(\omega))$, with ω being the light angular frequency and n the energy-dependent material refractive index. Besides corresponding to a field amplitude enhancement inside the solid, at θ_c the sensitivity of the reflectivity to the imaginary part of the dielectric function is minimized. Using this scheme Kaplan *et al.* studied simultaneously electron and hole dynamics in Ge [349]. R. Geneaux and coworkers used instead the Kramers-Kronig relations to disentangle the contribution of real and imaginary part of the dielectric function. In this way they could to retrieve the absorption properties starting from the measured reflectivity and study ultrafast core-exciton dynamics in MgO [350]. Despite the outstanding results obtained with ATRS, none of the above cited works shows a clear attosecond dynamics even if the probing is done with a single attosecond pulse. Very recently, Lucchini *et al.* demonstrated that this is not an intrinsic limit of the technique by reporting the first example of true attosecond dynamics measured with ATRS [58]. In particular, they studied the attosecond and nanometric motion of Wannier excitons in a MgF_2 single crystal, disentangling the dual atomic-solid nature of these fundamental quasi-particles. In their experiment, a few-fs and intense ($\sim 10^{12}\,\mathrm{W/cm^2}$) IR pulse is used to perturb the crystal while an isolated attosecond pulse simultaneously creates and probes core-excitons obtained by ionizing a Mg^{2+} $2p$ state around 56 eV below the CB. The differential reflectivity trace (Fig. 46(a)) shows rich dynamics around the Mg $L_{2,3}$ edge where the static reflectivity is characterized by a clear peak (at about 54.6 eV) associated to the core exciton formation [351]. The dynamics, fully reproduced by a 1D Wannier-Mott model [352, 353] (Fig. 46(b)) unfold on two distinct time scales. On a few-fs time scale (Fig. 46(c)) the transient reflectivity is characterized by derivative profiles typical of the ac-Stark shift [354] and already observed in MgO [350] and Si [314]. These phenomenon originates from the coupling of bright and dark exciton states induced by the IR pulse and can be fully explained within an atomic-like, two-level model. On a faster (attosecond) time scale, the sample reflectivity oscillates with twice the IR central frequency (Fig. 46(d)). While the optical Stark effect could in principle be the cause for the observed 2ω-oscillations, a detailed analysis of the oscillation absolute phase delay, made possible by the unique two-foci geometry used in the experiment [347], showed that the sub-fs signal is instead related to the DFKE, as underlined by the characteristic V-shaped dispersion of Fig. 46(e). Conversely from what observed for the fs (atomic-like) response, the observed attosecond dynamics are hence a solid-like

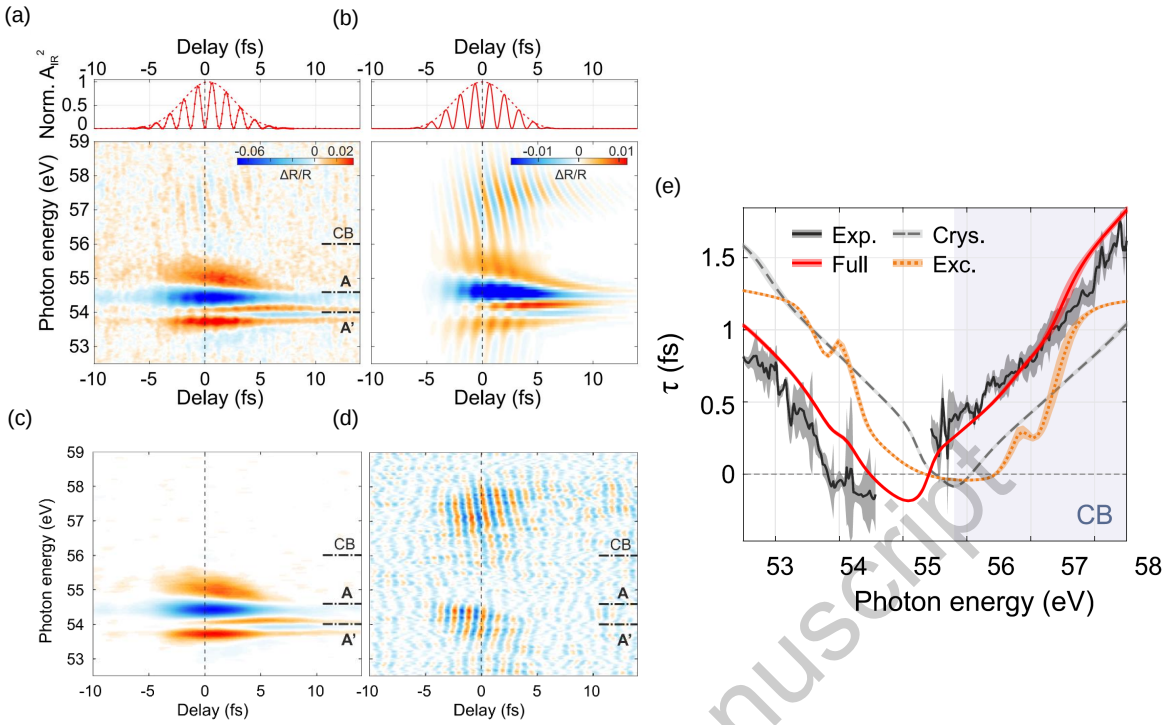

Figure 46. (a) Experimental, (b) calculated, differential reflectivity traces for a MgF_2 single crystal measured around the Mg $L_{2,3}$ edge, as a function of the delay between the XUV and IR pulses measured. The upper panels show the square of the IR vector potential obtained through simultaneous streaking measurements. The delay zero (vertical dashed line) has been chosen in order to coincide with the central minimum of the IR vector potential. (c), (d), fs and sub-fs components of the trace in (a), obtained by Fourier filtering. (e) Phase delay of the 2ω-oscillating part of the transient signal. In black the experimental data, in red the prediction of a 1D Wannier-Mott model, in orange dotted and gray dashed the calculation obtained considering only the excitonic contribution (atomic-model) or only the crystal contribution (solid-model). As it is possible to see, the full system and the pure crystal responses have the same V-shaped dispersion typical of the DFKE. Adapted figure with permission from [58], Copyright (2021), the authors.

effect originating by intra-band motion of dispersive states. These dual aspects of the excitonic quasi-particle, previously found to compete in time-averaged measurements [355], can be addressed separately because of the extreme time resolution of ATRS. As theoretical calculations show that the atomic-solid nature is to be found also in valence excitons, these results pave the way for future ATRS experiments which could be directly relevant for technological applications [356].

4. Conclusion and outlook

Despite the impressive progress in the application of attosecond methods, which we have only partially outlined in this Review, the complete exploitation of all potential of this research field still requires key technological advances and new theoretical approaches.

From the technological viewpoint, we can see a few interesting research directions. As we have discussed, the possibility to generate attosecond pulses with high photon energy, in the water window and beyond, may open new perspectives in ultrafast spectroscopy, since this makes it possible to combine extreme temporal (and spatial) resolution with element- and state-specificity of core-level x-ray absorption spectroscopy. This offers the opportunity to investigate electron and nuclear ultrafast dynamics in organic molecules and in materials containing, for example, C, N and O atoms [357]. XUV continua in the water window and beyond are generated by using driving pulses with few-optical-cycle duration, with central wavelength in the mid-infrared spectral region, typically produced by Optical Parametric Amplifiers (OPAs) followed by hollow-fiber compression or by Optical Parametric Chirped-Pulse Amplification (OPCPA) [358–360]. Driven by advances in the generation of high-energy pulses in the near-IR region, notable progress has recently been made in the generation of attosecond pulses in the water window, and various spectroscopic applications have been reported. Since the harmonic generation efficiency scales with the driving wavelength as $\lambda^{-5,-6}$ [37], the generation of attosecond pulses with high photon flux in this spectral region is still a very active research field.

As a matter of fact, the implementation of experimental methods for increasing the XUV photon flux is another key issue in attosecond technology. High-energy, attosecond pulses are crucial, for example, for attosecond-pump/attosecond-probe measurements. Contrary to what happens in the case of attosecond/near-IR-visible pump-probe spectroscopy, where the energy levels of the sample under investigation are strongly distorted, due to the high ponderomotive energy of the intense NIR/visible pulses, in the case of attosecond-pump/attosecond-probe measurements, as a consequence of the very small ponderomotive energy of the XUV pulse, the energy levels and structure of the sample are not distorted. So far, only a few examples of this technique were reported, for example in Xe [35] and H_2 [124]. An alternative and very promising way to produce high-energy pulses is based on X-ray free-electron lasers (FELs), as recently reported at Linac Coherent Light Source (LCLS) [19]. The pulses were generated by an electron bunch modulated by interaction with a high-power IR pulse and compressed in a small magnetic chicane. The advantage of a FEL is the possibility to generate high intensity, high photon energy and short pulse duration, but at the cost of a much more complex experimental apparatus, compare to HHG in gas.

As outlined in this Review, another important tool for attosecond spectroscopy is the polarization control of attosecond pulses [336, 337, 361]. Table-top sources of attosecond pulses with circular polarization are particularly useful for the investigation of ultrafast processes involved in chirality-sensitive light–matter interactions, with crucial applications to magnetic circular dichroism spectroscopy, the investigation of ultrafast dynamics of photoelectron circular dichroism in chiral molecules [362] and for ultrafast imaging of magnetic circular dichroism [337, 338], to cite just a few examples. Various techniques have been proposed and implemented for the generation of high-order harmonics with circular or elliptical polarization. Despite the outstanding and pioneering results obtained so far, the research on the generation of circularly polarised

isolated attosecond pulses is still in its infancy and the applicability of such techniques for the realisation of actual experiments has yet to be fully exploited.

Another hot topic in attosecond science is the extension to the attosecond domain of nonlinear wave-mixing spectroscopic techniques, which are now widely used with femtosecond pulses. These experimental methods are related to the nonlinear dependence of the polarization of a given material on the intensity of the incident electric field [363]. Time resolved four-wave mixing (4WM), transient grating spectroscopy and multidimensional spectroscopy rely on the use of intense coherent pulses: this is the reason why the extension of these spectroscopic techniques towards the XUV or the X-ray regime is not straightforward. The low photon flux of typical attosecond beamlines based on HHG does not allow one to perform XUV-only multidimensional spectroscopy. 4WM has been experimentally demonstrated by employing attosecond pulses in combination with moderately intense femtosecond NIR pulses [364–367]: this represents a very important step towards multidimensional coherent spectroscopy [363]. True multidimensional spectroscopy in the XUV region could be achieved by resolving simultaneously the frequencies of the XUV and of the optical pulses. A further advance will be the extension of attosecond multidimensional spectroscopy to solids or liquids.

In conclusion, in this Review we have seen that the extension to the attosecond domain of spectroscopic techniques originally developed for the femtosecond domain and the introduction of completely new experimental approaches, have made it possible to investigate electronic dynamics in atoms, molecules and solid with an extreme temporal resolution. The measurement of photoemission delays, the excitation and control of electron dynamics in complex molecules before significant motion of nuclei, the first steps towards optical manipulation of carriers in dielectrics in the petahertz regime, are just a few examples that have allowed the attosecond science to be recognized as one of the most significant advances in the field of physics of matter. The combination of new experimental tools with advanced theoretical modeling and numerical simulations, may open the way to the development of new technologies, for example in the field of petahertz electronics or in molecular electronics, where ultrafast electronic processes play a crucial role.

Acknowledgments

We gratefully acknowledge all our collaborators who have contributed immensely to the various experiments and studies reported here. We acknowledge funding from MIUR PRIN, Grant No. 20173B72NB and No. 2017RKWTMY, from the European Research Council under the ERC Grants 951224 (TOMATTO) and 848411 (AuDACE), and from the Fondazione Cariplo.

Data availability statement

No new data were created or analysed in this study.

References

[1] McPherson A, Gibson G, Jara H, Johann U, Luk T S, McIntyre I A, Boyer K and Rhodes C K 1987 *J. Opt. Soc. Am. B* **4** 595–601

[2] Ferray M, LHuillier A, Li X F, Lompre L A, Mainfray G and Manus C 1988 *Journal of Physics B: Atomic, Molecular and Optical Physics* **21** L31–L35

[3] Macklin J J, Kmetec J D and Gordon C L 1993 *Phys. Rev. Lett.* **70**(6) 766–769

[4] L'Huillier A and Balcou P 1993 *Phys. Rev. Lett.* **70**(6) 774–777

[5] Paul P M 2001 *Science* **292** 1689–1692

[6] Hentschel M, Kienberger R, Spielmann C, Reider G A, Milosevic N, Brabec T, Corkum P, Heinzmann U, Drescher M and Krausz F 2001 *Nature* **414** 509–513

[7] Protopapas M, Keitel C H and Knight P L 1997 *Reports on Progress in Physics* **60** 389–486

[8] Corkum P B and Krausz F 2007 *Nature Physics* **3** 381–387

[9] Krausz F and Ivanov M 2009 *Reviews of Modern Physics* **81** 163–234

[10] Sansone G, Poletto L and Nisoli M 2011 *Nature Photonics* **5** 655–663

[11] Nisoli M, Decleva P, Calegari F, Palacios A and Martín F 2017 *Chemical Reviews* **117** 10760–10825 pMID: 28488433

[12] Kraus P M, Zürch M, Cushing S K, Neumark D M and Leone S R 2018 *Nature Reviews Chemistry* **2** 82–94

[13] Schoetz J, Wang Z, Pisanty E, Lewenstein M, Kling M F and Ciappina M F 2019 *ACS Photonics* **6** 3057–3069

[14] Ghimire S and Reis D A 2019 *Nature Physics* **15** 10

[15] Park J, Subramani A, Kim S and Ciappina M F 2022 *Advances in Physics: X* **7** 2003244

[16] Teubner U and Gibbon P 2009 *Rev. Mod. Phys.* **81**(2) 445–479

[17] Thaury C and Quéré F 2010 *Journal of Physics B: Atomic, Molecular and Optical Physics* **43** 213001

[18] Chatziathanasiou S, Kahaly S, Skantzakis E, Sansone G, Lopez-Martens R, Haessler S, Varju K, Tsakiris G D, Charalambidis D and Tzallas P 2017 *Photonics* **4**

[19] Duris J, Li S, Driver T, Champenois E G, MacArthur J P, Lutman A A, Zhang Z, Rosenberger P, Aldrich J W, Coffee R, Coslovich G, Decker F J, Glownia J M, Hartmann G, Helml W, Kamalov A, Knurr J, Krzywinski J, Lin M F, Marangos J P, Nantel M, Natan A, O'Neal J T, Shivaram N, Walter P, Wang A L, Welch J J, Wolf T J A, Xu J Z, Kling M F, Bucksbaum P H, Zholents A, Huang Z, Cryan J P and Marinelli A 2020 *Nature Photonics* **14** 30–36

[20] Brabec T and Krausz F 2000 *Rev. Mod. Phys.* **72**(2) 545–591

[21] Fattahi H, Barros H G, Gorjan M, Nubbemeyer T, Alsaif B, Teisset C Y, Schultze M, Prinz S, Haefner M, Ueffing M, Alismail A, Vámos L, Schwarz A, Pronin O, Brons J, Geng X T, Arisholm G, Ciappina M, Yakovlev V S, Kim D E, Azzeer A M, Karpowicz N, Sutter D, Major Z, Metzger T and Krausz F 2014 *Optica* **1** 45–63

[22] Chang Z 2011 *Fundamentals of Attosecond Optics* (Boca Raton: CRC Press)

[23] Krause J L, Schafer K J and Kulander K C 1992 *Phys. Rev. Lett.* **68**(24) 3535–3538

[24] Kulander K C, Schafer K J and Krause J L 1993 Dynamics of short-pulse excitation, ionization and harmonic conversion *Super-Intense Laser-Atom Phys.* vol 316 ed Piraux B, L'Huillier A and Rzazewski K (New York: Plenum)

[25] Schafer K J, Yang B, DiMauro L F and Kulander K C 1993 *Phys. Rev. Lett.* **70**(11) 1599–1602

[26] Corkum P B 1993 *Phys. Rev. Lett.* **71**(13) 1994–1997

[27] Lewenstein M, Balcou P, Ivanov M Y, L'Huillier A and Corkum P B 1994 *Phys. Rev. A* **49**(3) 2117–2132

[28] Calegari F, Lucchini M, Negro M, Vozzi C, Poletto L, Svelto O, Silvestri S D, Sansone G, Stagira S and Nisoli M 2012 *Journal of Physics B: Atomic, Molecular and Optical Physics* **45** 074002

[29] Calegari F, Sansone G, Stagira S, Vozzi C and Nisoli M 2016 *J. Phys. B: At., Mol. Opt. Phys.: At., Mol. Opt. Phys.* **49** 062001

[30] Tcherbakoff O, Mével E, Descamps D, Plumridge J and Constant E 2003 *Phys. Rev. A* **68**(4) 043804
[31] Sola I, Mével E, Elouga L, Constant E, Strelkov V, Poletto L, Villoresi P, Benedetti E, Caumes J P, Stagira S, Vozzi C, Sansone G and Nisoli M 2006 *Nat. Phys.* **2** 319–322
[32] Sansone G, Benedetti E, Calegari F, Vozzi C, Avaldi L, Flammini R, Poletto L, Villoresi P, Altucci C, Velotta R, Stagira S, Silvestri S D and Nisoli M 2006 *Science* **314** 443–446
[33] Mashiko H, Gilbertson S, Li C, Khan S D, Shakya M M, Moon E and Chang Z 2008 *Phys. Rev. Lett.* **100** 103906
[34] Li J, Lu J, Chew A, Han S, Li J, Wu Y, Wang H, Ghimire S and Chang Z 2020 *Nature Communications* **11** 2748
[35] Tzallas P, Skantzakis E, Nikolopoulos L A A, Tsakiris G D and Charalambidis D 2011 *Nature Physics* **7** 781–784
[36] Takahashi E J, Lan P, Mücke O D and Nabekawa Yasuo nad Midorikawa K 2013 *Nature Communications* **4** 2691
[37] Shiner A D, Trallero-Herrero C, Kajumba N, Bandulet H C, Comtois D, Légaré F, Giguère M, Kieffer J C, Corkum P B and Villeneuve D M 2009 *Phys. Rev. Lett.* **103**(7) 073902
[38] Popmintchev T, Chen M C, Popmintchev D, Arpin P, Brown S, Ališauskas S, Andriukaitis G, Balčiunas T, Mücke O D, Pugzlys A, Baltuška A, Shim B, Schrauth S E, Gaeta A, Hernández-García C, Plaja L, Becker A, Jaron-Becker A, Murnane M M and Kapteyn H C 2012 *Science* **336** 1287–1291
[39] Popmintchev D, Galloway B R, Chen M C, Dollar F, Mancuso C A, Hankla A, Miaja-Avila L, O'Neil G, Shaw J M, Fan G, Ališauskas S, Andriukaitis G, Balčiunas T, Mücke O D, Pugzlys A, Baltuška A, Kapteyn H C, Popmintchev T and Murnane M M 2018 *Phys. Rev. Lett.* **120**(9) 093002
[40] Scrinzi A and Muller H G 2009 Attosecond pulses: Generation, detection, and applications *Strong Field Laser Physics* ed Brabec T (New York, NY: Springer New York) pp 281–300
[41] Orfanos I, Makos I, Liontos I, Skantzakis E, Förg B, Charalambidis D and Tzallas P 2019 *APL Photonics* **4** 080901
[42] Drescher M, Hentschel M, Kienberger R, Uiberacker M, Yakovlev V, Scrinzi A, Westerwalbesloh T T, Kleineberg U, Heinzmann U and Krausz F 2002 *Nature* **419** 803–807 ISSN 0028-0836
[43] Pazourek R, Nagele S and Burgdörfer J 2015 *Reviews of Modern Physics* **87** 765–802
[44] Cavalieri a L, Müller N, Uphues T, Yakovlev V S, Baltuška A, Horvath B, Schmidt B, Blümel L, Holzwarth R, Hendel S, Drescher M, Kleineberg U, Echenique P M, Kienberger R, Krausz F and Heinzmann U 2007 *Nature* **449** 1029–1032
[45] Locher R, Castiglioni L, Lucchini M, Greif M, Gallmann L, Osterwalder J, Hengsberger M and Keller U 2015 *Optica* **2** 405
[46] Neppl S, Ernstorfer R, Cavalieri A L, Lemell C, Wachter G, Magerl E, Bothschafter E M, Jobst M, Hofstetter M, Kleineberg U, Barth J V, Menzel D, Burgdörfer J, Feulner P, Krausz F and Kienberger R 2015 *Nature* **517** 342–346
[47] Lucchini M, Castiglioni L, Kasmi L, Kliuiev P, Ludwig A, Greif M, Osterwalder J, Hengsberger M, Gallmann L and Keller U 2015 *Physical Review Letters* **115** 137401
[48] Tao Z, Chen C, Szilvási T, Keller M, Mavrikakis M, Kapteyn H and Murnane M 2016 *Science* **353** 62–67
[49] Kasmi L, Lucchini M, Castiglioni L, Kliuiev P, Osterwalder J, Hengsberger M, Gallmann L, Krüger P and Keller U 2017 *Optica* **4** 1492
[50] Siek F, Neb S, Bartz P, Hensen M, Strüber C, Fiechter S, Torrent-Sucarrat M, Silkin V M, Krasovskii E E, Kabachnik N M, Fritzsche S, Muiño R D, Echenique P M, Kazansky A K, Müller N, Pfeiffer W and Heinzmann U 2017 *Science* **357** 1274–1277
[51] Seiffert L, Liu Q, Zherebtsov S, Trabattoni A, Rupp P, Castrovilli M C, Galli M, Süßmann F, Wintersperger K, Stierle J, Sansone G, Poletto L, Frassetto F, Halfpap I, Mondes V, Graf C, Rühl E, Krausz F, Nisoli M, Fennel T, Calegari F and Kling M 2017 *Nature Physics* **13** 766–770

[52] Uiberacker M, Uphues T, Schultze M, Verhoef a J, Yakovlev V, Kling M F, Rauschenberger J, Kabachnik N M, Schröder H, Lezius M and et al 2007 *Nature* **446** 627–32

[53] Sansone G, Kelkensberg F, Pérez-Torres J F, Morales F, Kling M F, Siu W, Ghafur O, Johnsson P, Swoboda M, Benedetti E, Ferrari F, Lépine F, Sanz-Vicario J L, Zherebtsov S, Znakovskaya I, Lhuillier A, Ivanov M Y, Nisoli M, Martín F and Vrakking M J 2010 *Nature* **465** 763–766

[54] Calegari F, Ayuso D, Trabattoni A, Belshaw L, Camillis S D, Anumula S, Frassetto F, Poletto L, Palacios A, Decleva P, Greenwood J B, Martín F and Nisoli M 2014 *Science* **346** 336–339

[55] Lara-Astiaso M, Galli M, Trabattoni A, Palacios A, Ayuso D, Frassetto F, Poletto L, De Camillis S, Greenwood J, Decleva P, Tavernelli I, Calegari F, Nisoli M and Martín F 2018 *The Journal of Physical Chemistry Letters* **9** 4570–4577

[56] Goulielmakis E, Loh Z H, Wirth A, Santra R, Rohringer N, Yakovlev V S, Zherebtsov S, Pfeifer T, Azzeer A M, Kling M F, Leone S R and Krausz F 2010 *Nature* **466** 739–743

[57] Wang H, Chini M, Chen S, Zhang C H, He F, Cheng Y, Wu Y, Thumm U and Chang Z 2010 *Phys. Rev. Lett.* **105**(14) 143002

[58] Lucchini M, Sato S A, Lucarelli G D, Moio B, Inzani G, Borrego-Varillas R, Frassetto F, Poletto L, Hübener H, De Giovannini U, Rubio A and Nisoli M 2021 *Nature Communications* **12** 1021

[59] Haessler S, Caillat J and Salières P 2011 *Journal of Physics B: Atomic, Molecular and Optical Physics* **44** 203001

[60] Marangos J P 2016 *Journal of Physics B: Atomic, Molecular and Optical Physics* **49** 132001

[61] Peng P, Marceau C and Villeneuve D M 2019 *Nature Reviews Physics* **1** 144–155

[62] Uehara Y, Ushiroku T, Ushioda S and Murata Y 1990 *Japanese Journal of Applied Physics* **29** 2858–2863

[63] Wiley W C and McLaren I H 1955 *Review of Scientific Instruments* **26** 1150–1157

[64] Kruit P and Read F H 1983 *Journal of Physics E: Scientific Instruments* **16** 313–324

[65] Eppink A T J B and Parker D H 1997 *Review of Scientific Instruments* **68** 3477–3484

[66] Vrakking M J J 2001 *Review of Scientific Instruments* **72** 4084–4089

[67] Ullrich J, Moshammer R, Dorn A, D rner R, Schmidt L P H and Schmidt-B cking H 2003 *Reports on Progress in Physics* **66** 1463–1545

[68] Ullrich J, Moshammer R, Dörner R, Jagutzki O, Mergel V, Schmidt-Böcking H and Spielberger L 1997 *Journal of Physics B: Atomic, Molecular and Optical Physics* **30** 2917–2974

[69] Muller H 2002 *Applied Physics B* **74** s17–s21

[70] Véniard V, Taïeb R and Maquet A 1996 *Physical Review A* **54** 721–728

[71] Mairesse Y 2003 *Science* **302** 1540–1543

[72] Pazourek R, Nagele S and Burgdörfer J 2013 *Faraday Discussions* **163** 353

[73] Wigner E P 1955 *Physical Review* **98** 145–147

[74] Dahlström J M, L'Huillier A and Maquet A 2012 *Journal of Physics B: Atomic, Molecular and Optical Physics* **45** 183001

[75] Constant E, Taranukhin V D, Stolow A and Corkum P B 1997 *Phys. Rev. A* **56**(5) 3870–3878

[76] Itatani J, Quéré F, Yudin G L, Ivanov M Y, Krausz F and Corkum P B 2002 *Physical Review Letters* **88** 173903

[77] Kienberger R, Goulielmakis E, Uiberacker M, Baltuska A, Yakovlev V, Bammer F, Scrinzi A, Westerwalbesloh T, Kleineberg U, Heinzmann U, Drescher M and Krausz F 2004 *Nature* **427** 817–821

[78] Cattaneo L, Vos J, Lucchini M, Gallmann L, Cirelli C and Keller U 2016 *Optics Express* **24** 29060

[79] Kitzler M, Milosevic N, Scrinzi A, Krausz F and Brabec T 2002 *Physical Review Letters* **88** 173904

[80] Trebino R, DeLong K W, Fittinghoff D N, Sweetser J N, Krumbügel M A, Richman B A and Kane D J 1997 *Review of Scientific Instruments* **68** 3277–3295

[81] Mairesse Y and Quéré F 2005 *Physical Review A* **71** 011401

[82] Kane D 1999 *IEEE Journal of Quantum Electronics* **35** 421–431

[83] Gagnon J, Goulielmakis E and Yakovlev V 2008 *Applied Physics B* **92** 25–32

[84] Lucchini M, Brügmann M, Ludwig A, Gallmann L, Keller U and Feurer T 2015 *Optics Express* **23** 29502
[85] Yu W W, Zhao X, Wei H, Wang S J and Lin C D 2019 *Physical Review A* **99** 033403
[86] Zhu Z, White J, Chang Z and Pang S 2020 *Scientific Reports* **10** 5782
[87] Schultze M, Fiess M, Karpowicz N, Gagnon J, Korbman M, Hofstetter M, Neppl S, Cavalieri A L, Komninos Y, Mercouris T, Nicolaides C A, Pazourek R, Nagele S, Feist J, Burgdorfer J, Azzeer A M, Ernstorfer R, Kienberger R, Kleineberg U, Goulielmakis E, Krausz F and Yakovlev V S 2010 *Science* **328** 1658–1662
[88] Klünder K, Dahlström J M, Gisselbrecht M, Fordell T, Swoboda M, Guénot D, Johnsson P, Caillat J, Mauritsson J, Maquet A, Taïeb R and L'Huillier A 2011 *Phys. Rev. Lett.* **106**(14) 143002
[89] Sabbar M, Heuser S, Boge R, Lucchini M, Carette T, Lindroth E, Gallmann L, Cirelli C and Keller U 2015 *Physical Review Letters* **115** 133001
[90] Kaldun A, Blättermann A, Stooß V, Donsa S, Wei H, Pazourek R, Nagele S, Ott C, Lin C D, Burgdörfer J and Pfeifer T 2016 *Science* **354** 738–741
[91] Gruson V, Barreau L, Jiménez-Galan Á, Risoud F, Caillat J, Maquet A, Carré B, Lepetit F, Hergott J F, Ruchon T, Argenti L, Taïeb R, Martín F and Salières P 2016 *Science* **354** 734–738
[92] Cirelli C, Marante C, Heuser S, Petersson C L M, Galán Á J, Argenti L, Zhong S, Busto D, Isinger M, Nandi S, Maclot S, Rading L, Johnsson P, Gisselbrecht M, Lucchini M, Gallmann L, Dahlström J M, Lindroth E, L'Huillier A, Martín F and Keller U 2018 *Nature Communications* **9** 955
[93] Pfeiffer A N, Bell M J, Beck A R, Mashiko H, Neumark D M and Leone S R 2013 *Phys. Rev. A* **88**(5) 051402
[94] Dudovich N, Smirnova O, Levesque J, Mairesse Y, Ivanov M Y, Villeneuve D M and Corkum P B 2006 *Nature Physics* **2** 781–786
[95] Ramasesha K, Leone S R and Neumark D M 2016 *Annual Review of Physical Chemistry* **67** 41–63
[96] Kling M F, Siedschlag C, Verhoef A J, Khan J I, Schultze M, Uphues T, Ni Y, Uiberacker M, Drescher M, Krausz F and Vrakking M J 2006 *Science* ISSN 00368075
[97] Kling M F and Vrakking M J 2008 *Annual Review of Physical Chemistry* **59** 463–492
[98] Gallmann L, Cirelli C and Keller U 2012 *Annual Review of Physical Chemistry* **63** 447–469
[99] Ossiander M, Siegrist F, Shirvanyan V, Pazourek R, Sommer A, Latka T, Guggenmos A, Nagele S, Feist J, Burgdörfer J, Kienberger R and Schultze M 2017 *Nature Physics* **13** 280–285
[100] Sabbar M, Timmers H, Chen Y J, Pymer A K, Loh Z H, Sayres S G, Pabst S, Santra R and Leone S R 2017 *Nature Physics* **13** 472–478
[101] Mauritsson J, Remetter T, Swoboda M, Klünder K, L'Huillier A, Schafer K J, Ghafur O, Kelkensberg F, Siu W, Johnsson P, Vrakking M J J, Znakovskaya I, Uphues T, Zherebtsov S, Kling M F, Lépine F, Benedetti E, Ferrari F, Sansone G and Nisoli M 2010 *Phys. Rev. Lett.* **105**(5) 053001
[102] Lucchini M, Ludwig A, Zimmermann T, Kasmi L, Herrmann J, Scrinzi A, Landsman A S, Gallmann L and Keller U 2015 *Physical Review A* **91** 063406
[103] Remetter T, Johnsson P, Mauritsson J, Varjú K, Ni Y, Lépine F, Gustafsson E, Kling M, Khan J, López-Martens R, Schafer K J, Vrakking M J J and L'Huillier A 2006 *Nature Physics* **2** 323–326
[104] Johnsson P, Mauritsson J, Remetter T, L'Huillier A and Schafer K J 2007 *Phys. Rev. Lett.* **99**(23) 233001
[105] Månsson E P, Guénot D, Arnold C L, Kroon D, Kasper S, Dahlström J M, Lindroth E, Kheifets A S, L'Huillier A, Sorensen S L and Gisselbrecht M 2014 *Nature Physics* **10** 207–211
[106] Heuser S, Jiménez Galán Á, Cirelli C, Marante C, Sabbar M, Boge R, Lucchini M, Gallmann L, Ivanov I, Kheifets A S, Dahlström J M, Lindroth E, Argenti L, Martín F and Keller U 2016 *Physical Review A* **94** 063409

[107] Isinger M, Squibb R J, Busto D, Zhong S, Harth A, Kroon D, Nandi S, Arnold C L, Miranda M, Dahlström J M, Lindroth E, Feifel R, Gisselbrecht M and L'Huillier A 2017 *Science* **358** 893–896

[108] Feist J, Zatsarinny O, Nagele S, Pazourek R, Burgdörfer J, Guan X, Bartschat K and Schneider B I 2014 *Physical Review A* **89** 033417

[109] Moore L R, Lysaght M A, Parker J S, van der Hart H W and Taylor K T 2011 *Physical Review A* **84** 061404

[110] Kheifets A S and Ivanov I A 2010 *Physical Review Letters* **105** 233002

[111] Busto D, Barreau L, Isinger M, Turconi M, Alexandridi C, Harth A, Zhong S, Squibb R J, Kroon D, Plogmaker S, Miranda M, Jiménez-Galán Á, Argenti L, Arnold C L, Feifel R, Martín F, Gisselbrecht M, L'Huillier A and Salières P 2018 *Journal of Physics B: Atomic, Molecular and Optical Physics* **51** 044002

[112] Schoun S B, Chirla R, Wheeler J, Roedig C, Agostini P, DiMauro L F, Schafer K J and Gaarde M B 2014 *Phys. Rev. Lett.* **112**(15) 153001

[113] Alexandridi C, Platzer D, Barreau L, Busto D, Zhong S, Turconi M, Neoričić L, Laurell H, Arnold C L, Borot A, Hergott J F, Tcherbakoff O, Lejman M, Gisselbrecht M, Lindroth E, L'Huillier A, Dahlström J M and Salières P 2021 *Physical Review Research* **3** L012012

[114] Barreau L, Petersson C L M, Klinker M, Camper A, Marante C, Gorman T, Kiesewetter D, Argenti L, Agostini P, González-Vázquez J, Salières P, DiMauro L F and Martín F 2019 *Phys. Rev. Lett.* **122**(25) 253203

[115] Kotur M, Guénot D, Jiménez-Galán Á, Kroon D, Larsen E W, Louisy M, Bengtsson S, Miranda M, Mauritsson J, Arnold C L, Canton S E, Gisselbrecht M, Carette T, Dahlström J M, Lindroth E, Maquet A, Argenti L, Martín F and L'Huillier A 2016 *Nature Communications* **7** 10566

[116] Borrego-Varillas R and Lucchini M 2021 *Opt. Express* **29** 9711–9722

[117] Wickenhauser M, Burgdörfer J, Krausz F and Drescher M 2005 *Phys. Rev. Lett.* **94**(2) 023002

[118] Baykusheva D and Wörner H J 2021 Attosecond Molecular Dynamics and Spectroscopy *Molecular Spectroscopy and Quantum Dynamics* (Elsevier) pp 113–161

[119] Kelkensberg F, Siu W, Pérez-Torres J F, Morales F, Gademann G, Rouzée A, Johnsson P, Lucchini M, Calegari F, Sanz-Vicario J L, Martín F and Vrakking M J 2011 *Physical Review Letters*

[120] Ranitovic P, Hogle C W, Rivière P, Palacios A, Tong X M, Toshima N, González-Castrillo A, Martin L, Martín F, Murnane M M and Kapteyn H 2014 *Proceedings of the National Academy of Sciences of the United States of America*

[121] Cattaneo L, Vos J, Bello R Y, Palacios A, Heuser S, Pedrelli L, Lucchini M, Cirelli C, Martín F and Keller U 2018 *Nature Physics* **14** 733–739

[122] Tzallas P, Skantzakis E, Kalpouzos C, Benis E P, Tsakiris G D and Charalambidis D 2007 *Nature Physics* **3** 846–850

[123] Major B, Ghafur O, Kovács K, Varjú K, Tosa V, Vrakking M J J and Schütte B 2021 *Optica* **8** 960

[124] Carpeggiani P A, Tzallas P, Palacios A, Gray D, Martín F and Charalambidis D 2014 *Phys. Rev. A* **89**(2) 023420

[125] Palacios A, Gonzalez-Castrillo A and Martin F 2014 *Proceedings of the National Academy of Sciences* **111** 3973–3978 ISSN 0027-8424

[126] Nabekawa Y, Furukawa Y, Okino T, Amani Eilanlou A, Takahashi E J, Yamanouchi K and Midorikawa K 2016 *Nature Communications* **7** 12835

[127] González-Castrillo A, Martín F and Palacios A 2020 *Scientific Reports* **10** 12981

[128] Wituschek A, Bruder L, Allaria E, Bangert U, Binz M, Borghes R, Callegari C, Cerullo G, Cinquegrana P, Giannessi L, Danailov M, Demidovich A, Di Fraia M, Drabbels M, Feifel R, Laarmann T, Michiels R, Mirian N S, Mudrich M, Nikolov I, O'Shea F H, Penco G, Piseri P, Plekan O, Prince K C, Przystawik A, Ribič P R, Sansone G, Sigalotti P, Spampinati S, Spezzani C, Squibb R J, Stranges S, Uhl D and Stienkemeier F 2020 *Nature Communications* **11** 1–19

[129] Maroju P K, Grazioli C, Di Fraia M, Moioli M, Ertel D, Ahmadi H, Plekan O, Finetti P, Allaria E, Giannessi L, De Ninno G, Spezzani C, Penco G, Spampinati S, Demidovich A, Danailov M B, Borghes R, Kourousias G, Sanches Dos Reis C E, Billé F, Lutman A A, Squibb R J, Feifel R, Carpeggiani P, Reduzzi M, Mazza T, Meyer M, Bengtsson S, Ibrakovic N, Simpson E R, Mauritsson J, Csizmadia T, Dumergue M, Kühn S, Nandiga Gopalakrishna H, You D, Ueda K, Labeye M, Bækhøj J E, Schafer K J, Gryzlova E V, Grum-Grzhimailo A N, Prince K C, Callegari C and Sansone G 2020 *Nature* **578** 386–391

[130] Gauthier D, Ribič P R, De Ninno G, Allaria E, Cinquegrana P, Danailov M B, Demidovich A, Ferrari E and Giannessi L 2016 *Physical Review Letters* **116** 024801

[131] Siu W, Kelkensberg F, Gademann G, Rouzée A, Johnsson P, Dowek D, Lucchini M, Calegari F, De Giovannini U, Rubio A, Lucchese R R, Kono H, Lépine F and Vrakking M J J 2011 *Physical Review A* **84** 063412

[132] Cörlin P, Fischer A, Schönwald M, Sperl A, Mizuno T, Thumm U, Pfeifer T and Moshammer R 2015 *Physical Review A* **91** 043415

[133] Sandhu A S, Gagnon E, Santra R, Sharma V, Li W, Ho P, Ranitovic P, Cocke C L, Murnane M M and Kapteyn H C 2008 *Science* **322** 1081–1085

[134] Lucchini M, Kim K, Calegari F, Kelkensberg F, Siu W, Sansone G, Vrakking M J J, Hochlaf M and Nisoli M 2012 *Physical Review A* **86** 043404

[135] Haessler S, Fabre B, Higuet J, Caillat J, Ruchon T, Breger P, Carré B, Constant E, Maquet A, Mével E, Salières P, Taïeb R and Mairesse Y 2009 *Physical Review A* **80** 011404

[136] Eckstein M, Yang C H, Kubin M, Frassetto F, Poletto L, Ritze H H, Vrakking M J J and Kornilov O 2015 *The Journal of Physical Chemistry Letters* **6** 419–425

[137] Trabattoni A, Klinker M, González-Vázquez J, Liu C, Sansone G, Linguerri R, Hochlaf M, Klei J, Vrakking M J J, Martín F, Nisoli M and Calegari F 2015 *Physical Review X* **5** 041053

[138] Neidel C, Klei J, Yang C H, Rouzée A, Vrakking M J J, Klünder K, Miranda M, Arnold C L, Fordell T, L'Huillier A, Gisselbrecht M, Johnsson P, Dinh M P, Suraud E, Reinhard P G, Despré V, Marques M A L and Lépine F 2013 *Physical Review Letters* **111** 033001

[139] Huppert M, Jordan I, Baykusheva D, von Conta A and Wörner H J 2016 *Physical Review Letters* **117** 093001

[140] Jordan I, Huppert M, Rattenbacher D, Peper M, Jelovina D, Perry C, von Conta A, Schild A and Wörner H J 2020 *Science* **369** 974–979

[141] Chacon A, Lein M and Ruiz C 2014 *Physical Review A* **89** 053427

[142] Vos J, Cattaneo L, Patchkovskii S, Zimmermann T, Cirelli C, Lucchini M, Kheifets A, Landsman A S and Keller U 2018 *Science* **360** 1326–1330

[143] Spanner M and Patchkovskii S 2009 *Physical Review A* **80** 063411

[144] Biswas S, Förg B, Ortmann L, Schötz J, Schweinberger W, Zimmermann T, Pi L, Baykusheva D, Masood H A, Liontos I, Kamal A M, Kling N G, Alharbi A F, Alharbi M, Azzeer A M, Hartmann G, Wörner H J, Landsman A S and Kling M F 2020 *Nature Physics* **16** 778–783

[145] Zewail A H 2000 *The Journal of Physical Chemistry A* **104** 5660–5694

[146] De Silvestri S, Manzoni C, Borrego-Varillas R, Oriana A and Cerullo G 2018 *Rivista del Nuovo Cimento* **41** 1–70

[147] Berera R, van Grondelle R and Kennis J T M 2009 *Photosynthesis Research* **101** 105–118

[148] Scholes G D, Fleming G R, Olaya-Castro A and van Grondelle R 2011 *Nature Chemistry* **3** 763–774

[149] de la Cruz Valbuena G, V A Camargo F, Borrego-Varillas R, Perozeni F, D'Andrea C, Ballottari M and Cerullo G 2019 *The Journal of Physical Chemistry Letters* **10** 2500–2505

[150] Middleton C T, de La Harpe K, Su C, Law Y K, Crespo-Hernández C E and Kohler B 2009 *Annual Review of Physical Chemistry* **60** 217–239

[151] Borrego-Varillas R, Teles-Ferreira D C, Nenov A, Conti I, Ganzer L, Manzoni C, Garavelli M, Maria de Paula A and Cerullo G 2018 *Journal of the American Chemical Society* **140** 16087–16093

[152] Borrego-Varillas R, Cerullo G and Markovitsi D 2019 *The Journal of Physical Chemistry Letters* **10** 1639–1643

[153] Teles-Ferreira D C, Conti I, Borrego-Varillas R, Nenov A, Van Stokkum I H M, Ganzer L, Manzoni C, Paula A M, Cerullo G and Garavelli M 2020 *Chemistry – A European Journal* **26** 336–343

[154] Pecourt J M L, Peon J and Kohler B 2000 *Journal of the American Chemical Society* **122** 9348–9349

[155] Ikeura-Sekiguchi H and Sekiguchi T 2007 *Physical Review Letters* **99** 228102

[156] Cederbaum L and Zobeley J 1999 *Chemical Physics Letters* **307** 205–210

[157] Wörner H J, Arrell C A, Banerji N, Cannizzo A, Chergui M, Das A K, Hamm P, Keller U, Kraus P M, Liberatore E, Lopez-Tarifa P, Lucchini M, Meuwly M, Milne C, Moser J E, Rothlisberger U, Smolentsev G, Teuscher J, Van Bokhoven J A and Wenger O 2017 *Structural Dynamics* **4**

[158] Weinkauf R, Schanen P, Yang D, Soukara S and Schlag E W 1995 *The Journal of Physical Chemistry* **99** 11255–11265

[159] Weinkauf R, Schlag E W, Martinez T J and Levine R D 1997 *The Journal of Physical Chemistry A* **101** 7702–7710

[160] Weinkauf R, Schanen P, Metsala A, Schlag E W, Burgle M and Kessler H 1996 *J. Phys. Chem.* **100** 18567–18585

[161] Hennig H, Breidbach J and Cederbaum L S 2005 *The Journal of Chemical Physics* **122** 134104

[162] Breidbach J and Cederbaum L S 2003 *The Journal of Chemical Physics* **118** 3983–3996

[163] Breidbach J and Cederbaum L S 2005 *Physical Review Letters* **94** 033901

[164] Remacle F and Levine R D 2006 *Proceedings of the National Academy of Sciences of the United States of America* **103** 6793–6798

[165] Mignolet B, Levine R D and Remacle F 2014 *Journal of Physics B: Atomic, Molecular and Optical Physics* **47**

[166] Lehr L, Horneff T, Weinkauf R and Schlag E W 2005 *The Journal of Physical Chemistry A* **109** 8074–8080

[167] Cheng W, Kuthirummal N, Gosselin J L, Sølling T I, Weinkauf R and Weber P M 2005 *The Journal of Physical Chemistry A* **109** 1920–1925

[168] Belshaw L, Calegari F, Duffy M J, Trabattoni A, Poletto L, Nisoli M and Greenwood J B 2012 *The Journal of Physical Chemistry Letters* **3** 3751–3754

[169] Kraus P M, Mignolet B, Baykusheva D, Rupenyan A, Horný L, Penka E F, Grassi G, Tolstikhin O I, Schneider J, Jensen F, Madsen L B, Bandrauk A D, Remacle F and Wörner H J 2015 *Science* **350** 790–795

[170] Perfetto E, Trabattoni A, Calegari F, Nisoli M, Marini A and Stefanucci G 2020 *The Journal of Physical Chemistry Letters* **11** 891–899

[171] Castrovilli M C, Trabattoni A, Bolognesi P, O'Keeffe P, Avaldi L, Nisoli M, Calegari F and Cireasa R 2018 *The Journal of Physical Chemistry Letters* **9** 6012–6016

[172] Månsson E P, De Camillis S, Castrovilli M C, Galli M, Nisoli M, Calegari F and Greenwood J B 2017 *Physical Chemistry Chemical Physics* **19** 19815–19821

[173] Månsson E P, Latini S, Covito F, Wanie V, Galli M, Perfetto E, Stefanucci G, Hübener H, De Giovannini U, Castrovilli M C, Trabattoni A, Frassetto F, Poletto L, Greenwood J B, Légaré F, Nisoli M, Rubio A and Calegari F 2021 *Communications Chemistry* **4** 73

[174] Zipp L J, Natan A and Bucksbaum P H 2014 *Optica* **1** 361–364

[175] Song X, Shi G, Zhang G, Xu J, Lin C, Chen J and Yang W 2018 *Phys. Rev. Lett.* **121**(10) 103201

[176] Beaulieu S, Comby A, Clergerie A, Caillat J, Descamps D, Dudovich N, Fabre B, Géneaux R, Légaré F, Petit S, Pons B, Porat G, Ruchon T, Taïeb R, Blanchet V and Mairesse Y 2017 *Science* **358** 1288–1294

[177] Hertz H 1887 *Annalen der Physik* **267** 983–1000

[178] Reinert F and Hüfner S 2005 *New Journal of Physics* **7** 97–97

[179] Shen Z X and Dessau D 1995 *Physics Reports* **253** 1–162

[180] Damascelli A, Hussain Z and Shen Z X 2003 *Rev. Mod. Phys.* **75**(2) 473–541

[181] Hüfner S 2003 *Photoelectron Spectroscopy* Advanced Texts in Physics (Berlin, Heidelberg: Springer Berlin Heidelberg)
[182] Farkas G and Tóth C 1992 *Physics Letters A* **168** 447–450
[183] Rundquist A, Durfee C G, Chang Z, Herne C, Backus S, Murnane M M and Kapteyn H C 1998 *Science* **280** 1412–1415
[184] Spielmann C, Burnett N H, Sartania S, Koppitsch R, Schnürer M, Kan C, Lenzner M, Wobrauschek P and Krausz F 1997 *Science* **278** 661–664
[185] Mathias S, Wiesenmayer M, Deicke F, Ruffing A, Miaja-Avila L, Murnane M M, Kapteyn H C, Bauer M and Aeschlimann M 2009 *Journal of Physics: Conference Series* **148** 012042
[186] Poletto L, Villoresi P, Frassetto F, Calegari F, Ferrari F, Lucchini M, Sansone G and Nisoli M 2009 *Review of Scientific Instruments* **80** 123109
[187] Frassetto F, Cacho C, Froud C a, Turcu I E, Villoresi P, Bryan W a, Springate E and Poletto L 2011 *Optics Express* **19** 19169
[188] Lucchini M, Lucarelli G D, Murari M, Trabattoni A, Fabris N, Frassetto F, De Silvestri S, Poletto L and Nisoli M 2018 *Optics Express* **26** 6771
[189] Haight R 1995 *Surface Science Reports* **21** 275–325
[190] Quéré F, Guizard S, Martin P, Petite G, Merdji H, Carré B, Hergott J F and Le Déroff L 2000 *Phys. Rev. B* **61**(15) 9883–9886
[191] Miaja-Avila L, Saathoff G, Mathias S, Yin J, La-o vorakiat C, Bauer M, Aeschlimann M, Murnane M M and Kapteyn H C 2008 *Phys. Rev. Lett.* **101**(4) 046101
[192] Read K, Karlsson H S, Murnane M M, Kapteyn H C and Haight R 2001 *Journal of Applied Physics* **90** 294–300
[193] Siffalovic P, Drescher M, Spieweck M, Wiesenthal T, Lim Y C, Weidner R, Elizarov A and Heinzmann U 2001 *Review of Scientific Instruments* **72** 30–35
[194] Melzer A, Kampa D, Wang J and Fauster T 2009 *Phys. Rev. B* **80**(20) 205424
[195] Rohwer T, Hellmann S, Wiesenmayer M, Sohrt C, Stange A, Slomski B, Carr A, Liu Y, Avila L M, Kalläne M, Mathias S, Kipp L, Rossnagel K and Bauer M 2011 *Nature* **471** 490–493
[196] Petersen J C, Kaiser S, Dean N, Simoncig A, Liu H Y, Cavalieri A L, Cacho C, Turcu I C E, Springate E, Frassetto F, Poletto L, Dhesi S S, Berger H and Cavalleri A 2011 *Phys. Rev. Lett.* **107**(17) 177402
[197] Hellmann S, Rohwer T, Kalläne M, Hanff K, Sohrt C, Stange A, Carr A, Murnane M, Kapteyn H, Kipp L, Bauer M and Rossnagel K 2012 *Nature Communications* **3** 1069
[198] Carley R, Döbrich K, Frietsch B, Gahl C, Teichmann M, Schwarzkopf O, Wernet P and Weinelt M 2012 *Phys. Rev. Lett.* **109**(5) 057401
[199] Dakovski G L, Li Y, Gilbertson S M, Rodriguez G, Balatsky A V, Zhu J X, Gofryk K, Bauer E D, Tobash P H, Taylor A, Sarrao J L, Oppeneer P M, Riseborough P S, Mydosh J A and Durakiewicz T 2011 *Phys. Rev. B* **84**(16) 161103
[200] Gierz I, Petersen J C, Mitrano M, Cacho C, Turcu I C E, Springate E, Stöhr A, Köhler A, Starke U and Cavalleri A 2013 *Nature Materials* **12** 1119–1124
[201] Gierz I, Calegari F, Aeschlimann S, Chávez Cervantes M, Cacho C, Chapman R T, Springate E, Link S, Starke U, Ast C R and Cavalleri A 2015 *Physical Review Letters* **115** 086803
[202] Borisov A, Sánchez-Portal D, Dıéz Muiño R and Echenique P 2004 *Chemical Physics Letters* **387** 95–100
[203] Kazansky A K and Echenique P M 2009 *Physical Review Letters* **102** 177401
[204] Zhang C H and Thumm U 2009 *Physical Review Letters* **102** 123601
[205] Kazansky A K and Echenique P M 2010 *Phys. Rev. B* **81**(19) 193413
[206] Zhang C H and Thumm U 2011 *Physical Review A* **84** 063403
[207] Föhlisch a, Feulner P, Hennies F, Fink A, Menzel D, Sanchez-Portal D, Echenique P M and Wurth W 2005 *Nature* **436** 373–376
[208] Neppl S, Ernstorfer R, Bothschafter E M, Cavalieri A L, Menzel D, Barth J V, Krausz F, Kienberger R and Feulner P 2012 *Physical Review Letters* **109** 087401

[209] Cavalieri A L, Krausz F, Ernstorfer R, Kienberger R, Feulner P, Barth J V and Menzel D 2010 Attosecond Time-Resolved Spectroscopy at Surfaces *Dynamics at Solid State Surfaces and Interfaces* vol 1 (Weinheim, Germany: Wiley-VCH Verlag GmbH & Co. KGaA) pp 537–553
[210] Bothschafter E, Neppl S and Kienberger R 2013 Few-femtosecond and attosecond electron dynamics at surfaces *Progress in Ultrafast Intense Laser Science* vol 9 ed Yamanouchi K and Katsumi M (Berlin Heidelberg: Springer Verlag)
[211] Heinzmann U 2013 Attosecond Time-Resolved Photoemission Spectroscopy in Condensed Matter—Photoelectron Wave Phase Shifts and Time Delays *Springer Series in Optical Sciences* vol 177 (Springer Verlag) pp 231–253
[212] Thumm U, Liao Q, Bothschafter E M, Süßmann F, Kling M F and Kienberger R 2015 Attosecond Physics: Attosecond Streaking Spectroscopy of Atoms and Solids *Photonics* vol 1 (Hoboken, NJ, USA: John Wiley & Sons, Inc.) pp 387–441
[213] Banfi F, Giannetti C, Ferrini G, Galimberti G, Pagliara S, Fausti D and Parmigiani F 2005 *Physical Review Letters* **94** 037601
[214] Krasovskii E E, Schattke W, Jiříček P, Vondráček M, Krasovska O V, Antonov V N, Shpak A P and Bartoš I 2008 *Phys. Rev. B* **78**(16) 165406
[215] Kuzian R O and Krasovskii E E 2020 *Phys. Rev. B* **102**(11) 115116
[216] Baggesen J C and Madsen L B 2009 *Phys. Rev. A* **80**(3) 030901
[217] Krasovskii E E 2011 *Phys. Rev. B* **84**(19) 195106
[218] Lemell C, Solleder B, Tőkési K and Burgdörfer J 2009 *Phys. Rev. A* **79**(6) 062901
[219] Okell W A, Witting T, Fabris D, Arrell C A, Hengster J, Ibrahimkutty S, Seiler A, Barthelmess M, Stankov S, Lei D Y, Sonnefraud Y, Rahmani M, Uphues T, Maier S A, Marangos J P and Tisch J W G 2015 *Optica* **2** 383
[220] Liu Q, Seiffert L, Trabattoni A, Castrovilli M C, Galli M, Rupp P, Frassetto F, Poletto L, Nisoli M, Rühl E, Krausz F, Fennel T, Zherebtsov S, Calegari F and Kling M F 2018 *Journal of Optics* **20** 024002
[221] Lemell C, Neppl S, Wachter G, Tőkési K, Ernstorfer R, Feulner P, Kienberger R and Burgdörfer J 2015 *Physical Review B* **91** 241101
[222] Riemensberger J, Neppl S, Potamianos D, Schäffer M, Schnitzenbaumer M, Ossiander M, Schröder C, Guggenmos A, Kleineberg U, Menzel D, Allegretti F, Barth J V, Kienberger R, Feulner P, Borisov A G, Echenique P M and Kazansky A K 2019 *Phys. Rev. Lett.* **123**(17) 176801
[223] Gebauer A, Neb S, Enns W, Stadtmüller B, Aeschlimann M and Pfeiffer W 2019 *Applied Sciences* **9**
[224] Sato S A, Hübener H, Rubio A and De Giovannini U 2018 *The European Physical Journal B* **91** 126
[225] Locher R 2013 *Attosecond photoemission dynamics from noble metal surfaces* Ph.D. thesis ETH-Zürich
[226] Seah M P and Dench W A 1979 *Surface and Interface Analysis* **1** 2–11
[227] Ossiander M, Riemensberger J, Neppl S, Mittermair M, Schäffer M, Duensing A, Wagner M S, Heider R, Wurzer M, Gerl M, Schnitzenbaumer M, Barth J V, Libisch F, Lemell C, Burgdörfer J, Feulner P and Kienberger R 2018 *Nature* **561** 374–377
[228] Locher R, Lucchini M, Herrmann J, Sabbar M, Weger M, Ludwig A, Castiglioni L, Greif M, Hengsberger M, Gallmann L and Keller U 2014 *Review of Scientific Instruments* **85** 1–9
[229] Borisov a G, Sánchez-Portal D, Kazansky a K and Echenique P M 2013 *Physical Review B* **87** 121110
[230] Ambrosio M J and Thumm U 2018 *Phys. Rev. A* **97**(4) 043431
[231] Chen C, Tao Z, Carr A, Matyba P, Szilvási T, Emmerich S, Piecuch M, Keller M, Zusin D, Eich S, Rollinger M, You W, Mathias S, Thumm U, Mavrikakis M, Aeschlimann M, Oppeneer P M, Kapteyn H and Murnane M 2017 *Proceedings of the National Academy of Sciences* **114** E5300–E5307
[232] Gertsvolf M, Spanner M, Rayner D M and Corkum P B 2010 *Journal of Physics B: Atomic,*

Molecular and Optical Physics **43** 131002
[233] Ambrosio M J and Thumm U 2019 *Phys. Rev. A* **100**(4) 043412
[234] Heinrich S, Saule T, Högner M, Cui Y, Yakovlev V S, Pupeza I and Kleineberg U 2021 *Nature Communications* **12** 3404
[235] Liao Q, Cao W, Zhang Q, Liu K, Wang F, Lu P and Thumm U 2020 *Phys. Rev. Lett.* **125**(4) 043201
[236] Bovensiepen U, Declair S, Lisowski M, Loukakos P A, Hotzel A, Richter M, Knorr A and Wolf M 2009 *Physical Review B* **79** 045415
[237] Lucchini M, Ludwig A, Kasmi L, Gallmann L and Keller U 2015 *Optics Express* **23** 8867
[238] Bourke J D and Chantler C T 2010 *Physical Review Letters* **104** 206601
[239] Tanuma S, Powell C J and Penn D R 2011 *Surface and Interface Analysis* **43** 689–713
[240] Ambrosio M J and Thumm U 2017 *Phys. Rev. A* **96**(5) 051403
[241] Ambrosio M J and Thumm U 2016 *Phys. Rev. A* **94**(6) 063424
[242] Attaccalite C, Grüning M and Marini A 2011 *Phys. Rev. B* **84**(24) 245110
[243] Perfetto E, Pavlyukh Y and Stefanucci G 2022 *Phys. Rev. Lett.* **128**(1) 016801
[244] Gallmann L, Herrmann J, Locher R, Sabbar M, Ludwig A, Lucchini M and Keller U 2013 *Molecular Physics* **111** 2243–2250
[245] Beck A R, Neumark D M and Leone S R 2015 *Chemical Physics Letters* **624** 119–130
[246] Neville S P, Averbukh V, Patchkovskii S, Ruberti M, Yun R, Chergui M, Stolow A and Schuurman M S 2016 *Faraday Discuss.* **194**(0) 117–145
[247] Geneaux R, Marroux H J B, Guggenmos A, Neumark D M and Leone S R 2019 *Philosophical Transactions of the Royal Society A: Mathematical, Physical and Engineering Sciences* **377** 20170463
[248] Schultze M, Bothschafter E M, Sommer A, Holzner S, Schweinberger W, Fiess M, Hofstetter M, Kienberger R, Apalkov V, Yakovlev V S, Stockman M I and Krausz F 2013 *Nature* **493** 75–78
[249] Gaarde M B, Buth C, Tate J L and Schafer K J 2011 *Phys. Rev. A* **83**(1) 013419
[250] Chen S, Bell M J, Beck A R, Mashiko H, Wu M, Pfeiffer A N, Gaarde M B, Neumark D M, Leone S R and Schafer K J 2012 *Phys. Rev. A* **86**(6) 063408
[251] Wu M, Chen S, Camp S, Schafer K J and Gaarde M B 2016 *Journal of Physics B: Atomic, Molecular and Optical Physics* **49** 062003
[252] Gaarde M B, Tate J L and Schafer K J 2008 *Journal of Physics B: Atomic, Molecular and Optical Physics* **41** 132001
[253] Holler M, Schapper F, Gallmann L and Keller U 2011 *Phys. Rev. Lett.* **106**(12) 123601
[254] Fano U 1935 *Nuovo Cimento* **12** 154
[255] Fano U 1961 *Phys. Rev.* **124**(6) 1866–1878
[256] Bernhardt B, Beck A R, Li X, Warrick E R, Bell M J, Haxton D J, McCurdy C W, Neumark D M and Leone S R 2014 *Phys. Rev. A* **89**(2) 023408
[257] Chini M, Wang X, Cheng Y and Chang Z 2014 *Journal of Physics B: Atomic, Molecular and Optical Physics* **47** 124009
[258] Cao W, Warrick E R, Neumark D M and Leone S R 2016 *New Journal of Physics* **18** 013041
[259] Beck A R, Bernhardt B, Warrick E R, Wu M, Chen S, Gaarde M B, Schafer K J, Neumark D M and Leone S R 2014 *New Journal of Physics* **16** 113016
[260] Wang X, Chini M, Cheng Y, Wu Y, Tong X M and Chang Z 2013 *Phys. Rev. A* **87**(6) 063413
[261] Lucchini M, Herrmann J, Ludwig A, Locher R, Sabbar M, Gallmann L and Keller U 2013 *New Journal of Physics* **15** 103010
[262] Chini M, Wang X, Cheng Y, Wu Y, Zhao D, Telnov D a, Chu S I and Chang Z 2013 *Scientific Reports* **3** 1105
[263] Chini M, Zhao B, Wang H, Cheng Y, Hu S X and Chang Z 2012 *Phys. Rev. Lett.* **109**(7) 073601
[264] Herrmann J, Lucchini M, Chen S, Wu M, Ludwig A, Kasmi L, Schafer K J, Gallmann L, Gaarde M B and Keller U 2015 *New Journal of Physics* **17** 013007
[265] Ludwig A, Liberatore E, Herrmann J, Kasmi L, López-Tarifa P, Gallmann L, Rothlisberger U,

Keller U and Lucchini M 2016 *The Journal of Physical Chemistry Letters* **7** 1901–1906
[266] Herrmann J, Weger M, Locher R, Sabbar M, Rivière P, Saalmann U, Rost J M, Gallmann L and Keller U 2013 *Phys. Rev. A* **88**(4) 043843
[267] Simpson E R, Sanchez-Gonzalez A, Austin D R, Diveki Z, Hutchinson S E E, Siegel T, Ruberti M, Averbukh V, Miseikis L, Strüber C S, Chipperfield L and Marangos J P 2016 *New Journal of Physics* **18** 083032
[268] Reduzzi M, Hummert J, Dubrouil A, Calegari F, Nisoli M, Frassetto F, Poletto L, Chen S, Wu M, Gaarde M B, Schafer K and Sansone G 2015 *Phys. Rev. A* **92**(3) 033408
[269] Liao C T, Sandhu A, Camp S, Schafer K J and Gaarde M B 2015 *Phys. Rev. Lett.* **114**(14) 143002
[270] Ott C, Kaldun A, Raith P, Meyer K, Laux M, Evers J, Keitel C H, Greene C H and Pfeifer T 2013 *Science* **340** 716–720
[271] Ott C, Kaldun A, Argenti L, Raith P, Meyer K, Laux M, Zhang Y, Blättermann A, Hagstotz S, Ding T and et al 2014 *Nature* **516** 374–378
[272] Cheng Y, Chini M, Wang X, González-Castrillo A, Palacios A, Argenti L, Martín F and Chang Z 2016 *Phys. Rev. A* **94**(2) 023403
[273] Reduzzi M, Chu W C, Feng C, Dubrouil A, Hummert J, Calegari F, Frassetto F, Poletto L, Kornilov O, Nisoli M, Lin C D and Sansone G 2016 *Journal of Physics B: Atomic, Molecular and Optical Physics* **49** 065102
[274] Warrick E R, Cao W, Neumark D M and Leone S R 2016 *The Journal of Physical Chemistry A* **120** 3165–3174
[275] Warrick E R, Bækhøj J E, Cao W, Fidler A P, Jensen F, Madsen L B, Leone S R and Neumark D M 2017 *Chemical Physics Letters* **683** 408–415
[276] Bominaar J, Schoemaecker C, Dam N, Ter Meulen J and Groenenboom G 2007 *Chemical Physics Letters* **435** 242–246
[277] Drescher L, Reitsma G, Witting T, Patchkovskii S, Mikosch J and Vrakking M J J 2019 *The Journal of Physical Chemistry Letters* **10** 265–269
[278] Ryland E S, Lin M F, Verkamp M A, Zhang K, Benke K, Carlson M and Vura-Weis J 2018 *Journal of the American Chemical Society* **140** 4691–4696
[279] Stolow A and Underwood J G 2008 Time-resolved photoelectron spectroscopy of nonadiabatic dynamics in polyatomic molecules *Advances in Chemical Physics* vol 139 ed Rice S A (John Wiley and Sons)
[280] Domcke W, Yarkony D R and Köppel H 2004 *Conical Intersections* (World Scientific)
[281] Lépine F, Ivanov M Y and Vrakking M J J 2014 *Nature Photonics* **8** 195–204
[282] Kobayashi Y, Chang K F, Zeng T, Neumark D M and Leone S R 2019 *Science* **365** 79–83
[283] Timmers H, Zhu X, Li Z, Kobayashi Y, Sabbar M, Hollstein M, Reduzzi M, Martínez T J, Neumark D M and Leone S R 2019 *Nature Communications* **10** 3133
[284] Chang K F, Reduzzi M, Wang H, Poullain S, Kobayashi Y, Barreau L, Prendergast D, Neumark D M and Leone S R 2020 *Nature Communications* **11** 4042
[285] Child M S and Bernstein R B 1973 *The Journal of Chemical Physics* **59** 5916–5925
[286] Locht R, Leyh B, Dehareng D, Jochims H and Baumgärtel H 2005 *Chemical Physics* **317** 87–102
[287] Pertot Y, Schmidt C, Matthews M, Chauvet A, Huppert M, Svoboda V, von Conta A, Tehlar A, Baykusheva D, Wolf J P and Wörner H J 2017 *Science* **355** 264–267
[288] Attar A R, Bhattacherjee A, Pemmaraju C D, Schnorr K, Closser K D, Prendergast D and Leone S R 2017 *Science* **356** 54–59
[289] Bhattacherjee A, Pemmaraju C D, Schnorr K, Attar A R and Leone S R 2017 *Journal of the American Chemical Society* **139** 16576–16583
[290] Saito N, Sannohe H, Ishii N, Kanai T, Kosugi N, Wu Y, Chew A, Han S, Chang Z and Itatani J 2019 *Optica* **6** 1542–1546
[291] Ho W C, Ozier I, Cramb D T and Gerry M C L 1991 *J. Mol. Spectrosc.* **149** 559–561
[292] Kleine C, Ekimova M, Goldsztejn G, Raabe S, Strüber C, Ludwig J, Yarlagadda S, Eisebitt S, Vrakking M J J, Elsaesser T, Nibbering E T J and Rouzée A 2019 *The Journal of Physical*

Chemistry Letters **10** 52–58
[293] Zinchenko K S, Ardana-Lamas F, Seidu I, Neville S P, van der Veen J, Lanfaloni V U, Schuurman M S and Wörner H J 2021 *Science* **371** 489–494
[294] Borja L J, Zürch M, Pemmaraju C D, Schultze M, Ramasesha K, Gandman A, Prell J S, Prendergast D, Neumark D M and Leone S R 2016 *Journal of the Optical Society of America B* **33** C57
[295] Krausz F and Stockman M I 2014 *Nature Photonics* **8** 205–213
[296] Buades B, Moonshiram D, Sidiropoulos T P H, León I, Schmidt P, Pi I, Di Palo N, Cousin S L, Picón A, Koppens F and Biegert J 2018 *Optica* **5** 502
[297] Thompson, A C and Vaughan D (ed) 2009 *X-ray Data Booklet* ed. 3 ed (Lawrence Berkeley National Laboratory, University of California)
[298] Vura-Weis J, Jiang C M, Liu C, Gao H, Lucas J M, de Groot F M F, Yang P, Alivisatos A P and Leone S R 2013 *The Journal of Physical Chemistry Letters* **4** 3667–3671
[299] Jiang C M, Baker L R, Lucas J M, Vura-Weis J, Alivisatos A P and Leone S R 2014 *The Journal of Physical Chemistry C* **118** 22774–22784
[300] Zürch M, Chang H t, Borja L J, Kraus P M, Cushing S K, Gandman A, Kaplan C J, Oh M H, Prell J S, Prendergast D, Pemmaraju C D, Neumark D M and Leone S R 2017 *Nature Communications* **8** 15734
[301] Cushing S K, Zürch M, Kraus P M, Carneiro L M, Lee A, Chang H T, Kaplan C J and Leone S R 2018 *Structural Dynamics* **5** 054302
[302] Zürch M, Chang H T, Kraus P M, Cushing S K, Borja L J, Gandman A, Kaplan C J, Oh M H, Prell J S, Prendergast D, Pemmaraju C D, Neumark D M and Leone S R 2017 *Structural Dynamics* **4** 044029
[303] Weisshaupt J, Rouzée A, Woerner M, Vrakking M J J, Elsaesser T, Shirley E L and Borgschulte A 2017 *Phys. Rev. B* **95** 081101
[304] Carneiro L M, Cushing S K, Liu C, Su Y, Yang P, Alivisatos A P and Leone S R 2017 *Nature Materials* **16** 819–825
[305] Attar A R, Chang H T, Britz A, Zhang X, Lin M F, Krishnamoorthy A, Linker T, Fritz D, Neumark D M, Kalia R K, Nakano A, Ajayan P, Vashishta P, Bergmann U and Leone S R 2020 *ACS Nano* **14** 15829–15840
[306] Imada M, Fujimori A and Tokura Y 1998 *Reviews of Modern Physics* **70** 1039–1263
[307] Jager M F, Ott C, Kraus P M, Kaplan C J, Pouse W, Marvel R E, Haglund R F, Neumark D M and Leone S R 2017 *Proceedings of the National Academy of Sciences* **114** 9558–9563
[308] Kübler C, Ehrke H, Huber R, Lopez R, Halabica A, Haglund R F and Leitenstorfer A 2007 *Phys. Rev. Lett.* **99**(11) 116401
[309] Britz A, Attar A R, Zhang X, Chang H T, Nyby C, Krishnamoorthy A, Park S H, Kwon S, Kim M, Nordlund D, Sainio S, Heinz T F, Leone S R, Lindenberg A M, Nakano A, Ajayan P, Vashishta P, Fritz D, Lin M F and Bergmann U 2021 *Structural Dynamics* **8** 014501
[310] Buades B, Picón A, Berger E, León I, Di Palo N, Cousin S L, Cocchi C, Pellegrin E, Martin J H, Mañas-Valero S, Coronado E, Danz T, Draxl C, Uemoto M, Yabana K, Schultze M, Wall S, Zürch M and Biegert J 2021 *Applied Physics Reviews* **8** 011408
[311] Schultze M, Bothschafter E M, Sommer A, Holzner S, Schweinberger W, Fiess M, Hofstetter M, Kienberger R, Apalkov V, Yakovlev V S, Stockman M I and Krausz F 2013 *Nature* **493** 75–78
[312] Schultze M, Ramasesha K, Pemmaraju C D, Sato S A, Whitmore D, Gandman A, Prell J S, Borja L J, Prendergast D, Yabana K, Neumark D M and Leone S R 2014 *Science* **346** 1348–1352
[313] Schmidt C, Bühler J, Heinrich A C, Allerbeck J, Podzimski R, Berghoff D, Meier T, Schmidt W G, Reichl C, Wegscheider W, Brida D and Leitenstorfer A 2018 *Nature Communications* **9** 2890
[314] Moulet A, Bertrand J B, Klostermann T, Guggenmos A, Karpowicz N and Goulielmakis E 2017 *Science* **357** 1134–1138
[315] Kruchinin S Y, Krausz F and Yakovlev V S 2018 *Reviews of Modern Physics* **90** 21002

[316] Sato S A, Lucchini M, Volkov M, Schlaepfer F, Gallmann L, Keller U and Rubio A 2018 *Physical Review B* **98** 035202

[317] Sato S A 2021 *Computational Materials Science* **194** 110274

[318] Keldysh L V 1965 *Sovietic Physics JETP* **20**(5) 1307–1314

[319] Hu C C 2009 *Modern Semiconductor Devices for Integrated Circuits* (London: Pearson Education)

[320] Mashiko H, Oguri K, Yamaguchi T, Suda A and Gotoh H 2016 *Nature Physics* **12** 741–745

[321] Mashiko H, Chisuga Y, Katayama I, Oguri K, Masuda H, Takeda J and Gotoh H 2018 *Nature Communications* **9** 1468

[322] Kraut E A, Grant R W, Waldrop J R and Kowalczyk S P 1980 *Phys. Rev. Lett.* **44**(24) 1620–1623

[323] Schlaepfer F, Lucchini M, Sato S A, Volkov M, Kasmi L, Hartmann N, Rubio A, Gallmann L and Keller U 2018 *Nature Physics* **14** 560–564

[324] Vampa G, Hammond T J, Thiré N, Schmidt B E, Légaré F, McDonald C R, Brabec T and Corkum P B 2015 *Nature* **522** 462–464

[325] Luu T T, Garg M, Kruchinin S Y, Moulet A, Hassan M T and Goulielmakis E 2015 *Nature* **521** 498–502

[326] Otobe T, Shinohara Y, Sato S A and Yabana K 2016 *Phys. Rev. B* **93**(4) 045124

[327] Yu P Y and Cardona M 2010 *Fundamentals of Semicondutors* ed. 4 ed (Springer)

[328] Jauho A P and Johnsen K 1996 *Physical Review Letters* **76** 4576–4579

[329] Novelli F, Fausti D, Giusti F, Parmigiani F and Hoffmann M 2013 *Scientific Reports* **3** 1227

[330] Uchida K, Otobe T, Mochizuki T, Kim C, Yoshita M, Akiyama H, Pfeiffer L N, West K W, Tanaka K and Hirori H 2016 *Physical Review Letters* **117** 277402

[331] Lucchini M, Sato S A, Ludwig A, Herrmann J, Volkov M, Kasmi L, Shinohara Y, Yabana K, Gallmann L and Keller U 2016 *Science* **353** 916–919

[332] Lucchini M, Sato S A, Schlaepfer F, Yabana K, Gallmann L, Rubio A and Keller U 2020 *Journal of Physics: Photonics* **2** 025001

[333] Seres E, Seres J, Serrat C and Namba S 2016 *Phys. Rev. B* **94** 165125

[334] Volkov M, Sato S A, Schlaepfer F, Kasmi L, Hartmann N, Lucchini M, Gallmann L, Rubio A and Keller U 2019 *Nature Physics* **15** 1145–1149

[335] Eichmann H, Egbert A, Nolte S, Momma C, Wellegehausen B, Becker W, Long S and McIver J K 1995 *Physical Review A* **51** R3414–R3417

[336] Fleischer A, Kfir O, Diskin T, Sidorenko P and Cohen O 2014 *Nature Photonics* **8** 543–549

[337] Kfir O, Grychtol P, Turgut E, Knut R, Zusin D, Popmintchev D, Popmintchev T, Nembach H, Shaw J M, Fleischer A, Kapteyn H, Murnane M and Cohen O 2015 *Nature Photonics* **9** 99–105

[338] Fan T, Grychtol P, Knut R, Hernández-García C, Hickstein D D, Zusin D, Gentry C, Dollar F J, Mancuso C A, Hogle C W, Kfir O, Legut D, Carva K, Ellis J L, Dorney K M, Chen C, Shpyrko O G, Fullerton E E, Cohen O, Oppeneer P M, Milošević D B, Becker A, Jaroń-Becker A A, Popmintchev T, Murnane M M and Kapteyn H C 2015 *Proceedings of the National Academy of Sciences* **112** 14206–14211

[339] Hickstein D D, Dollar F J, Grychtol P, Ellis J L, Knut R, Hernández-García C, Zusin D, Gentry C, Shaw J M, Fan T, Dorney K M, Becker A, Jaroń-Becker A, Kapteyn H C, Murnane M M and Durfee C G 2015 *Nature Photonics* **9** 743–750

[340] Bigot J Y, Vomir M and Beaurepaire E 2009 *Nature Physics* **5** 515–520

[341] Siegrist F, Gessner J A, Ossiander M, Denker C, Chang Y P, Schröder M C, Guggenmos A, Cui Y, Walowski J, Martens U, Dewhurst J K, Kleineberg U, Münzenberg M, Sharma S and Schultze M 2019 *Nature* **571** 240–244

[342] Dewhurst J K, Elliott P, Shallcross S, Gross E K U and Sharma S 2018 *Nano Letters* **18** 1842–1848

[343] Cirri A, Husek J, Biswas S and Baker L R 2017 *The Journal of Physical Chemistry C* **121** 15861–15869

[344] Porter I J, Cushing S K, Carneiro L M, Lee A, Ondry J C, Dahl J C, Chang H T, Alivisatos A P and Leone S R 2018 *The Journal of Physical Chemistry Letters* **9** 4120–4124

[345] Biswas S, Husek J and Baker L R 2018 *Chemical Communications* **54** 4216–4230

[346] Papalazarou E, Boschetto D, Gautier J, Garl T, Valentin C, Rey G, Zeitoun P, Rousse A, Balcou P and Marsi M 2008 *Applied Physics Letters* **93** 041114
[347] Lucarelli G D, Moio B, Inzani G, Fabris N, Moscardi L, Frassetto F, Poletto L, Nisoli M and Lucchini M 2020 *Review of Scientific Instruments* **91** 053002
[348] Kaplan C J, Kraus P M, Gullikson E M, Borja L J, Cushing S K, Zürch M, Chang H T, Neumark D M and Leone S R 2019 *Journal of the Optical Society of America B* **36** 1716
[349] Kaplan C J, Kraus P M, Ross A D, Zürch M, Cushing S K, Jager M F, Chang H T, Gullikson E M, Neumark D M and Leone S R 2018 *Physical Review B* **97** 205202
[350] Géneaux R, Kaplan C J, Yue L, Ross A D, Bækhøj J E, Kraus P M, Chang H t, Guggenmos A, Huang M y, Zürch M, Schafer K J, Neumark D M, Gaarde M B and Leone S R 2020 *Physical Review Letters* **124** 207401
[351] Hanson W F, Arakawa E T and Williams M W 1972 *Journal of Applied Physics* **43** 1661–1665
[352] Wannier G H 1937 *Physical Review* **52** 191–197
[353] Mott N F 1938 *Transactions of the Faraday Society* **34** 500
[354] Mysyrowicz A, Hulin D, Antonetti A, Migus A, Masselink W T and Morkoç H 1986 *Physical Review Letters* **56** 2748–2751
[355] Nordstrom K B, Johnsen K, Allen S J, Jauho A P, Birnir B, Kono J, Noda T, Akiyama H and Sakaki H 1998 *Physical Review Letters* **81** 457–460
[356] Butov L 2017 *Superlattices and Microstructures* **108** 2–26
[357] Ren X, Li J, Yin Y, Zhao K, Chew A, Wang Y, Hu S, Cheng Y, Cunningham E, Wu Y, Chini M and Chang Z 2018 *Journal of Optics* **20** 023001
[358] Elu U, Baudisch M, Pires H, Tani F, Frosz M H, Köttig F, Ermolov A, Russell P S and Biegert J 2017 *Optica* **4** 1024–1029
[359] Mitrofanov A V, Voronin A A, Rozhko M V, Sidorov-Biryukov D A, Fedotov A B, Pugžlys A, Shumakova V, Ališauskas S, Baltuška A and Zheltikov A M 2017 *Optica* **4** 1405–1408
[360] Wang P, Li Y, Li W, Su H, Shao B, Li S, Wang C, Wang D, Zhao R, Peng Y, Leng Y, Li R and Xu Z 2018 *Opt. Lett.* **43** 2197–2200
[361] Huang P C, Hernández-García C, Huang J T, Huang P Y, Lu C H, Rego L, Hickstein D D, Ellis J L, Jaron-Becker A, Becker A, Yang S D, Durfee C G, Plaja L, Kapteyn H C, Murnane M M, Kung A H and Chen M C 2018 *Nature Photonics* **12** 349–354
[362] Ferré A, Handschin C, Dumergue M, Burgy F, Comby A, Descamps D, Fabre B, Garcia G A, Géneaux R, Merceron L, Mével E, Nahon L, Petit S, Pons B, Staedter D, Weber S, Ruchon T, Blanchet V and Mairesse Y 2015 *Nature Photonics* **9** 93–98
[363] Mukamel S, Healion D, Zhang Y and Biggs J D 2013 *Annual Review of Physical Chemistry* **64** 101–127
[364] Cao W, Warrick E R, Fidler A, Neumark D M and Leone S R 2016 *Phys. Rev. A* **94**(5) 053846
[365] Cao W, Warrick E R, Fidler A, Leone S R and Neumark D M 2018 *Phys. Rev. A* **97**(2) 023401
[366] Marroux H J B, Fidler A P, Neumark D M and Leone S R 2018 *Science Advances* **4** eaau3783
[367] Fidler A P, Camp S J, Warrick E R, Bloch E, Marroux H J B, Neumark D M, Schafer K J, Gaarde M B and Leone S R 2019 *Nature Communications* **10** 1384

Rocío Borrego-Varillas is staff researcher at the Institute of Photonics and Nanotecnologies of the National Research Council (CNR-IFN). She obtained a PhD in Physics at the Universidad de Salamanca in 2013. In the same year she was awarded a Marie Curie fellowship and joined Prof. Cerullo's group at Politecnico di Milano. During her postdoc she developed novel techniques for the generation of ultrashort UV pules and their application to ultrafast molecular dynamics. At present she is responsible of the scientific activity in the laboratory for attosecond dynamics in molecules. Her research interests include few-cycle pulse generation in the UV, ultrafast spectroscopy of biomolecules and sub-femtosecond electron dynamics. She is the president of the Ultrafast Optical Phenomena OSA technical group and serves in the editorial committee of the journals "Photonics", "Journal of Optics" and "Optics and Photonics News". She has been awarded the "Ivan Kaminow Outstanding Young Professional Prize" by the OSA in 2016 and very recently the "EOS Early Career Women in Photonics Award" by the European Optical Society.

Matteo Lucchini is Senior Assistant Professor by the Physics Department of Politecnico di Milano. He studied Engineering Physics at the Politecnico di Milano where he graduated in December 2008. He obtained a PhD in Physics at the same institute in March 2012 with a thesis on the development of new techniques for the generation of single attosecond pulses and their application to molecular dynamics. In the same year, he joined the the Ultrafast Laser Physics Group, Eidgenössische Technische Hochschule (ETH), lead by with Prof. Ursula Keller, where he was awarded an ETH Zurich postdoctoral fellowship (Marie-Curie co-funded) and started to investigate attosecond dynamics in solids with photo-emission and photo-absorption spectroscopy. In 2017 he became junior assistant professor at Politecnico di Milano and in 2019 he has been awarded the price Alfredo di Braccio for young Italian physicist and the Fresnel price by the European Physical Society for outstanding contributions in the field of Attosecond Science. In 2021 he has been awarded the prize "Antonio Feltrinelli Giovani". At present, Matteo is in charge of the ERC-STG project AuDACE (No. 848411), which aims at studying the very first instants of light-matter interaction with attosecond laser pulses in advanced materials.

Mauro Nisoli is Full Professor at Politecnico di Milano since 2011. From 1990 to 2000, he was a Researcher of the National Research Council (CNR), Center of Quantum Electronic and Electronic Instrumentation; from 2001 to 2010, he was an Associate Professor with the Department of Physics, Politecnico di Milano. He is the Head of the Attosecond Research Center at the Department of Physics of Politecnico and he is co-director of the International School "The Frontiers of Attosecond and Ultrafast X-ray Science". He is author of more than 200 research papers in international journals and several invited and tutorial communications at international meetings and schools. His research focus are the following: attosecond science, ultrashort-pulse laser technology, and control and real-time observation of electronic motion in atoms, molecules and solids. He was awarded an European Research Council (ERC) Advanced Grant in 2009 (Electron-scale dynamics in chemistry, ELYCHE) and an ERC Synergy Grant in 2020 (The ultimate time scale in organic molecular opto-electronics, the attosecond, TOMATTO). He is OSA Fellow for innovative contributions to the field of attosecond science and technology, particularly for ground-breaking applications of attosecond pulses to molecules.